



**Interactions between Radiation, Clouds and  
Convective Self-Aggregation in Idealised  
Numerical Simulations**

---

Kieran Nicholas Pope

A thesis submitted in fulfilment of the requirements for the degree of  
Doctor of Philosophy

**PhD Atmosphere, Oceans and Climate**

**Department of Meteorology**

**School of Mathematical, Physical and Computational Sciences**

**February 2023**

University of Reading

DECLARATION

I confirm that this is my own work and the use of all material from other sources has been properly and fully acknowledged.

Kieran Nicholas Pope

# Abstract

Tropical weather is dominated by convection which is organised across a wide range of spatial and temporal scales. The degree of convective organisation has important consequences for weather and climate. The uncertainty in the response of convective organisation to a warming climate is one of the largest sources of uncertainty in climate sensitivity estimates.

Self-aggregation is the process in which convection spontaneously clusters despite homogeneous initial conditions and forcing. It has been the focus of many recent studies because of its implications for real world weather and climate. Cloud-radiation interactions have been shown to be crucial drivers and maintainers of aggregation. Yet there remains uncertainty in their role in self-aggregation. In this thesis, we develop a framework to study aggregation and quantify the contributions of radiative interactions with different cloud types to aggregation. We study models that form part of the Radiative-Convective Equilibrium Model Intercomparison Project, comparing models with explicit and parameterised convection across a range of sea surface temperatures (SSTs).

We find that longwave interactions with high-topped cloud and clear regions, as well as shortwave interactions with water vapour are key drivers and/or maintainers of aggregation. Their influence on aggregation tends to decrease with SST, but the rate of aggregation remains similar. We find the strength of these interactions strongly correlates with the rate of aggregation in parameterised convection simulations, yet the rate of aggregation in explicit simulations is more strongly influenced by circulations.

Parameterised convection simulations often have stronger longwave interactions with high-topped cloud than explicit simulations, resulting in faster aggregation. We find that by artificially reducing this longwave feedback in parameterised simulations, the aggregation behaves more similarly to explicit simulations. This highlights that global weather and climate models may be able to model the effects of real-world aggregation more accurately given an accurate representation of cloud-radiation interactions.

## ACKNOWLEDGEMENTS

Foremost, I would like to thank my supervisors: Chris Holloway, Thorwald Stein and Todd Jones. I have always considered myself extremely lucky to have such great supervisors. Your curiosity, encouragement, feedback, and humour have helped me through the highs and lows of the PhD. I always looked forward to our weekly Friday afternoon meetings that gave me the motivation to keep working until the next meeting. I would also like to thank my Monitoring Committee members: Keith Shine and Miguel Teixeira, for their biannual critical feedback and quality control to ensure I remain on track.

I am grateful to the Natural Environment Research Council for funding this work via the SCENARIO Doctoral Training Partnership.

Next, I would like thank my friends that have been there throughout this journey, and whose support has been invaluable. Thank you to my housemates - who made it through the pandemic with me, somehow making living through these times one of the highlights of my life. Thanks to my few fellow office mates on Lyle 5 who made it through to Lyle's bitter end; and to my three other original MMet undergrads who have made it through the undergrad and PhD with me. Thank you also, to my friends at the far corners of the globe, who, despite being so far away, have continuously been there for me and supported

---

me throughout.

And finally, thank you to my family – for fostering my curiosity throughout my whole life and continuously encouraging me through the ups and downs – and whose love and support have carried me to where I am today.

<b>1</b>	<b>Introduction</b>	<b>1</b>
1.1	Background . . . . .	1
1.2	Thesis Objectives . . . . .	12
1.3	Thesis Structure . . . . .	13
<b>2</b>	<b>Data and Methods</b>	<b>15</b>
2.1	Radiative-Convective Equilibrium Model Intercomparison Project (RCEMIP)	15
2.2	UK Met Office Unified Model (UKMOi-vn11.0-RA1-T) . . . . .	16
2.3	Variance of Normalised FMSE Budget . . . . .	19
<b>3</b>	<b>Cloud-Radiation Interactions and their Contributions to Convective Self- Aggregation</b>	<b>23</b>
3.1	Introduction . . . . .	23
3.2	Methods . . . . .	25
3.2.1	Data and Analysis Framework . . . . .	25
3.2.2	Cloud Classification Scheme . . . . .	25
3.3	Aggregation within the <i>LARGE</i> Domain . . . . .	27

---

3.4	Cloud Type Contributions during the Maintenance of Aggregation . . . . .	34
3.4.1	Longwave Cloud Interactions . . . . .	40
3.4.2	Longwave Interactions within the Clear Regions . . . . .	44
3.4.3	Shortwave Interactions . . . . .	49
3.5	Cloud Type Contributions throughout the Aggregation Process . . . . .	51
3.6	Comparison of Convection within High-Resolution Simulations . . . . .	54
3.7	Conclusions . . . . .	61
<b>4</b>	<b>Radiation, Clouds, and Self-Aggregation in RCEMIP Simulations</b>	<b>67</b>
4.1	Introduction . . . . .	67
4.2	Methods . . . . .	70
4.2.1	Normalised FMSE Framework for the CRMs and GCMs in RCEMIP	70
4.2.2	Cloud Classification Scheme . . . . .	72
4.3	Variance of Normalised FMSE . . . . .	77
4.3.1	Evolution of Normalised FMSE variance in RCEMIP simulations . .	77
4.3.2	Normalised FMSE variance budget analysis . . . . .	80
4.4	Contributions of Cloud-Radiation Interactions to Aggregation . . . . .	89
4.4.1	Cloud-Radiation Interactions within CRMs . . . . .	89
4.4.2	Comparison of Cloud-Radiation Interactions within CRMs and GCMs	94
4.5	Conclusions . . . . .	98
4.5.1	Robustness of Pope et al. (2021) results . . . . .	98
4.5.2	Differences between GCMs and CRMs . . . . .	101
<b>5</b>	<b>The Response of Convective Self-Aggregation to Enhanced Radiative- Convective Interactions in Explicit and Parameterised Convection Sim- ulations</b>	<b>104</b>
5.1	Introduction . . . . .	104
5.2	Methods . . . . .	106

---

---

5.2.1	Experiment Design . . . . .	106
5.2.2	Analysis Framework . . . . .	109
5.2.3	Expected Cloud-Longwave Forcing Response to Modified $C_{tot}$ . . . . .	110
5.3	Response of Cloud to Modified Cloud-Radiation Interactions . . . . .	112
5.4	Self-Aggregation within the Simulations . . . . .	120
5.5	Influence of Enhanced Cloud-Radiation Interactions on the Longwave-FMSE Feedback . . . . .	127
5.6	Conclusions . . . . .	137
<b>6</b>	<b>Conclusions</b>	<b>142</b>
6.1	Conclusions . . . . .	142
6.2	Summary of Major Outcomes . . . . .	142
6.3	Future Work . . . . .	148
<b>A</b>	<b>Normalised FMSE Variance Budget Equation Derivation</b>	<b>151</b>
	<b>Bibliography</b>	<b>153</b>

## 1.1 Background

The weather in the tropics is dominated by convection. The tropical atmosphere is in an approximate equilibrium between atmospheric radiative cooling and convective heating called radiative-convective equilibrium (RCE) (e.g. Manabe and Wetherald, 1967). With radiative cooling of the free troposphere, consistently high surface temperatures, and an abundant supply of moisture, convection occurs to neutralise conditional instability, resulting in strong rainstorms. This convection can form a wide variety of structures with a great range of spatial and temporal scales depending on the state of convective organisation. Structures can range from individual cumulonimbus clouds, to squall lines (e.g. Houze, 1977), mesoscale convective systems (MCSs) (e.g. Houze, 2004), tropical cyclones (e.g. Emanuel et al., 2003), and the convective phase of the Madden-Julian Oscillation (MJO) (Madden and Julian, 1971; Nakazawa, 1988; Mapes and Houze, 1993). The degree of convective organisation affects the environment of both the convective regions and surrounding subsiding regions (Wing, 2019), as well as global-scale circulations (Arnold and Randall, 2015) and climate (Coppin and Bony, 2018). Because of its impacts on

weather and climate, convective organisation has been the focus of many observational and modelling studies.

The majority of tropical rainfall comes from organised convection. Organised convective systems that last upwards of 12 hours account for 75% of tropical precipitation, and systems that propagate at least 250 km account for 60% of tropical precipitation (Roca et al., 2014). Long-lived, well-organised MCSs contribute disproportionately to the total extreme tropical rainfall (Roca and Fiolleau, 2020). There is some disagreement as to the effects of aggregation on instantaneous precipitation rates, with some studies finding it increases by as much as 30% (Da Silva et al., 2021), and others finding little difference (Bao and Sherwood, 2019). However, these studies agree that extreme daily precipitation rates increase with higher degrees of organisation thanks to the increased clustering of rainstorms and enhanced precipitation efficiency.

The aggregation of tropical convection has significant impacts on the climate, with convective aggregation reducing the high-cloud fraction and free-troposphere humidity (e.g. Bretherton et al., 2005; Tobin et al., 2013; Wing and Cronin, 2016), affecting the amount of shortwave radiation being absorbed by the atmosphere and surface, as well as affecting the amount of longwave radiation escaping to space. The uncertainty in the response of aggregation to a warming climate is a major source of uncertainty in our estimates for the global climate sensitivity (Sherwood et al., 2020), with models that increase in aggregation with warming tending to have a lower climate feedback parameter due to increased longwave cooling (Becker and Wing, 2020).

There are many processes that cause tropical convective organisation. Much of the convection is organised as a result of convectively coupled equatorial waves. These are zonally-propagating low-pressure systems that form as a result of near-equatorial convection on a rotating planet (Matsuno, 1966; Kiladis et al., 2009). Sea surface temperature (SST) hotspots act as convergence zones for convection, which help initiate convective organisation but are not essential for the maintenance of organisation (Müller and Ho-

henegger, 2020; Bretherton et al., 2004). Convection can further be organised along the low-level convergence of trade winds (Back and Bretherton, 2009).

Another mechanism of organisation has been termed convective self-aggregation: a process, first identified in idealised models, by which convection spontaneously becomes clustered despite homogeneous initial conditions and forcing (e.g. Wing et al., 2017). Self-aggregation has been the focus of many recent studies; the majority of which have used idealised simulations of RCE to further understand the processes that cause this phenomenon (e.g. Held et al., 1993; Bretherton et al., 2005; Muller and Held, 2012; Wing and Emanuel, 2014). A review of self-aggregation in numerical models has been published by Wing et al. (2017). Despite self-aggregation being first recognised in these idealised numerical models, key processes that drive self-aggregation are indeed relevant to the real atmosphere (Holloway et al., 2017), aiding the development of organised structures including tropical cyclones (Nolan et al., 2007; Wing et al., 2016) and the Madden–Julian oscillation (Raymond and Fuchs, 2009; Arnold and Randall, 2015).

Several mechanisms have been shown to be important in influencing self-aggregation; including interactions between convection and surface fluxes, (e.g. Tompkins and Craig, 1998), a coarsening of the moisture field (e.g. Craig and Mack, 2013), the virtual effect of water vapour (Yang, 2018a), entrainment of convective updrafts (Tompkins and Semie, 2017), radiatively-driven boundary layer circulations (e.g. Muller and Held, 2012; Muller and Bony, 2015; Naumann et al., 2017), and interactions between convection and radiation (e.g. Bretherton et al., 2005; Beucler and Cronin, 2016). However, there still remains much uncertainty in the mechanisms that drive and maintain self-aggregation (Wing et al., 2017), the SST dependence of aggregation (Wing et al., 2020), and the impacts of aggregation on climate sensitivity (Becker and Wing, 2020). These uncertainties are in part due to the inter-model variability in the structures and dynamics of convection within RCE models (Wing et al., 2017).

Most modelling studies of aggregation use simulations of RCE that are highly idealised.

These simulations are often configured over an ocean with a fixed SST, without rotation, without a diurnal solar cycle, and without a mean wind or wind shear profile. However, studies have shown that these aforementioned factors do influence aggregation. The use of an interactive SST in RCE simulations initially slows the rate of aggregation, with a shallower interactive ocean slab associated with a decrease in aggregation rate (Hohenegger and Stevens, 2016; Coppin and Bony, 2017). This is because enhanced shortwave heating in the clear regions leads to anomalously warm SSTs in these non-convective regions, opposing aggregation. However, the SST in the non-convective regions is dependent on its dryness (Shamekh et al., 2020). As the non-convective regions become very dry, enhanced surface evaporation leads to a cooling effect that dominates over the shortwave heating. This leads to negative SST anomalies, and favours aggregation in its mature phase.

The characteristics and mechanisms of aggregation are strongly dependent on rotation (Carstens and Wing, 2022). The effects of rotation are small for latitudes equatorward of  $\pm 5^\circ$ , but moist convective regions will develop into tropical cyclones for latitudes poleward of  $\pm 9^\circ$ . For these latitudes, convective organisation is more strongly driven by surface flux feedbacks, with strong winds in the convective regions producing an enhanced latent heat flux which further intensifies convection.

Land and orography also influences convective organisation, helping to form regions of convergence. There are also distinct distributions in the shapes of organised convective structures over land and over the ocean (Liu and Zipser, 2013). Organised convective systems tend to be larger and more circular in shape over land, while more linear over the ocean. These distributions in convective structures are additionally influenced by the season. Convection over land tends to be more powerful, and has a much stronger diurnal cycle compared to convection over the ocean (Nesbitt et al., 2000).

The structures of convection are strongly influenced by wind shear, affecting the storm mode, duration and intensity of the convection (Rotunno et al., 1988). Using numerical simulations, Chen et al. (2015) find that enhanced low-level wind shear favours linear

convective structures, whereas mid-level shear tends to produce more isolated supercell-like storms with rotating updrafts. Wind shear tends to dampen self-aggregation by smoothing horizontal moisture variations (Tompkins, 2001), and by enhancing the surface latent heat flux in dry regions (Bretherton et al., 2005).

Despite convective aggregation being affected by these previously mentioned factors, the ocean covers the majority of the tropics where the diurnal cycle of convection is weak, the effects of rotation are small, and wind shear is often weak. Therefore, highly idealised models remain a valuable tool in understanding tropical convection. They can be used to study the interactions between convection, radiation, surface fluxes and circulations that affect aggregation, and can be used to study the impacts of aggregation on weather and climate. We study these highly idealised simulations throughout this thesis.

Various metrics have been proposed to characterise aggregation, some of which measure the horizontal variability of moisture throughout the domain. As aggregation increases, dry regions generally get drier, convective regions become increasingly humid, and the spatial scale of these regions increases. The interquartile range (IQR) of precipitable water (PW) is used as an aggregation metric in some studies (e.g. Bretherton et al., 2005; Holloway and Woolnough, 2016). However, this metric is highly dependent on temperature due to the Clausius–Clapeyron exponential water vapour dependence on temperature. To account for this temperature dependence, some studies choose to normalise PW by dividing it by saturated PW, and measuring the horizontal variability of this column relative humidity (e.g. Craig and Mack, 2013; Wing and Cronin, 2016).

The variance of column-integrated moist static energy (MSE) or frozen MSE (FMSE) is a frequently used metric which is highly correlated with the IQR of PW. FMSE, or  $h$  ( $\text{J kg}^{-1}$ ), is defined as the sum of an air parcel’s internal energy, potential energy and latent heat. It is given by

$$h = c_p T + gz + L_v q_v - L_f q_i \tag{1.1}$$

where  $c_p$  is the specific heat capacity of dry air at constant pressure,  $T$  is temperature,  $g$  is the gravitational acceleration,  $z$  is the height above the surface,  $L_v$  is the latent heat of vaporisation,  $q_v$  is the water vapor mixing ratio,  $L_f$  is the latent heat of fusion and  $q_i$  is the condensed ice mixing ratio. FMSE differs from MSE by accounting for the changes in enthalpy associated with the freezing and melting of water. However, the contribution of this freezing term is small in comparison to the other terms in vertically-integrated FMSE budget analyses. In non-rotating RCE experiments over a fixed SST, variations in humidity contribute the most to the horizontal variability in FMSE as horizontal temperature gradients are weak, and the gravitational potential term is approximately uniform throughout the domain. Therefore, the variance of column-integrated FMSE is highly correlated to other metrics that measure the spatial variability of moisture.

FMSE is not entirely conserved for all convective processes, e.g. energy is not conserved when an air parcel precipitates or when its pressure change is non hydrostatic. Indeed, FMSE minus convective available potential energy (CAPE) is shown to be a better conservation approximation (Romps, 2015), as this quantity accounts for energy transfer associated with non-hydrostatic processes. However, under the majority of moist adiabatic processes, FMSE conservation remains to be a fair approximation. Therefore, convection does little to change a parcel's FMSE, but convective processes redistribute FMSE.

The density-weighted vertical integral of FMSE is almost entirely affected by radiation, surface fluxes and advection. When convection is randomly distributed across the domain, FMSE is approximately horizontally uniform. As convection aggregates, large overturning circulations develop and intensify. Regions with large-scale ascent are moister and favourable for deep convection. Regions with large-scale subsidence are drier and convection is suppressed. Column-integrated diabatic radiative heating and cooling has a large influence on FMSE variability despite FMSE variance being dominated by the horizontal water vapour distribution. This is because horizontal temperature gradients are weak, so

anomalous diabatic heating results in ascent which converges moisture into the column. Similarly, anomalous diabatic cooling leads to subsidence which dries the column.

Wing and Emanuel (2014) derive a budget equation for the rate of change of vertically-integrated FMSE variance, allowing for the quantification of the contributions of different FMSE feedbacks to the rate of change of aggregation:

$$\frac{1}{2} \frac{\partial \hat{h}'^2}{\partial t} = \hat{h}' LW' + \hat{h}' SW' + \hat{h}' SEF' - \hat{h}' \nabla_h \cdot \mathbf{u} \hat{h} \quad (1.2)$$

where hats ( $\hat{\phantom{x}}$ ) denote a density-weighted vertical integral,  $LW$  and  $SW$  are the net column longwave and shortwave heating ( $\text{W m}^{-2}$ ), respectively,  $SEF$  is the surface enthalpy flux, made up of the surface latent heat and sensible heat fluxes,  $\nabla_h \cdot \mathbf{u} \hat{h}$  is the horizontal divergence of the  $\hat{h}$  flux, and primes ( $'$ ) indicate local anomalies from the instantaneous domain-mean. The net longwave and shortwave radiative heating is defined as the column radiative flux convergence as follows:

$$LW = LW \uparrow_{\text{sfc}} - LW \downarrow_{\text{sfc}} - LW \uparrow_{\text{top}} \quad (1.3)$$

$$SW = SW \downarrow_{\text{top}} - SW \uparrow_{\text{top}} - SW \downarrow_{\text{sfc}} + SW \uparrow_{\text{sfc}} \quad (1.4)$$

where upward and downward arrows indicate upwelling and downwelling fluxes, and the subscripts ( $_{\text{sfc}}$ ) and ( $_{\text{top}}$ ) indicate a radiative flux at the surface and at the top of the atmosphere, respectively. Each term on the right hand side of Equation (1.2) is a covariance between the  $\hat{h}$  anomaly and the anomaly of a source/sink of  $\hat{h}$ . If the term is positive, there is either an anomalous source of  $\hat{h}$  in a region of already high  $\hat{h}$ , or an anomalous sink of  $\hat{h}$  in a region of low  $\hat{h}$ , representing a positive feedback on self-aggregation.

There is some disagreement over the importance of each of the feedbacks in Equation 1.2 to aggregation, as well as their SST dependencies and dependencies on aggregation

(Wing et al., 2017). The majority of studies that use the FMSE variance budget framework find surface flux feedbacks are strong, positive contributors to aggregation at early stages, sometimes being the leading driver of aggregation. However, their SST dependence is up for debate with the feedback either increasing (Coppin and Bony, 2015), decreasing (Becker et al., 2017), or remaining similar with SST (Wing et al., 2016). Feedbacks between FMSE and both shortwave and longwave radiation have been shown to be key drivers and maintainers of aggregation (e.g. Holloway and Woolnough, 2016; Wing et al., 2016; Becker et al., 2017), and interactive radiation in models is essential for aggregation to occur (Wing et al., 2017; Muller and Bony, 2015).

Muller and Held (2012) find that it is the longwave cooling effect of low clouds within dry regions that is responsible for the onset of self-aggregation. The resultant circulation driven by radiative cooling atop these clouds drives an upgradient transport of FMSE, which increases the variance of FMSE. They find the sensitivity of self-aggregation to domain size and resolution to be a result of the sensitivity of low cloud distributions within the model. Once the convection is aggregated, the longwave cooling effect of low clouds is not necessary to maintain aggregation (Muller and Held, 2012; Muller and Bony, 2015).

Direct cloud-radiation interactions have a major influence on self-aggregation by influencing the net column longwave and shortwave heating rates in Equations 1.3 and 1.4. Clouds can have a net shortwave cooling effect by reflecting solar radiation to space, but can also have a net longwave warming effect by reducing outgoing emission (Liou, 1986). Wing and Emanuel (2014) note the importance of the shortwave radiative feedback due to increased shortwave absorption within high-FMSE regions compared to low-FMSE regions, increasing the FMSE variance. By comparing the clear-sky radiative fluxes (radiative fluxes neglecting cloud) to the total radiative fluxes, they find that the shortwave feedback is mainly a clear-sky effect, with the effects of shortwave absorption by water vapour outweighing the reflecting and absorbing effects of cloud. Although the short-

wave feedback has a small effect compared to the longwave feedback during the early and mature stages of aggregation, they find it dominates the total radiative feedback at the intermediate stage.

Unlike the shortwave feedbacks, the clear-sky longwave feedback is small in comparison to the total longwave feedback. A simple schematic of longwave interactions with different cloud types is shown in Figure 1.1. High-topped clouds prevent radiation emitted below from escaping to space, and with their cold cloud tops, they emit little to space compared to clear regions. This reduces the magnitude of the final term of Equation (1.3) and helps to anomalously warm the atmospheric column. Shallow clouds have relatively warm cloud tops, so these columns emit only slightly less longwave radiation to space than clear columns. Clouds also affect the surface downwelling longwave radiation (DLR) by emitting more radiation downwards than in the clear regions. However, with the lower atmosphere being warm and usually fairly moist, DLR is always high in comparison to outgoing longwave radiation (OLR) and there is much less variability in DLR than OLR regardless of cloud type. Nevertheless, clouds with lower, warmer bases have greater DLR, which enhances the vertically-integrated net longwave cooling rate. The result is columns with high-topped clouds warm the atmosphere more than clear regions, and shallow clouds often have a slightly greater cooling rate than the clear regions.

The magnitude of the cloud-longwave radiative effects is dependent on the altitude, optical depth, effective size of the cloud particles and composition of the cloud. Higher, thicker clouds reduce OLR, leading to a greater net longwave heating effect (e.g. Hong et al., 2016). Additionally, clouds with smaller particles have enhanced cloud-radiation interactions as they have a higher albedo and are able to trap more longwave radiation (e.g. Vergara-Temprado et al., 2018). The effective cloud particle size is dependent on the phase of the cloud, with liquid clouds having a greater number of particles for a given condensed water content, resulting in enhanced longwave and shortwave effects (e.g. Fu and Liou, 1993).

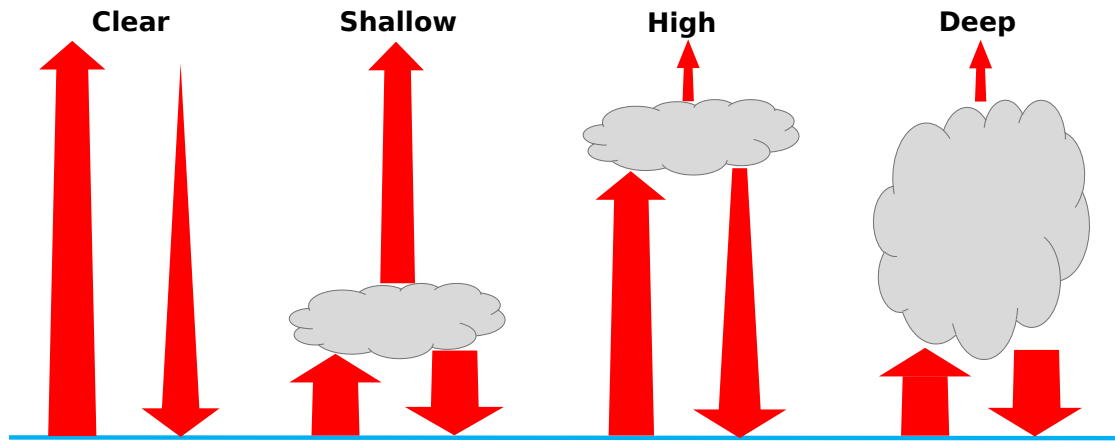


Figure 1.1: Schematic to show upwelling and downwelling longwave fluxes into and out of the atmosphere for clear, shallow, high, and deep cloud. The thickness of the arrows indicates the magnitude of the flux.

Longwave fluxes out of the atmosphere are also dependent on the temperature and humidity profiles. A warmer atmosphere generally has greater longwave emission (greater radiative cooling) following the Stefan-Boltzmann law. As the water vapour path (WVP) increases, the optical thickness of the atmospheric infrared windows (the ranges of longwave wavelengths for which water vapour is only a weak absorber) increases and narrows (e.g. Koll and Cronin, 2018). This raises the altitude of the effective level of emission of OLR to a cooler environment, decreasing OLR and helping decrease cooling of the atmospheric column (e.g. Allan et al., 1999). Increasing WVP also has the effect of lowering the effective level of emission of DLR to a warmer level, increasing DLR and increasing atmospheric cooling (e.g. Ruckstuhl et al., 2007). These relationships between WVP, OLR and DLR are also sensitive to the vertical distribution of water vapour; with upper-level humidity variations having the largest influence on OLR, and lower-level humidity variations mainly influencing DLR.

Wing and Emanuel (2014) find that longwave cooling is most influenced by cloud in the moist convective regions, but dominated by the clear-sky cooling in the dry subsiding regions. During the mature phase of aggregation, they find the reduced longwave cooling

of high clouds within high-FMSE regions becomes the dominant feedback maintaining aggregation. They also note that dry regions initially have anomalously strong radiative cooling, resulting in a positive longwave feedback, whereas at later times, the dry regions amplify, becoming dryer, which decreases low-level emissivity. Anomalous longwave heating then develops at low levels to the extent that the column longwave heating anomaly becomes positive.

Wing and Cronin (2016) study the SST sensitivity of cloud-radiative effects and find that clouds contribute strongly to both the longwave and shortwave radiative feedbacks, particularly at early times and cooler SSTs. In rotating RCE simulations, the longwave interactions with cloud contribute a significant amount to tropical cyclogenesis particularly at early stages of cyclone development (Wing et al., 2016; Muller and Roms, 2018).

A caveat of using the FMSE variance budget framework to study aggregation is the strong SST dependence of FMSE, making it difficult to fairly compare aggregation across simulations with different SSTs. Some studies choose to divide the budget terms by the instantaneous variance of FMSE to eliminate the SST dependence (e.g. Wing and Cronin, 2016; Holloway and Woolnough, 2016). Therefore, this technique compares the budget terms as a fraction of how aggregated the domain is, but it does not allow for the direct comparison of each budget term at specific stages of aggregation for different simulations.

The contributions from cloud-radiation interactions to convective self-aggregation have been generally shown to be important in previous studies, but a detailed analysis considering the role of specific cloud types is missing. With both the horizontal and vertical distribution of clouds being one of the largest sources of variability amongst RCE simulations (Wing et al., 2020), a detailed investigation into the role of specific cloud types on self-aggregation may help in explaining the variability of self-aggregation amongst RCE simulations and the consequential implications for climate sensitivity.

## 1.2 Thesis Objectives

There is much variability in the progression and characteristics of convective aggregation in numerical models, and cloud-radiation interactions have been shown to be crucial in the development and maintenance of convective aggregation. Uncertainties in the mechanics and characteristics of aggregation, and their sensitivities to a warming climate result in one of the largest sources of uncertainty in climate predictions.

This thesis aims to shed light on some of the causes of this inter-model variability by studying the contributions of cloud-radiation interactions to convective self-aggregation in idealised numerical models. We study these interactions throughout the development and maintenance stages of aggregation, across a range of SSTs, and for a range of model configurations; from small, square domains with 100 m horizontal grid spacing, to global-scale models with  $\sim 100$  km horizontal grid spacing.

The objectives of the thesis are to:

1. Design a framework that can be used to study how different cloud-radiation interactions contribute to convective self-aggregation across a range of SSTs and resolutions.
2. Determine the key radiation-convection interactions that are responsible for the development and maintenance of aggregation, and assess their sensitivity to SST in cloud resolving models and general circulation models.
3. Assess the extent to which the inter-model variability of cloud-radiation interactions affects self-aggregation.
4. Assess how modifications to cloud-longwave interactions affect self-aggregation in explicit convection and parameterised convection simulations.

### 1.3 Thesis Structure

In Chapter 2, we discuss the data and methods used in this thesis. We discuss the Radiative-Convective Equilibrium Model Intercomparison Project (RCEMIP), from which we analyse several of the cloud-system resolving models (CRMs) and general circulation models (GCMs) that comprise the project, and whose protocol we use to run our own RCE simulations using the Met Office Unified Model (UM). We then describe our UM simulations, which are used in each of the three results chapters to study and compare convective aggregation. Finally, we describe our analysis framework that is used in each results chapter, enabling the fair study of the contributions of cloud-radiation interactions to aggregation across a range of SSTs and model resolutions (first thesis objective).

In Chapter 3, we use RCEMIP simulations of the UM to study the key radiation interactions that are responsible for the development and maintenance of aggregation in these models. We study convection over three different SSTs and across different domain sizes and resolutions to assess how radiative interactions with different cloud types contribute to aggregation, assessing their sensitivity to SST and grid spacing (preliminarily answering the second thesis objective).

The robustness of the conclusions from Chapter 3 is then tested by comparing the UM simulations to other similar simulations in RCEMIP in Chapter 4. We use our analysis framework to assess the variety of cloud-radiation interactions in the RCEMIP simulations (second thesis objective), and test whether the inter-model variability in cloud-radiation interactions can help explain the variability in the rate and degree of aggregation in these models (third thesis objective).

In Chapter 5, we use the UM to simulate a set of explicit convection simulations and a set of parameterised convection simulations, to study how the magnitude of cloud-longwave interactions affects aggregation by systematically modifying the radiative properties of cloud (fourth thesis objective).

We then provide a summary of the conclusions of the thesis in Chapter 6, and discuss further avenues of study.

## Opening remarks

In this chapter, we introduce the datasets used throughout the thesis, as well as our framework used to quantify and study aggregation. Methodologies unique to each chapter are described in the methods sections of those chapters.

### 2.1 Radiative-Convective Equilibrium Model Intercomparison Project (RCEMIP)

The Radiative-Convective Equilibrium Model Intercomparison Project (RCEMIP, Wing et al., 2018) has been designed to assess the variation of the RCE state across a range of model configurations including small and large cloud-system resolving models (CRMs) and general circulation models (GCMs). It allows for the assessment of the the sensitivity of clouds and convective aggregation to a warming climate across these model configurations. With its free data availability, it is a valuable source of data to study convective self-aggregation. We compare cloud-radiation interactions and self-aggregation in the CRMs

and GCMs of RCEMIP in Chapter 4.

The CRMs and GCMs of RCEMIP are configured using a strict protocol which is described in Wing et al. (2018). These protocols standardise the models, and aim to enable direct comparisons between them. CRMs perform  $\sim 100$ -day, non-rotating simulations with doubly periodic boundary conditions and explicit convection. They have at least 74 vertical levels spanning at least 33 km, and have a sponge layer in the upper layers to damp gravity waves. The large CRMs are on a channel domain of  $\sim 6,000$  km  $\times$  400 km with a 3 km horizontal grid spacing, and the small CRMs are on a square, 100 km  $\times$  100 km domain with a 1 km grid spacing. GCMs perform  $\sim 1,000$ -day, non-rotating, global-scale aquaplanet simulations with parameterised convection. They have a mean grid spacing of  $\mathcal{O}(1^\circ)$  varying between  $\sim 100$  km and  $\sim 170$  km, with the average grid spacing of all GCMs being  $\sim 120$  km. Every model in RCEMIP has a constant solar forcing of  $409.6$  W m $^{-2}$  (the tropical annual mean), a uniform surface albedo of 0.07, and performs simulations with three fixed SSTs of 295 K, 300 K and 305 K to compare how convection in RCE may be affected by a warming climate. 3D data are produced every 6 hours, which is the temporal resolution of much of our analysis throughout the thesis. However, 3D data is usually only output for the final 25 days of the simulations in the freely available RCEMIP data. Note that domain averaged 0D data, averaged 1D profiles, and 2D horizontal fields are usually output hourly throughout the simulations.

## 2.2 UK Met Office Unified Model (UKMOi-vn11.0-RA1-T)

In Chapter 3, we use the UK Met Office Unified Model version 11.0 to simulate RCE at three fixed SSTs: 295, 300 and 305 K, following the RCEMIP protocol. We mainly study convection within the “*LARGE*” simulations. These simulations are configured on a 6048 km  $\times$  432 km elongated channel domain with a 3 km horizontal grid spacing. However, we also analyse three other sets of simulations on smaller 100 km  $\times$  100 km

domains; the “*SMALL*” and “*SMALL\_RHCRIT*” simulations have a 1 km grid spacing, and the “*SMALL\_HI*” simulations have a 0.1 km grid spacing. These are used to assess how the radiative properties of clouds are affected by the critical humidity threshold for condensation (RHcrit) and grid spacing. The *LARGE* simulations are run for 113 days, the *SMALL* simulations are 124 days, the *SMALL\_HI* simulations are 54 days, and the *SMALL\_RHCRIT* simulations are 123 days.

The *LARGE*, *SMALL* and *SMALL\_RHCRIT* simulations have been configured following the RCEMIP protocol. The *SMALL\_HI* domain only differs from this protocol in that the horizontal grid spacing is ten times finer than the other 100 km × 100 km simulations in RCEMIP. The *LARGE* and *SMALL* simulations have been submitted to RCEMIP under the model name “UKMOi-vn11.0-RA1-T”, with the name “UKMO-RA1-T” being used in subsequent RCEMIP comparison papers (Wing et al., 2020; Becker and Wing, 2020).

RHcrit is a parameter in the Smith sub-grid cloud scheme (Smith, 1990) used in the Unified Model, and determines the grid-box mean relative humidity at which sub-grid humidity fluctuations are assumed large enough to result in some fraction of the grid-box becoming saturated and forming cloud. The *LARGE*, *SMALL*, and *SMALL\_HI* simulations all have a uniform RHcrit value of 0.99 across the entire domain. The value of RHcrit should depend on the dimensions of the grid-box, with coarser grid-boxes requiring a lower RHcrit to yield realistic cloud amounts. Our value of 99% is too high to yield realistic low cloud distributions (Morcrette, 2013) including at km-scale grid spacings. To see the effects of a more realistic RHcrit, we used another set of simulations that are identical to our *SMALL* simulations but for an RHcrit distribution used in the UK Met Office UKV model. Here, RHcrit is set to 96% in the lowest layers and decreases steadily to 80% at 900 m. RHcrit is then maintained at 80% above this level.

The RCEMIP protocol states that large-domain simulations for a given SST are initialised using the equilibrium soundings of the corresponding small-domain simulations,

providing aggregation does not occur in the small-domain. In our case, the *SMALL* simulations showed signs of self-aggregation, therefore, our *LARGE* simulations are initialised from a corresponding small-domain simulation with homogenised radiation, which showed no sign of aggregation. Note that there was a mistake in the initialisation of the *LARGE* simulations, in that the initial humidity profile is out by a density factor. Since density is close to unity in the lower troposphere, this mistake does not result in supersaturation at any level, and only results in the upper troposphere being drier than it should. Within two days of the simulation, convection remoistens the upper troposphere to a similar level to the intended initial profile. With the 2-day spin-up period neglected in our analysis, we believe this error will not have an impact on our conclusions.

The science configuration of our simulations is based on the tropical Regional Atmosphere and Land (RAL1-T) configuration (Bush et al., 2020). However, we use the Smith sub-grid cloud scheme (Smith, 1990) rather than the PC2 scheme (Wilson et al., 2008). With our simulations configured over an ocean, the land settings of RAL1-T are not used. The simulations use explicit convection set over a flat, Cartesian grid, with bi-periodic boundary conditions, using a vertical sigma-z-coordinate Charney-Philips staggering (Charney and Phillips, 1953). We use a 60 s time step for the *LARGE* simulations, a 30 s time step for the *SMALL* and *SMALL\_RHCRIT* simulations, and a 5 s time step for the *SMALL\_HI* simulations. The dynamical core uses a semi-implicit, semi-Lagrangian scheme that solves the non-hydrostatic, fully compressible, deep-atmosphere equations of motion (Wood et al., 2014).

The boundary layer scheme is based on that described in Lock et al. (2000) with updates described in Walters et al. (2019). The subgrid turbulence scheme is based on Smagorinsky (1963) with multiple extensions from Lock et al. (2000). We use Rayleigh damping of all prognostics in a “sponge layer” in the upper levels of the model, with the damping timescale following an exponential function of height from 24-40 km. The microphysics used is a single-moment scheme based on Wilson and Ballard (1999).

The default radiation scheme, which is used in UKMOi-vn11.0-RA1-T and studied in Chapters 3 and 4, is the Suite of Community Radiative Transfer codes based on Edwards and Slingo (SOCRATES) (Edwards and Slingo, 1996). The spectral files used are those associated with the UM Global Atmosphere 3.0 (GA3.0, Walters et al., 2011) which has 6 spectral bands in the shortwave, and 9 in the longwave. The full radiation calculations are computed at 15-minute time steps and simplified radiation calculation are made at 5-minute time steps. In Chapter 5, we use a different radiation scheme that allows us to systematically modify cloud-longwave interactions. This will be discussed later in Section 5.2.1.

### 2.3 Variance of Normalised FMSE Budget

Using the variance of vertically-integrated FMSE ( $\text{var}(\hat{h})$ ) as the metric for comparing aggregation across different SSTs has its disadvantages as it is very strongly dependent on temperature. To account for this, we normalise vertically-integrated FMSE between a hypothetical upper and lower limit based on the SST using Equation (2.1), yielding values of normalised FMSE ( $\hat{h}_n$ ) between 0 and 1.

$$\hat{h}_n = \frac{\hat{h} - \hat{h}_{\min}}{\hat{h}_{\max} - \hat{h}_{\min}} \quad (2.1)$$

Here, hats ( $\hat{\phantom{x}}$ ) denote a density-weighted vertical integral, and  $\hat{h}_{\max}$  and  $\hat{h}_{\min}$  are the upper and lower limits of  $\hat{h}$  for a given SST.  $\hat{h}_{\max}$  is defined as the vertically-integrated FMSE of a fully saturated moist pseudoadiabatic profile from the surface to the tropopause, plus the integrated FMSE of the initial profile above the tropopause. For  $\hat{h}_{\min}$ , the vertically-integrated FMSE of a dry adiabatic profile with zero moisture is used within the troposphere, and again, integrated FMSE above the tropopause from the initial profile is added. The SST is used as the temperature at sea-level pressure to initiate both adiabatic profiles. The tropopause is defined as the lowest level in the initial profile at which the lapse rate

---

decreases to 2°C/km or less. The values of  $\hat{h}_{\max}$  and  $\hat{h}_{\min}$  for the UKMO-RA1-T model are shown in Table 2.1, along with the height and pressure of the tropopause and the integrated FMSE above it. With less than 11% of the mass-weighted integral of  $\hat{h}_{\max}$  and  $\hat{h}_{\min}$  coming from the FMSE above the tropopause, the way we define the tropopause has little effect on these limits and does not impact our conclusions. Note that these values for  $\hat{h}_{\max}$  and  $\hat{h}_{\min}$  are used for all UM simulations throughout this thesis, however,  $\hat{h}_{\max}$  and  $\hat{h}_{\min}$  are calculated separately for all RCEMIP simulations. The difference between  $\hat{h}_{\max}$  and  $\hat{h}_{\min}$  does not vary by more than 8% between the RCEMIP models for a given SST.

Table 2.1: Values of  $\hat{h}_{\max}$  and  $\hat{h}_{\min}$  for each SST used in Equation (2.1) to normalise  $\hat{h}$ .

SST (K)	$\hat{h}_{\min}$ ( $GJ m^{-2}$ )	$\hat{h}_{\max}$ ( $GJ m^{-2}$ )	Tropopause Pressure (hPa)	Tropopause altitude (km)	$\hat{h}$ above tropopause ( $GJ m^{-2}$ )
295	3.177	3.563	92.0	16.1	0.386
300	3.228	3.753	91.3	16.6	0.387
305	3.272	3.988	80.0	17.9	0.348

For all of our SSTs, variations in  $\hat{h}_n$  are dominated by horizontal variations in moisture. By computing the individual components of  $\hat{h}$  from the terms in Equation (1.1), we find the horizontal variance of the thermal energy component of  $\hat{h}$  is approximately 0.5% of the variance of the moisture component of  $\hat{h}$  for all SSTs. The variances of the geopotential energy and ice content terms are negligible in comparison to the variance of the moisture term. Average anomalies in the moisture component of  $\hat{h}$  increase exponentially with SST and are proportional to the difference between  $\hat{h}_{\min}$  and  $\hat{h}_{\max}$ . Therefore, this normalisation technique approximately eliminates the SST dependence of  $\text{var}(\hat{h})$ .

The relative importance of different processes to changing the variance of FMSE can be analysed using the budget equation derived by Wing and Emanuel (2014) as shown in Equation 1.2 in Chapter 1. This equation is suitable for comparing the importance

of different  $\widehat{h}$  feedbacks to aggregation within models at the same SST. However, due to the strong dependence of  $\text{var}(\widehat{h})$  to SST, this equation cannot be used to analyse how the importance of these feedbacks to aggregation change with SST. To enable fair comparisons of aggregation with SST, we frame our analysis using a budget of the horizontal variance of  $\widehat{h}_n$ . By following the budget equation derivation by Wing and Emanuel (2014) and using  $\widehat{h}_n$  instead of  $\widehat{h}$ , Equation (1.2) becomes:

$$\frac{1}{2} \frac{\partial \widehat{h}_n'^2}{\partial t} = \widehat{h}_n' LW_n' + \widehat{h}_n' SW_n' + \widehat{h}_n' SEF_n' - \widehat{h}_n' \nabla_h \cdot \mathbf{u} \widehat{h}_n \quad (2.2)$$

Here, each of the three normalised flux anomalies on the RHS ( $LW_n'$ ,  $SW_n'$ , and  $SEF_n'$ ) is equal to the original flux anomaly in Equation (1.2) divided by the difference between  $\widehat{h}_{\max}$  and  $\widehat{h}_{\min}$ . The derivation of this equation is shown in the appendix.

In Wing and Emanuel (2014), the budget terms are normalised by the instantaneous FMSE variance, which results in a couple of differences from our method. Firstly, as the variance of FMSE increases, the magnitude of their terms tends to decrease because the terms are divided by a larger value, whereas the terms in Equation (2.2) tend to increase in magnitude as  $\widehat{h}_n'$  is a factor in every term. The SST sensitivity of the terms may also be different if the degree of aggregation (as measured by normalised FMSE variance) changes with SST. For example, if aggregation increases with SST, then Wing and Emanuel (2014) would find the magnitude of the budget terms decrease with SST as the terms are divided by a much larger FMSE variance, whereas following Equation (2.2),  $\widehat{h}_n'$  would increase and therefore the individual terms increase with SST. If the degree of aggregation is similar across all SSTs as measured by  $\text{var}(\widehat{h}_n)$ , then the SST dependence of the budget terms will be very similar during the mature stage of aggregation regardless of which normalisation method is used.

A drawback of the  $\text{var}(\widehat{h}_n)$  budget framework is that it is a vertically-integrated framework that is not able to quantify the effects of processes occurring at specific vertical

levels. Studies have shown that there are many low-level processes that are important for aggregation. For example, Muller and Held (2012) highlight the importance of shallow, radiatively-driven circulations caused by cooling atop shallow clouds in dry regions, yielding an upgradient transport of FMSE, inducing a positive aggregation feedback. Jeevanjee and Romps (2013) describe how cold pools are responsible for the domain size dependence of self-aggregation. Boundary layer processes are key for the production of available potential energy that is associated with the development of self-aggregation (Yang, 2018a), and are theorised to determine the length scale of aggregation (Yang, 2018b). The use of our vertically-integrated framework means the effects of these processes are not directly studied. However, circulations that are induced by diabatic forcing are included in the vertically-integrated advection term in the  $\text{var}(\widehat{h}_n)$  budget framework. So the radiation and surface flux terms only account for the *direct* diabatic feedbacks.

There is still great value in the use of the  $\text{var}(\widehat{h}_n)$  budget framework to study the direct diabatic feedbacks. Previous studies have shown that these feedbacks are key drivers and maintainers of aggregation, and this framework allows us to easily quantify and compare these feedbacks across a range of models and SSTs.

## CHAPTER 3

# CLOUD-RADIATION INTERACTIONS AND THEIR CONTRIBUTIONS TO CONVECTIVE SELF-AGGREGATION

### Opening remarks

The work in this chapter has been published as Pope et al. (2021) and is only slightly modified as a thesis chapter from the original publication. Part of the Introduction and some of the Methods regarding the normalised FMSE variance budget framework and model configuration in the original publication have been moved to Chapters 1 & 2, as they are also relevant in the following chapters.

### 3.1 Introduction

Previous studies have shown that interactions between radiation and convection are crucial drivers and maintainers of aggregation (e.g. Bretherton et al., 2005; Holloway and Woolnough, 2016; Becker et al., 2017). Some studies have further shown that cloud radiative effects are important (e.g. Wing and Emanuel, 2014; Wing and Cronin, 2016) by comparing the total longwave feedback to the clear-sky feedback. However, a detailed investigation

into the importance of radiative interactions with different cloud types is missing. By studying in detail the cloud-radiation interactions affecting aggregation within a set of idealised simulations, this chapter begins to answer the second thesis objective.

In this chapter, we investigate the direct radiative-convective processes that are important to self-aggregation, and their sensitivity to SST within elongated channel simulations of the UK Met Office Unified Model (UM) version 11.0. We then investigate how the SST-dependent convective features and their radiative interactions are affected by model grid spacing and treatment of subgrid condensation using smaller square domains. Our simulations are configured using three fixed sea surface temperatures (SSTs) following the Radiative-Convective Equilibrium Model Intercomparison Project (RCEMIP) protocol (Wing et al., 2018, and briefly described in Section 2.1), and the model configurations are described in Section 2.2. We use a budget equation for the variance of normalised vertically-integrated FMSE which minimises the SST dependence of horizontal FMSE variance (described in Section 2.3). This allows us to compare how the impacts of radiative feedbacks on aggregation change with SST. We categorise cloud types based on the vertical distribution of condensed water content and analyse their radiative interactions that impact aggregation. This categorisation is shown in Section 3.2.2.

We first analyse how convection aggregates within the three large channel simulations in Section 3.3, and show how the FMSE budget terms vary with time and SST. We then analyse the radiative feedbacks responsible for maintaining aggregation in the large domain and compare how SST affects these feedbacks in Section 3.4. Then, we look at the dominant radiative feedbacks during the early stages of aggregation and see how they change with time (Section 3.5). Finally, we investigate how these radiative interactions are affected by both resolution and the critical humidity threshold for condensation to occur ( $RH_{crit}$ ), using smaller domains with lower grid spacing (Section 3.6). A summary and conclusions is presented in Section 3.7.

## 3.2 Methods

### 3.2.1 Data and Analysis Framework

In this study, we use the UK Met Office Unified Model version 11.0 to simulate RCE at three fixed SSTs: 295, 300 and 305 K. This study mainly focuses on convection within the “*LARGE*” simulations; 6048 km  $\times$  432 km elongated channel simulations with a 3 km horizontal grid spacing. However, we also use three smaller 100 km  $\times$  100 km domains: “*SMALL*” (1 km grid spacing), “*SMALL\_RHCRIT*” (1 km grid spacing), and “*SMALL\_HI*” (0.1 km grid spacing), to assess how the radiative properties of clouds are affected by the critical humidity threshold for condensation (RHcrit) and grid spacing. The models used in this study are described in more detail in Section 2.2.

We use the variance of normalised vertically-integrated frozen moist static energy budget framework to measure and analyse convective aggregation in this study. This framework is described in Section 2.3.

### 3.2.2 Cloud Classification Scheme

The cloud classification scheme is based on Hill et al. (2018), using the vertical structure of condensed water content to define different cloud types. High-level clouds are defined to be located above an upper-level pressure threshold, low-level clouds are located below a lower-level threshold, and mid-level clouds are anything in between. Clouds spanning two or more levels have their own categories. In this study, a gridbox is defined as being cloudy when its condensed water content exceeds  $10^{-6}$  kg m $^{-3}$ . This is the approximate limit below which the average difference between the longwave and shortwave heating rates of clear-sky (without condensed water) and total radiative transfer calculations are less than 1 K day $^{-1}$ , and an order of magnitude lower than the value for mean cloud condensed amount (analysis not shown).

We use different high and low cloud pressure level thresholds for each SST to account

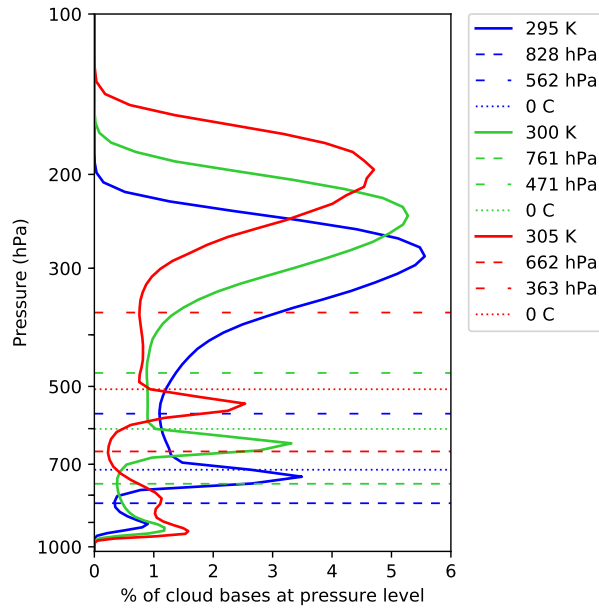


Figure 3.1: Cloud base distributions throughout each of the *LARGE* domain simulations. The lower and upper pressure thresholds (P1 and P2) for each SST are shown in narrow and wide dashed lines respectively, and the mean freezing level is shown in dotted lines.

for the change in depth of the troposphere. The thresholds for a given SST are determined from the average vertical profile of cloud bases throughout the entire *LARGE* domain simulation. Distributions of cloud base pressures for each of the *LARGE* simulations are shown in Figure 3.1. The cloud base at a given column is calculated as the lowest-altitude pressure at which the condensed water content exceeds  $10^{-6} \text{ kg m}^{-3}$  (the distribution shown, therefore, does not account for additional cloud bases above the lowest base). The profiles of cloud base have very similar features for each SST, with two consistent local minima within each distribution. These two minima will be the chosen pressure thresholds that define the cloud types throughout this study. The lower-level threshold is defined as the first cloud base distribution local minimum below the freezing level. The upper-level threshold is the highest-altitude cloud base distribution local minimum. The lower-level thresholds (P1), and the upper-level thresholds (P2) for each SST are shown in Figure 3.1.

Rather than using all 12 cloud types used by Hill et al. (2018), we have merged the cloud

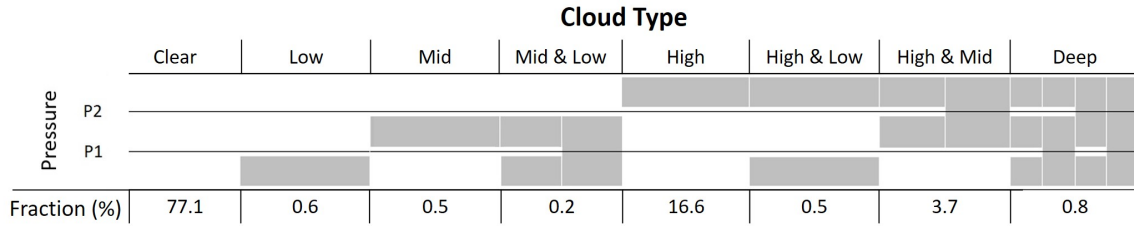


Figure 3.2: Schematic of the categories used in this study. P1 and P2 are the lower-level and upper-level pressure thresholds respectively. The shading is contiguous across rows if the cloud type extends across multiple layers. The mean domain fractions for each cloud type throughout the entirety of the *LARGE*, 300 K SST simulation are shown. Note that fractions are sensitive to aggregation and SST.

types that were only distinguishable by whether or not they are vertically contiguous. We analysed radiative heating rates for all 12 cloud types, and found that the types we have merged have similar heating rates for a given condensed water path (CWP) (not shown). The merged cloud types also have similar  $\hat{h}$  distributions, meaning they will have similar radiative interactions for a given CWP. The main differences between the individual cloud types is their CWP distributions, with the contiguous types tending to have higher CWPs. We end up with 8 cloud types used in this study, including Clear regions. A schematic of the categories is shown in Figure 3.2.

### 3.3 Aggregation within the *LARGE* Domain

Within the first five hours of our simulations, convection initiates rapidly and homogeneously, with scattered convection appearing across the entire domain. After a couple of days, dry regions begin to develop, within which, deep convection is suppressed. These dry regions begin to grow in size and subsequently become drier, reminiscent of the radiatively-driven cold pool process described in Coppin and Bony (2015). As the dry regions expand and merge, the moist regions become increasingly confined and become moister. The most prevalent dry regions are usually surrounded by the most intense convection. Dry regions continue to expand, constricting the moist regions until an equilibrium state is reached

with quasi-stationary bands of intense convection being separated by dry regions with little cloud. This evolution is consistent with the majority of non-rotating large-domain simulations of RCE (Wing et al., 2017, 2020).

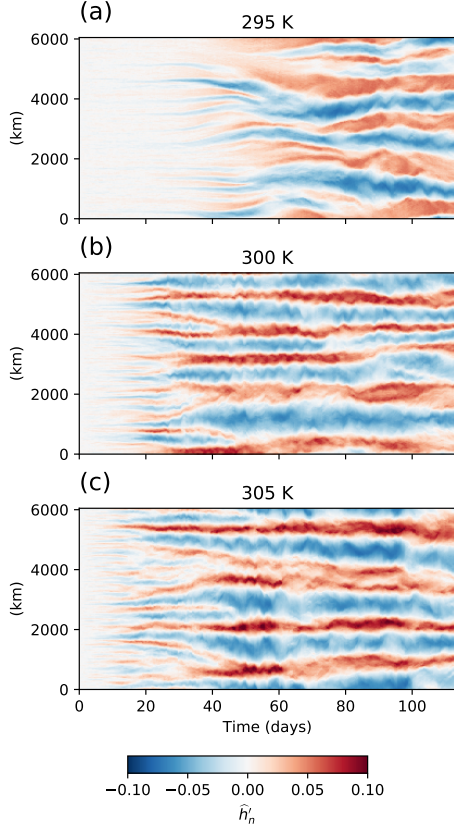


Figure 3.3: Hovmöller diagrams of  $\hat{h}_n$  for each SST for the *LARGE* domain runs.  $\hat{h}_n$  is averaged across the short axis of the domain.

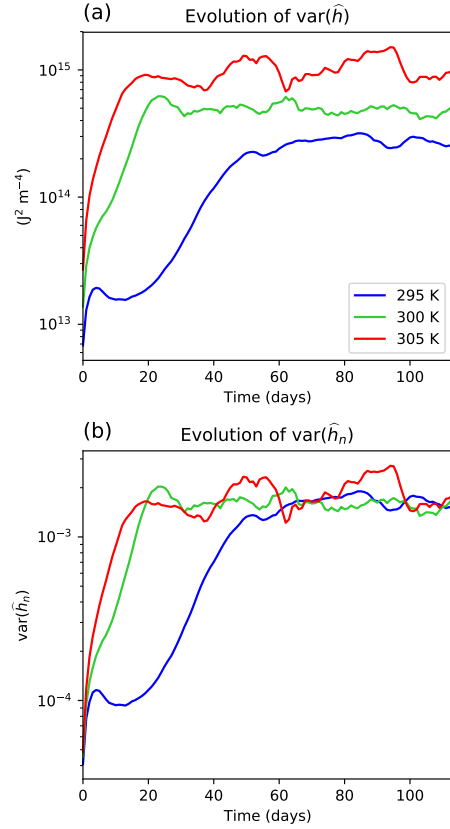


Figure 3.4: Daily means of the (a) spatial variance of  $\hat{h}$ , and (b) spatial variance of  $\hat{h}_n$ , for each SST for the *LARGE* domain.

Hovmöller plots for each simulation are shown in Figure 3.3 using  $\hat{h}_n$  as a proxy for moist convective regions. The Hovmöller diagrams were made by averaging  $\hat{h}_n$  along the short axis of the domain. The evolution of the variance of column-integrated FMSE for each SST is shown in Figure 3.4a. Visually, this metric has a strong correlation with SST since a warmer atmosphere is able to contain exponentially more water vapour via the

Clausius-Clapeyron relationship, so there will be a larger difference in FMSE between the dry and moist regions. Normalisation allows for fair comparisons of aggregation across all SSTs whilst using the FMSE variance framework, as shown in Figure 3.4b.  $\text{Var}(\hat{h}_n)$  is a consistent metric for each SST, with values less than  $10^{-4}$  corresponding to uniformly scattered convection, and values greater than  $10^{-3}$  corresponding to strong convective aggregation. Aggregation via this metric reaches a similar level once the convective aggregation is in equilibrium despite convection organising into four bands in the 305 K simulations and five in the other simulations. We note however that when considering multiple metrics of convective aggregation for these simulations there is no agreement on the SST sensitivity of aggregation in the final equilibrium state. Wing et al. (2020) found that the subsidence fraction and the organisation index ( $I_{\text{org}}$ ) both increase with SST for these simulations, indicating that the convection forms into more constricted bands as SST increases, whereas the variance of column relative humidity slightly decreases with SST.

Considering the Hovmöller plots in Figure 3.3, the fully-aggregated state is reached around day 50 for the 300 K and 305 K simulations and around day 75 for the 295 K simulation. This difference in aggregation rate can be attributed to the ability of dry regions to expand and amplify. In the 300 K and 305 K simulations, the dry patches that form very early on merge, amplify and continue to expand until the equilibrium state is reached. However, in the 295 K simulation these patches struggle to amplify and are easily remoistened, allowing convection to reoccur in that location – more persistent dry patches begin to develop around day 15 and slowly expand and confine the convection to form the quasi-stationary bands.

The points in time at which the variances of  $\hat{h}$  level off in Figure 3.4 appear to occur earlier than the points in time at which the convection appears fully aggregated in Figure 3.3 particularly for the 300 K and 305 K simulations. This could in part be due to the averaging along short axis of the domain for the Hovmöller diagrams, smoothing out

any features that do not extend across the entire short axis. However, once the moist regions no longer get moister, and the dry regions no longer become drier,  $\text{var}(\hat{h})$  will reach its maximum value. This shows that there can be spatial reorganisation of the convective aggregation without a change in  $\text{var}(\hat{h})$ . It may only take around the timescale of a convective cell for a column to reach the upper limit of  $\hat{h}$ , however it takes much longer for the driest regions to reach the lower limit. The drying of the dry regions may be on the same timescale as the subsidence timescale; the time it takes for the very dry air near the tropopause to descend throughout the depth of the free troposphere.  $\text{Var}(\hat{h})$  correlates strongly with aggregation, although it does not necessarily indicate how clustered the convection is once the maximum variance is reached. This is not a surprising result. Beucler and Cronin (2019) relate the evolution of the length-scale of convection aggregation to the FMSE budget terms, showing that the processes that increase FMSE variance are not always the processes that increase the length-scale of aggregation. This allows convection to spatially reorganise without changing FMSE variance.

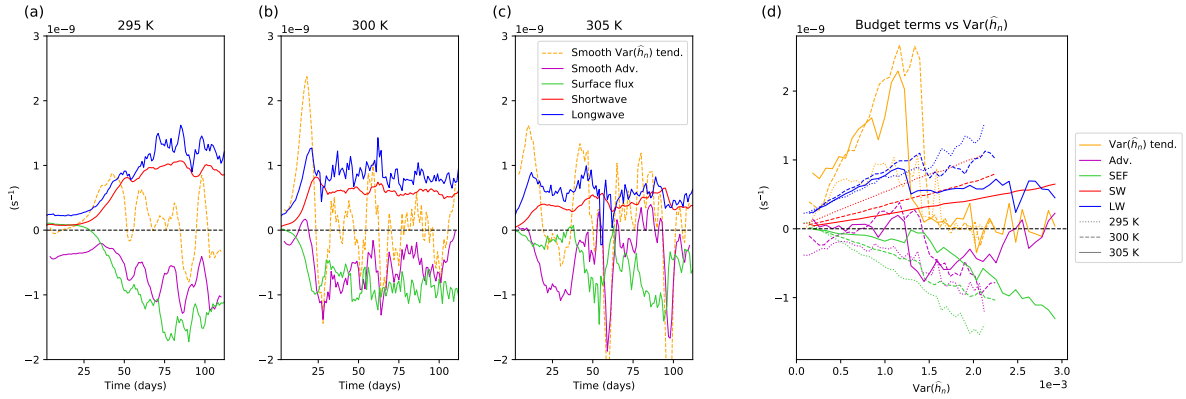


Figure 3.5: Domain-mean of terms in Equation (2.2) for (a) 295 K, (b) 300 K, (c) 305 K within the *LARGE* domain. Each point represents a daily mean of the term. The advection term is calculated as a residual of the other terms. Both the  $\text{var}(\hat{h}_n)$  tendency and the advection term are 5-day running averages, shown to reduce noise. (d) Mean of each term against  $\text{var}(\hat{h}_n)$  calculated for 40 evenly-spaced  $\text{var}(\hat{h}_n)$  bins.

Time series of the domain-mean values of the terms in the  $\text{var}(\widehat{h}_n)$  budget (Equation 2.2) are shown in Figure 3.5a-c. Where the terms are positive, they are contributing to an increase in  $\text{var}(\widehat{h}_n)$ , and hence encourage aggregation (note that the advection term is calculated as a residual of the other terms). Figure 3.5d shows the mean values of the budget terms for a given degree of aggregation for each SST in terms of  $\text{var}(\widehat{h}_n)$ . From this, the SST dependence of the budget terms can be seen throughout the aggregation process. The growth phase of aggregation can be seen where the  $\text{var}(\widehat{h}_n)$  tendency is strongly positive (typically where  $\text{var}(\widehat{h}_n) < 1.4 \times 10^{-3}$ , compare with Figure 3.4b) and the maintenance phase is where the tendency is close to 0. The magnitude of all terms tends to increase as  $\text{var}(\widehat{h}_n)$  increases since each term in the equation is a product that includes  $\widehat{h}'_n$ .

The longwave feedback is the main driver of aggregation in each of our simulations, with its contribution to aggregation insensitive to SST during the growth phase. Most studies are in agreement that the longwave feedback is a strong positive driver of aggregation, whereas Wing and Cronin (2016) found that the longwave feedback increases with SST. They find that this SST dependence is mainly due to clouds. This is because at lower SSTs, the atmosphere is drier, making the infrared atmospheric windows much more transparent. The atmosphere is then a poor emitter of longwave radiation because it is optically thinner at these wavelengths. They hypothesise that the presence of clouds in the moist regions increases radiative cooling by increasing the number of longwave emitters, hence decreasing the longwave feedback. Specifically, the presence of low clouds would have a larger effect than high clouds as their warm cloud tops would emit more radiation. Our simulations have a distinct lack of low cloud compared to most cloud-resolving models (Wing et al., 2020), and this may be the reason we do not see this trend. We find the longwave feedback is also the dominant maintainer of aggregation, however its contribution to maintenance falls with SST. This is discussed further in Section 3.4.1.

The shortwave feedback is always positive and is highly sensitive to SST, with higher

SSTs having smaller shortwave feedbacks. Its contribution to driving aggregation is small compared to the longwave term especially for warmer SSTs, though it is roughly three quarters of the magnitude of the longwave feedback during the maintenance phase. These results are in agreement with Wing and Cronin (2016) and are discussed further in Section 3.4.3.

A more surprising result is the magnitude of the surface flux feedback which is a strong negative feedback at all stages and SSTs except for the very earliest stages of aggregation. This is in contrast to the majority of studies which find the surface flux feedback to be one of the dominant drivers of self-aggregation (Wing et al., 2017). Wing and Emanuel (2014) describe two opposing surface flux feedbacks at play. Firstly, surface wind speeds are higher in moister regions resulting in a positive feedback which helps drive aggregation. On the other hand, there is enhanced evaporation in the dry regions due to enhanced air-sea enthalpy disequilibrium resulting in a negative feedback. Typically the former feedback dominates at early stages, whereas the latter is more relevant for aggregated convection (Wing et al., 2017). The surface flux feedback is also highly sensitive to SST, with higher SSTs generally having a less negative surface flux feedback. The reasons for the surface flux feedback’s sensitivity to aggregation and SST are not investigated.

Figure 3.5d shows the sum of all the diabatic feedbacks (longwave, shortwave and surface flux terms) is similar at all stages of aggregation in each of our simulations, however the rate of change of aggregation increases with SST. The aggregation rate increases with SST because of the SST sensitivity of the advection term. At early stages of aggregation ( $\text{var}(\hat{h}_n) < 0.8 \times 10^{-3}$ ) the (usually negative) advection feedback becomes increasingly positive as SST increases and is approximately zero for the 305 K simulation. This accelerates the aggregation process for higher SSTs. Muller and Bony (2015) highlight the importance of radiatively driven circulations from low clouds that result in upgradient transport of FMSE resulting in a positive feedback. Despite our simulations having a notable lack of low cloud, the average fraction of low-level cloud increases from 1.4% at 295 K to 3.2% at

305 K, and may be a factor in explaining the SST dependence of the advection term. We do not explore the reason for this relationship further.

There are two occasions in the 305 K simulations in which  $\text{var}(\widehat{h}_n)$  rapidly decreases. These are between days 55 & 60, and days 95 & 100 (Figure 3.4). Approximately five days prior to  $\text{var}(\widehat{h}_n)$  decreasing, the intensity of the convection in the moist bands begins oscillating with a period of 2 to 5 days. The convection can become so intense that anvil clouds spread far away from the convective updrafts and over the driest regions of the domain. This creates anomalous longwave heating over anomalously dry regions (relative to the instantaneous domain-mean), resulting in a sharp decrease in the domain-mean longwave term (Figure 3.5c days 55 & 95). The intense convection might also generate intense circulations that transport high  $\widehat{h}$  away from moist regions, creating the strongly negative advection feedbacks which ultimately cause  $\text{var}(\widehat{h}_n)$  to fall. These events are not directly caused by radiation-convection interactions so they are not investigated further in this study.

In Section 3.4, we discuss radiation-FMSE interactions during the “Mature” phase of aggregation, and we discuss the “Growth” phase of aggregation in Section 3.5. We define the Mature phase of aggregation to be after the time at which the convection is most clustered (after day 75 for the 295 K simulation, and after day 50 for the 300 K and 305 K simulations, following Figure 3.3) and where  $\text{var}(\widehat{h}_n)$  is between  $1.5 \times 10^{-3}$  and  $2 \times 10^{-3}$ . This  $\text{var}(\widehat{h}_n)$  range was chosen because the mean  $\text{var}(\widehat{h}_n)$  tendency is close to zero for each SST (Figure 3.5d) and the simulations are within this range for a sizeable duration (Figure 3.4b). Fluctuations in  $\text{var}(\widehat{h}_n)$  outside this range will not bias the results. The Growth phase is sampled for  $\text{var}(\widehat{h}_n)$  between  $3 \times 10^{-4}$  and  $4 \times 10^{-4}$ . This is an arbitrary range – using any range in which aggregation increases rapidly for all SSTs does not affect the conclusions of these results. We have chosen these narrow ranges to compare convection at similar stages of aggregation, with FMSE anomalies being similar in magnitude.

### 3.4 Cloud Type Contributions during the Maintenance of Aggregation

Interactions between radiation and cloud/moisture responses to convection have been shown to be crucial contributors to convective self-aggregation (e.g. Arnold and Putman, 2018; Wing et al., 2017). In this section, we investigate the impacts of cloud-radiative interactions on the maintenance of self-aggregation during the Mature phase of aggregation within our *LARGE* simulations. Figures presented in Sections 3.4.1 and 3.4.2 also display data for the Growth phase of aggregation which are discussed in Section 3.5.

Note that results presented here are limited to our specific simulations. They are outliers in RCEMIP in a number of ways, so the results might not be representative of all RCE simulations. Wing et al. (2020) report that in terms of cloud fraction, our *LARGE* simulations have roughly one fifth of the low-level cloud fraction compared to the mean of the other RCEMIP cloud resolving models, but they also have one of the largest high-cloud fractions.

The radiative heating rate of an atmospheric column is determined by the difference between the radiative fluxes into the atmosphere and the radiative fluxes out. The only longwave flux into the atmosphere is the upwelling surface radiation which is uniform in space and time in our simulations, owing to the fixed SST. Therefore, the longwave heating rate is determined by the magnitudes of the downwelling flux into the surface and the outgoing longwave radiation (OLR). These fluxes are sensitive to the emission heights and opacities of different layers, which in turn depend on the profiles of cloud and moisture. Net longwave radiation into the atmosphere is always negative, but longwave cooling can be strongly reduced with the presence of optically-thick high cloud.

Incoming solar radiation is the main source of shortwave radiation into the atmosphere (surface albedo is 0.07 in our simulations). Water vapour is an excellent absorber of shortwave radiation, so the column humidity will have a major effect on the shortwave

heating rates. Clouds are also good absorbers of shortwave radiation and act to increase the amount of diffuse radiation, allowing more radiation to be absorbed by cloud and water vapor. However, they are also good reflectors, resulting in clouds having either a positive or negative influence on atmospheric shortwave heating (Wing and Cronin, 2016).

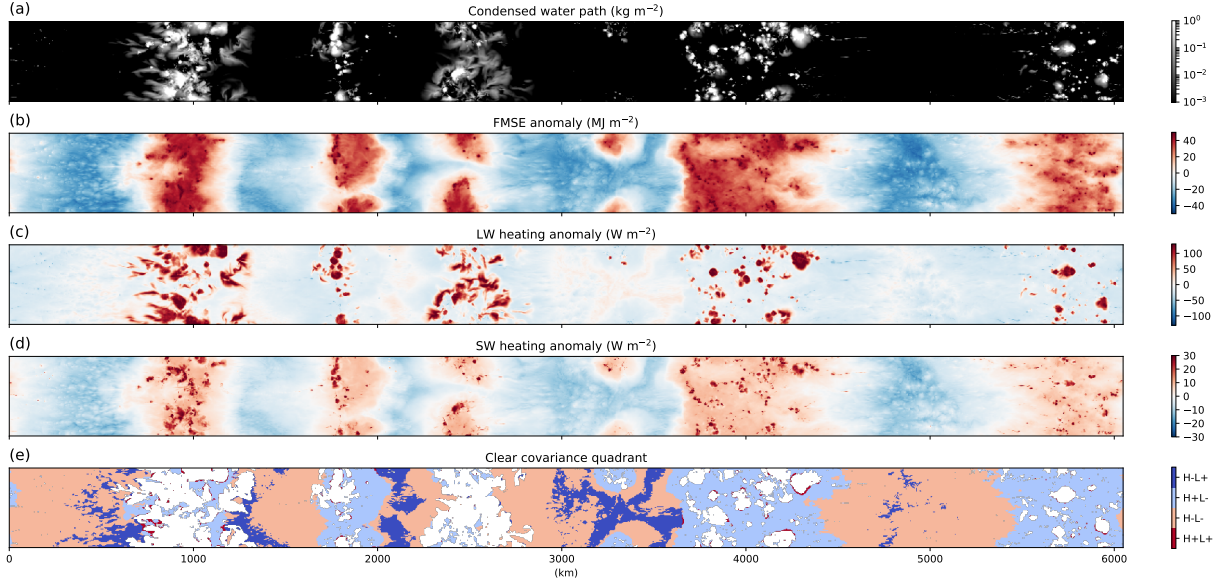


Figure 3.6: Maps of (a) condensed water path ( $\text{kg m}^{-2}$ ), (b) FMSE anomaly ( $\text{MJ m}^{-2}$ ), (c) longwave heating anomaly ( $\text{W m}^{-2}$ ), (d) shortwave heating anomaly ( $\text{W m}^{-2}$ ), (e) Clear covariance quadrant (Section 3.4.2) - note that clouds are coloured white in (e). Snapshots taken at day 100 in the *LARGE* domain with  $\text{SST} = 300 \text{ K}$ . Regions where the FMSE anomaly (“H”) and radiative heating anomaly (“L”) have the same sign contribute to increasing  $\text{var}(\hat{h})$ . Note that the FMSE, shortwave and longwave anomalies relative to the instantaneous domain mean and are not normalised.

From Figures 3.6a & c, we see a strong connection between cloud and net longwave heating. As previously noted, there is a distinct lack of low cloud in our simulations, so the vast majority of cloud in this figure are high-topped clouds. These high-topped cloud regions have an average longwave heating anomaly of  $+47 \text{ W m}^{-2}$  relative to the domain mean, with the thicker clouds tending to have higher anomalies. The remaining cloud type regions have an average longwave anomaly of  $-16 \text{ W m}^{-2}$ , and the clear regions have an average of  $-11 \text{ W m}^{-2}$ . The shortwave heating rates are very strongly correlated with

$\widehat{h}'$ . With changes in  $\widehat{h}$  stemming from changes in water vapor, shortwave heating rates depend mostly on the amount of water vapour in the column, and 99% of the shortwave heating anomalies fall in the range of  $-15$  to  $28 \text{ W m}^{-2}$ . Note that radiative fluxes are output as hourly-averaged variables whereas FMSE and 3D data (including cloud type classification) are instantaneous snapshots.

We wish to study how the radiative feedbacks of each cloud category contribute to the  $\text{var}(\widehat{h}_n)$  tendency of the entire domain. Since both radiative anomalies and FMSE anomalies are calculated at each grid point, the instantaneous values of the radiative terms in Equation (2.2) can also be calculated at each point across the domain. Then, by knowing the cloud type at each grid point, the contributions of each category to the domain-mean radiative terms can be found.

Note that this approach does not describe the cloud-only effect, and since the anomalies of FMSE and radiation also depend on the domain-mean,  $\text{var}(\widehat{h}_n)$  is not purely a local metric. We only consider the column-integrated cloud-radiative feedbacks here, although indirect radiative interactions with cloud are shown to be important via the generation of circulations (e.g. Muller and Held, 2012; Muller and Bony, 2015; Holloway and Woolnough, 2016). Nevertheless, we find the approach to be a useful way to compare the relative importance of each cloud type's direct radiative contribution to self-aggregation across a range of SSTs.

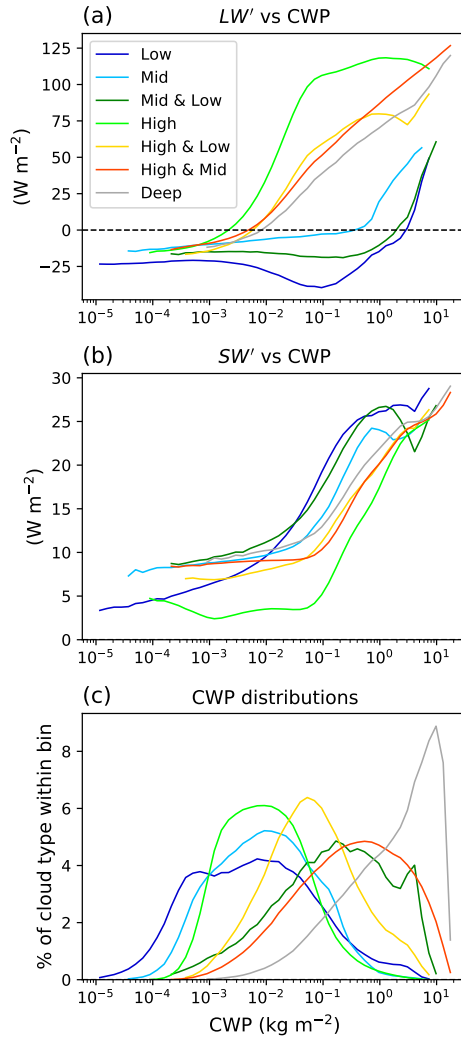


Figure 3.7: (a) Longwave and (b) shortwave radiative heating anomalies vs condensed water path for each cloud type (defined in Section 3.2.2), and (c) distributions of condensed water path for each cloud type. Data from the *LARGE*, 300 K SST simulation during the Mature phase. 50 bins are spaced logarithmically throughout the CWP range. The percentage shown in (c) is the percentage of each cloud type within a given bin.

To begin to quantify the longwave and shortwave heating effects of clouds, the mean radiative anomalies of each cloud type (defined in Section 3.2.2) for a given CWP are shown in Figure 3.7a & b. The radiative heating in both the longwave and shortwave

varies strongly with CWP. The cloud type is also a very important factor in the radiative anomalies, particularly in the longwave. For a given CWP, High clouds have the largest column longwave heating rates since they have cold cloud tops, resulting in low outgoing longwave radiation (OLR). This effect, combined with relatively little emission to the surface, leads to strongly positive longwave heating anomalies. Low clouds have warm tops and warm bases, so they effectively emit longwave radiation to space as well as to the surface, cooling the column faster than Clear regions. Deep clouds have longwave heating rates in between High and Low clouds for a given CWP. For a given total CWP, they have less optically thick high-level cloud than High clouds, allowing more radiation to be transmitted from the warmer lower levels. In addition, their low, warm bases strongly emit towards the surface, further decreasing the column radiative heating.

In the shortwave, each cloud type's heating rate increases with CWP, although this is largely due to increased shortwave absorption by water vapour within these columns (as shown in Wing and Emanuel (2014) and Section 3.4.3). However, there is some dependence on cloud type due to the high reflectivity of clouds. Columns with Low clouds typically have the highest shortwave heating rates. Their low cloud top height allows lots of shortwave radiation to be absorbed by water vapour. The radiation they reflect may also be absorbed by water vapour above the cloud. High clouds have the lowest shortwave heating rates as they reflect a large amount of solar radiation before it can be absorbed by the water vapour below.

The distributions of CWP for each cloud type are shown in Figure 3.7c. These distributions, paired with the dependence of the radiative anomalies on CWP, determine the mean radiative anomalies for each cloud category (domain-averaged heating rates of all categories are shown in Figures 3.9e-g). Despite the High clouds having the largest longwave heating rate for a given CWP, their CWP distribution peaks at around  $0.01 \text{ kg m}^{-2}$ , corresponding to a longwave heating anomaly of roughly  $20 \text{ W m}^{-2}$ . In contrast, the High & Mid cloud has a peak CWP around  $0.5 \text{ kg m}^{-2}$  corresponding to a longwave heating

anomaly around  $70 \text{ W m}^{-2}$ . This results in High clouds having only the fourth largest domain-averaged longwave heating rates out of all categories.

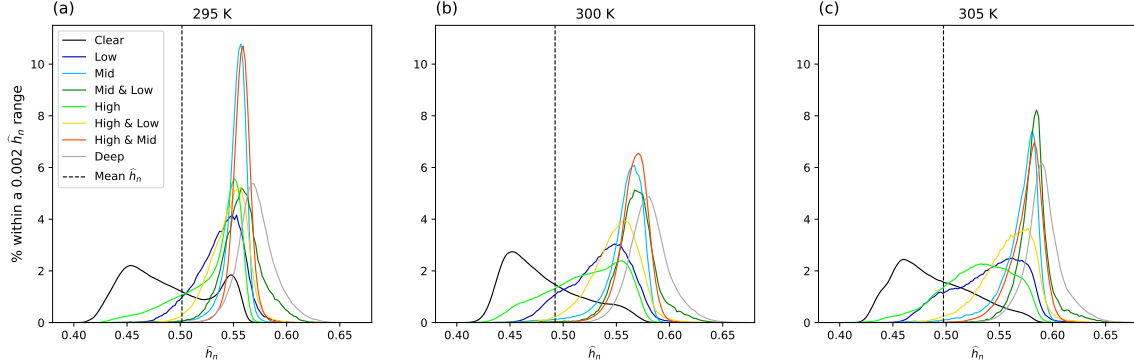


Figure 3.8: Distributions of  $\hat{h}_n$  for each cloud type for all SSTs within the *LARGE* domain during Mature phase. The vertical dashed line indicates the domain-mean  $\hat{h}_n$  throughout the Mature phase. Note that each curve is normalised individually.

Distributions of  $\hat{h}_n$  during the Mature phase of the *LARGE* simulations for each cloud category are shown in Figure 3.8. The vast majority of clouds occur within anomalously high  $\hat{h}_n$  regions, with only a few High and Low clouds occurring with negative  $\hat{h}'_n$ . High clouds have the largest spread of  $\hat{h}_n$  out of all the cloud types as they can extend hundreds of kilometres away from the updraft, spanning a wide  $\hat{h}_n$  range. Low clouds occur within a broad span of  $\hat{h}_n$  as they can form under a wide range of conditions. At higher  $\hat{h}'_n$  regions, Low clouds form and may continue to develop into congestus and cumulonimbus, as the environment is favourable for deep convection. At lower  $\hat{h}'_n$  regions, descending motion throughout the free troposphere increases stability and reduces humidity, making the atmosphere unfavourable for deep convection, but shallow cumulus may still form atop the well-mixed boundary layer. The majority of the other cloud types are associated with deep convection, which only occurs within high  $\hat{h}'_n$  regions, where the environment is favourable for updraft development. Whilst the domain-mean  $\hat{h}'_n$  for the Clear regions is slightly negative, there is a very large spread in the distribution of  $\hat{h}_n$ , with just under half of the Clear regions having positive anomalies.

The domain-mean  $\widehat{h}_n$ , as well as its lower limit, remain very similar with SST. The upper limit increases slightly with SST, as does the mean  $\widehat{h}_n$  for most cloud types. We do not have a good explanation for this phenomenon.

### 3.4.1 Longwave Cloud Interactions

The contribution of each cloud category to the radiative terms can be calculated by multiplying their mean covariance between the normalised radiative and  $\widehat{h}$  anomalies by their cloud fraction. Figure 3.9a shows that it is the Clear, High, High & Mid, and Deep categories that have the largest contribution to the longwave term during the Mature phase (compare open circles representing the Mature phase), with the magnitude of their contributions being highly sensitive to SST. The contributions of the Low, Mid, Mid & Low and High & Low categories have a relatively insignificant contribution. To understand the magnitudes of the contributions of each cloud type to the longwave term, the constituents of the longwave term are shown in the left-hand panels in Figure 3.9. The figure shows the  $LW'_n \times \widehat{h}'_n$  covariance, and the fraction of each category. The mean  $LW'_n$  and  $\widehat{h}'_n$  are also shown, as well as the non-normalised longwave anomaly. Note that the mean  $LW'_n$  multiplied by the mean  $\widehat{h}'_n$  does not equal the mean  $LW'_n \times \widehat{h}'_n$  covariance, although for most categories they are approximately equal. One notable exception is the  $LW'_n \times \widehat{h}'_n$  covariance for the Clear regions at 305 K, which is negative, despite having both negative  $LW'_n$  and  $\widehat{h}'_n$ . This is discussed in Section 3.4.2.

Despite their relatively low  $LW'_n \times \widehat{h}'_n$  covariance, High clouds are one of the main contributors to the longwave term at all SSTs because of their abundance, occurring roughly four times as often as any other cloud type (Figure 3.9i). The longwave covariances for the High & Mid and Deep clouds are high compared to the other categories, and they are abundant enough to have an impact on the overall longwave term (Figure 3.9a). Low, Mid, and Low & Mid clouds have a small mean longwave covariance and also a small total fraction, making their contribution to the overall longwave term negligible. Despite

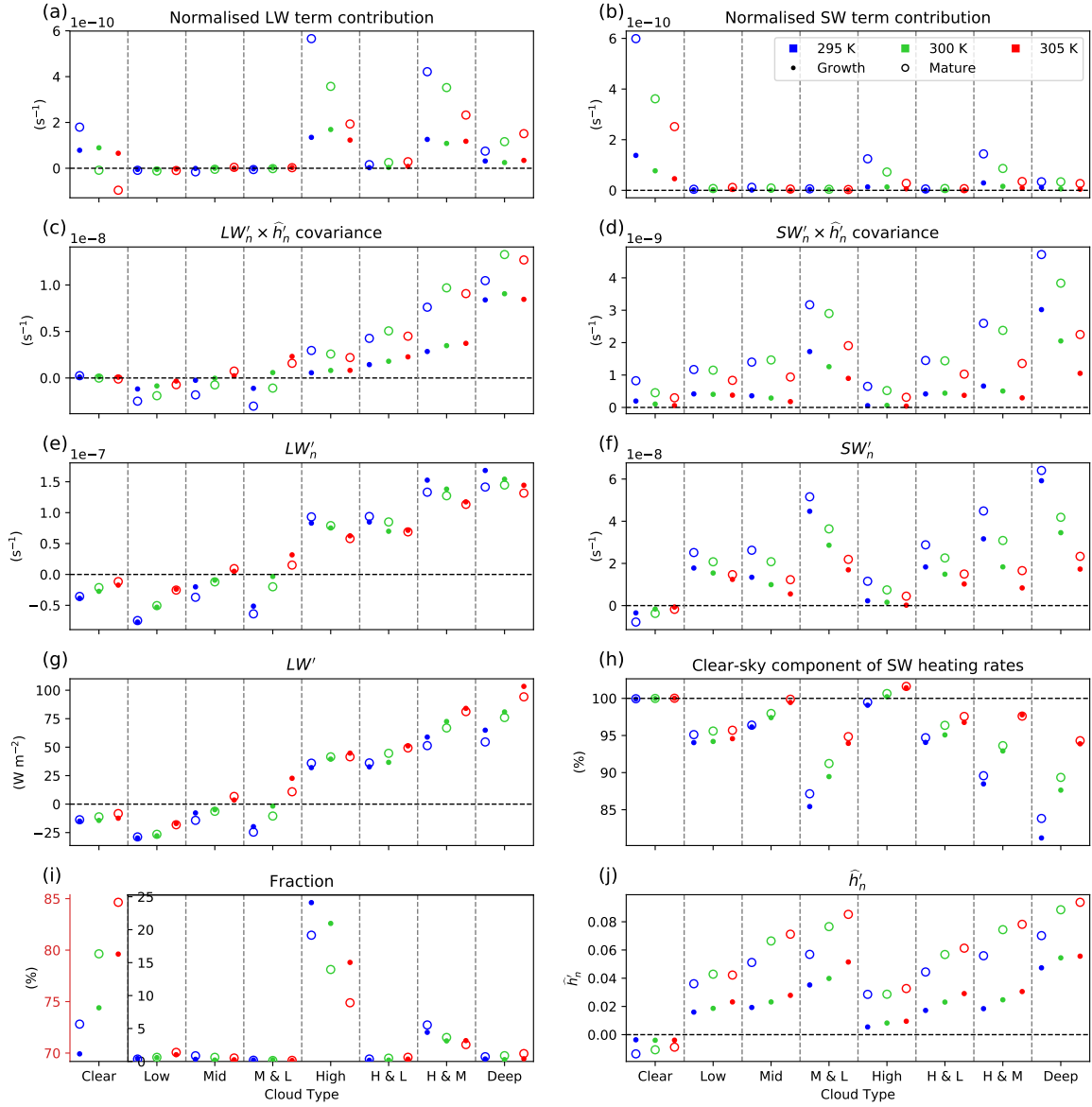


Figure 3.9: Mean (a) contribution to the longwave term in Equation (2.2), (b) contribution to the shortwave term, (c) normalised longwave  $\times$  FMSE covariance, (d) normalised shortwave  $\times$  FMSE covariance, (e) normalised longwave heating anomaly, (f) normalised shortwave heating anomaly, (g) longwave heating anomaly, (h) clear-sky heating divided by total shortwave heating rate, (i) cloud fraction, and (j) normalised FMSE anomaly for the Growth (dots) and Mature phase (open circles) of the *LARGE* domains. Data points for each category are in order of SST increasing to the right. Boxplots showing the spread of the data for the Mature phase are shown in Figure 3.10.

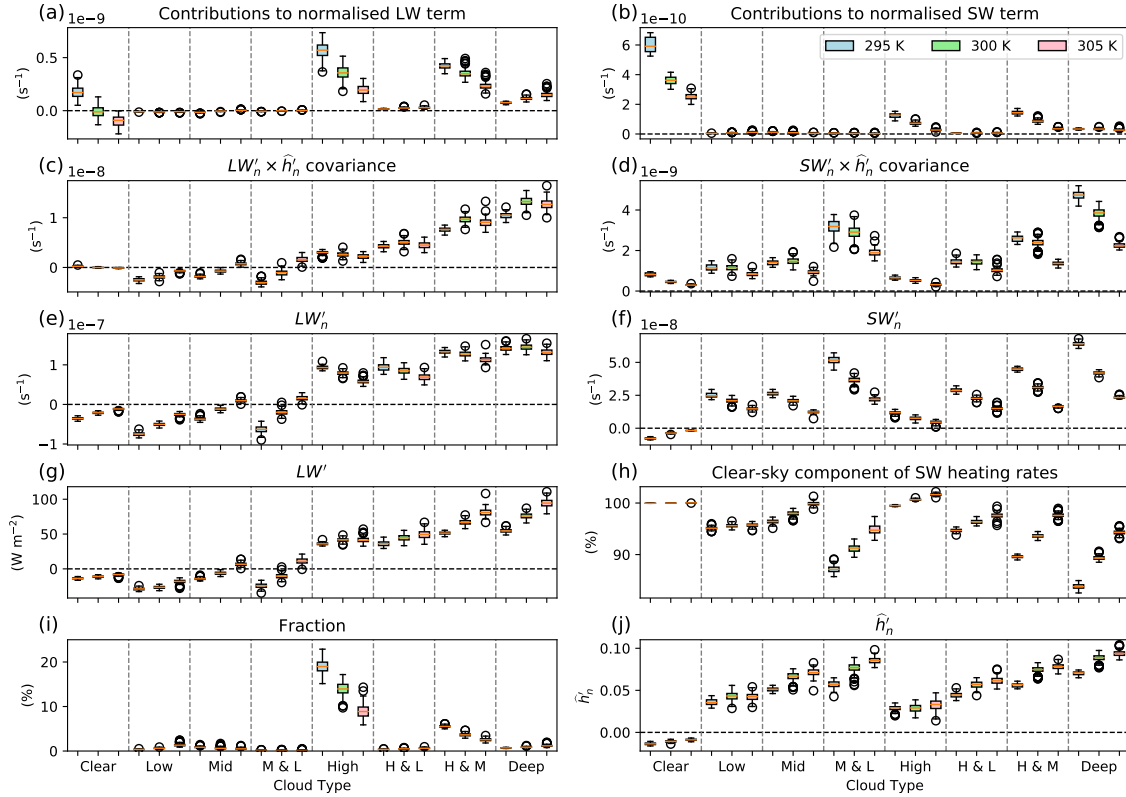


Figure 3.10: (a) Contribution to longwave term in Equation (2.2), (b) contribution to the shortwave term, (c) normalised longwave  $\times$  FMSE covariance, (d) normalised shortwave  $\times$  FMSE covariance, (e) normalised longwave heating anomaly, (f) normalised shortwave heating anomaly, (g) longwave heating anomaly, (h) clear-sky heating divided by total shortwave heating rate, (i) cloud fraction, and (j) normalised FMSE anomaly during the Mature stage of the *LARGE* domains. Clear fractions are 73, 80 and 85% on average in order of increasing SST (not shown). Each data point represents the instantaneous domain-mean of the category. Orange lines indicate the median. Boxes represent the upper ( $Q_3$ ) and lower ( $Q_1$ ) quartiles, with the whiskers showing the range of the data, from the smallest value greater than  $Q_1 - 1.5(Q_3 - Q_1)$  to the largest value less than  $Q_3 + 1.5(Q_3 - Q_1)$ . Outliers above and below the whiskers (circles) are any data point that is outside this range. Boxes for each category are in order of SST increasing to the right.

having the third largest longwave covariance, the High & Low cloud type has one of the smallest cloud fractions, making its overall contribution also very small.

There is a significant decrease in the contributions of High and High & Mid clouds to the longwave term as SST increases (Figure 3.9a). Figure 3.9c shows that the  $LW'_n \times \widehat{h}'_n$  covariance remains similar for these cloud types across all SSTs, yet the fraction of these clouds decreases (Figure 3.9i). This suggests the sensitivity of the High and High & Mid cloud's longwave contribution to aggregation is predominantly due to the sensitivity of their abundance to SST. This decrease in anvil cloud fraction with SST is consistent with the stability iris mechanism described by Bony et al. (2016), who describe the reduction in anvil cloud as a consequence of increased anvil stability and decreased convective outflow with increasing SST. This decrease in high clouds is consistent with  $\sim 70\%$  of the other RCEMIP models (Wing et al., 2020).

The net longwave heating rate for all cloud types is negative, and gets more negative with increasing SST (not shown). This SST sensitivity is primarily because the downwelling longwave radiation into the surface increases with SST faster than the upwelling longwave radiation. However, the non-normalised longwave heating anomalies tend to become more positive with SST. As noted in Section 3.3, Wing and Cronin (2016) hypothesise that the longwave cloud feedback would be more negative at lower SSTs because the clear-sky atmosphere is a weaker emitter of longwave radiation at cooler SSTs, whereas clouds act as effective longwave emitters, making their  $LW'$  more negative. Figure 3.9g is in agreement with this hypothesis, with  $LW'$  for each cloud type being more negative at lower SSTs. Once the longwave anomalies are normalised however, we see there is a slight decrease in  $LW'_n$  with increasing SST for the significant cloud types as the difference between  $\widehat{h}'_{\max}$  and  $\widehat{h}'_{\min}$  increases. The decrease in  $LW'_n$ , along with the slight increase in  $\widehat{h}'_n$  with SST, results in the  $LW'_n \times \widehat{h}'_n$  covariance for the most abundant cloud types remaining approximately constant with SST.

### 3.4.2 Longwave Interactions within the Clear Regions

Figure 3.9a shows the contributions of the Clear regions to the longwave term decrease and become negative with increasing SST. The reason for this is not immediately apparent, with the mean  $LW'_n \times \widehat{h}'_n$  covariance becoming negative, despite both the mean  $LW'_n$  and mean  $\widehat{h}'_n$  remaining negative (which would usually produce a mean positive covariance). This indicates that there must be a significant proportion of the Clear regions with large negative covariance which is able to reduce the overall contribution to the longwave term with increasing SST.

We consider four types of Clear regions at play here whose significance changes with SST. There are the regions with both positive  $\widehat{h}'$  and  $LW'$  (H+L+), regions with both negative  $\widehat{h}'$  and  $LW'$  (H-L-), positive  $\widehat{h}'$  and negative  $LW'$  (H+L-) and finally, negative  $\widehat{h}'$  and positive  $LW'$  (H-L+). Note that this “H” and “L” nomenclature is only used to categorise the Clear regions and is not to be confused with High and Low clouds. The Clear covariance quadrant map in Figure 3.6e shows that H+L+ regions are rare and are found in the highest  $\widehat{h}'$  areas, with a portion of these regions perhaps occurring as an artifact of the condensed water content used to define clouds. A lot of these H+L+ columns may indeed have enough high-altitude condensed water to produce a positive longwave heating anomaly. H+L- regions are typically found surrounding the cloud clusters, with H-L- occupying the majority of the dry regions. H-L+ occur only within the very driest areas. The H+L+ and H-L- regions both have a positive  $LW' \times \widehat{h}'$  covariance whereas the H-L+ and H+L- regions have a negative covariance. By calculating the domain fraction of these regions, as well as their mean  $LW'_n$  and  $\widehat{h}'_n$  and their mean  $LW'_n \times \widehat{h}'_n$  covariance, we can see how their influences on the longwave term changes with SST. These calculations are shown in Figure 3.11 for both the Growth phase and Mature phase of aggregation. The Growth phase is discussed in Section 3.5.

There is a shift in dominance from the positive covariance regions to the negative co-

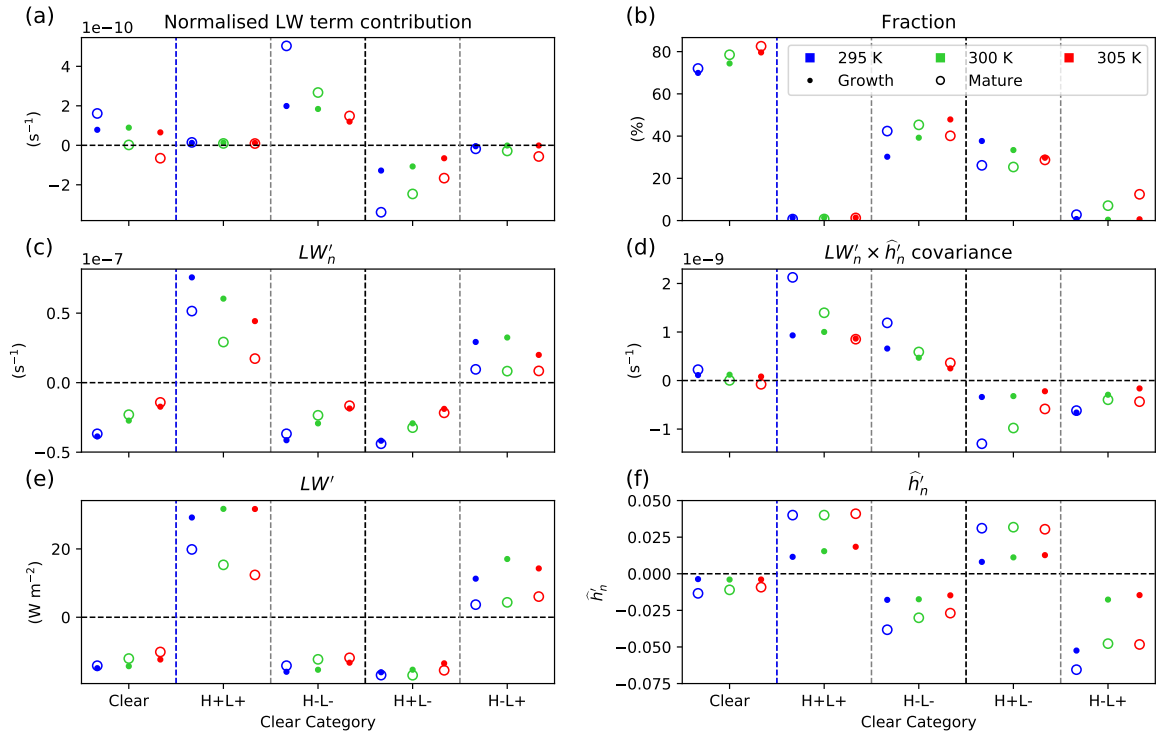


Figure 3.11: Mean (a) contribution to the normalised longwave term, (b) domain fraction, (c) normalised longwave heating anomaly, (d) mean normalised longwave  $\times$  FMSE covariance, (e) longwave heating anomaly, and (f) normalised FMSE anomaly of each Clear category for the Growth (dots) and Mature phase (open circles). Boxplots showing the spread of the data for the Mature phase are shown in Figure 3.12

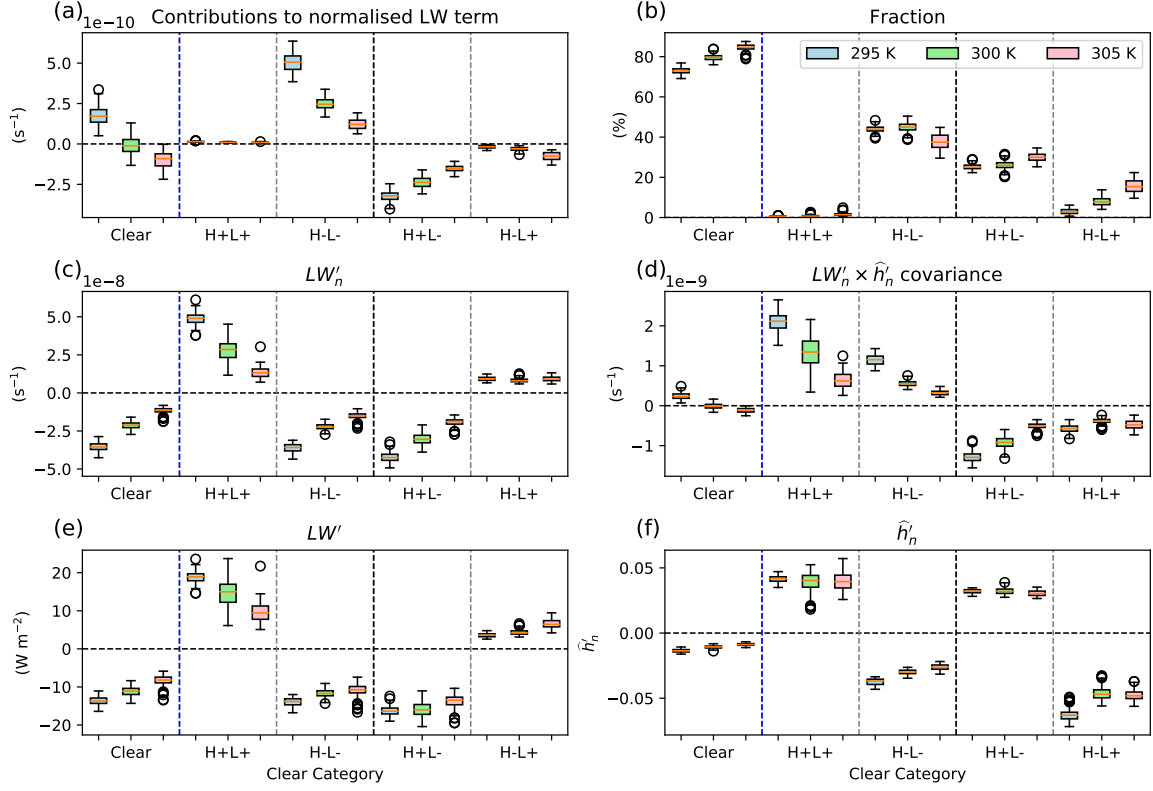


Figure 3.12: (a) Contribution to the normalised longwave term, (b) domain fraction, (c) normalised longwave heating anomaly, (d) mean normalised longwave  $\times$  FMSE covariance, (e) longwave heating anomaly, and (f) normalised FMSE anomaly of each Clear category during the Mature stage of the *LARGE* domains. Each data point represents the instantaneous domain-mean of the category. Boxes and whiskers follow the same format as in Figure 3.10.

variance regions as the SST increases. For all SSTs, the H+L+ regions only occupy around 1% of the domain, making their overall contribution to the longwave term negligible. At 295 K, there are two significant Clear regimes; H-L-, occupying 44% of the domain and H+L-, occupying 25%. They have similar but opposite  $LW'_n \times \widehat{h}'_n$  covariances, so the Clear region's contribution to the longwave term is dominated by the H-L- regions based on their abundance. This results in a positive contribution of the Clear regions to the longwave term.

As SST increases, the  $LW'$  of the Clear regions as a whole becomes significantly less negative (Figure 3.11e). This is mainly due to the approximate halving in the abundance of high-topped clouds, which have strong positive longwave heating anomalies. This then reduces the domain-mean longwave heating rate, making the longwave anomaly of the Clear regions less negative. If we calculate  $LW'$  for each category using the absolute longwave heating rates of the cloud types at 295 K and use the cloud type fractions of the 305 K simulations, we find the  $LW'$  of the clear regions reduce by  $\sim 51\%$ . After normalising the longwave anomalies, the SST sensitivity is even more notable (Figure 3.11e). The contribution of the H-L- regions falls rapidly as the  $LW'_n \times \widehat{h}'_n$  covariance decreases. At the same time, the H-L+ regions (with negative covariance) become far more abundant, also helping to decrease the Clear region's contribution to the longwave term. This feature was also noted by Wing and Emanuel (2014) and Emanuel et al. (2014), who explain that extremely dry columns with little low-level moisture are unable to effectively emit radiation, resulting in anomalous warming.

The magnitude of  $\widehat{h}'$  is largest for the two regimes with positive  $LW'$  (L+, Figure 3.11f). This is because the relationship between  $\widehat{h}$  and longwave heating within the Clear regions is not linear; the strongest longwave cooling occurs roughly where  $\widehat{h}'$  is zero for all SSTs. The effective upward emission level is defined as the altitude at which the temperature is such that  $\sigma T^4$  is equal to the OLR, where  $\sigma$  is the Stefan-Boltzmann constant. Similarly, the effective downward emission level is the altitude at which the

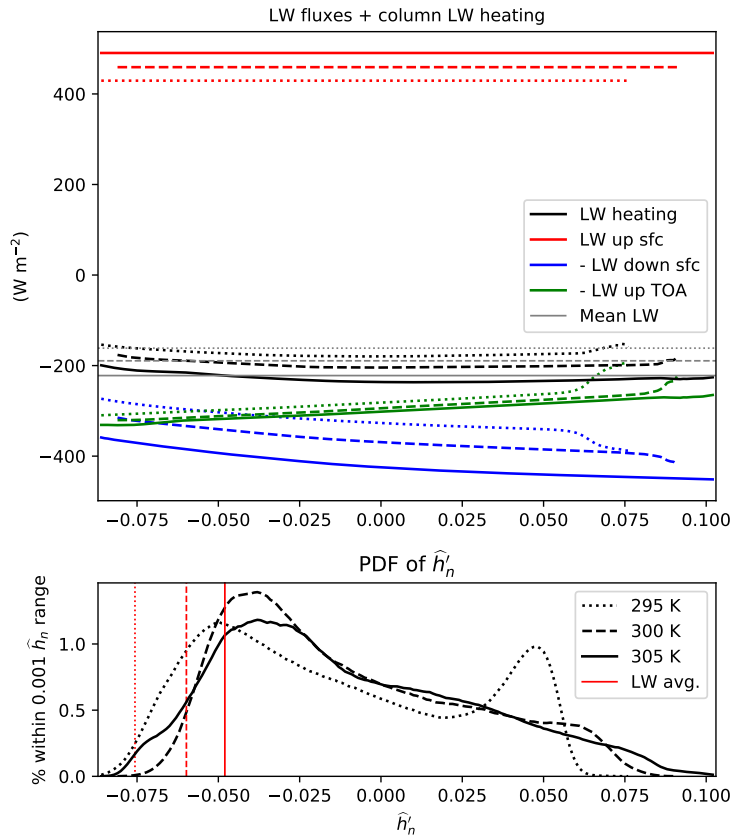


Figure 3.13: (Top) All longwave fluxes into, and out of the atmosphere plotted against  $\hat{h}_n$  anomaly. 295 K: dotted, 300 K dashed, 305 K: solid. The fluxes out of the atmosphere are plotted with positive direction into the atmosphere so that the three fluxes add together to equal the net longwave heating. Horizontal grey lines indicate the domain-mean longwave column heating. (Bottom) Percentage of Clear grid points within a given  $0.001 \hat{h}_n'$  range. The  $\hat{h}_n'$  at which the mean longwave heating anomaly is zero is indicated by the vertical red lines. Clear regions to the left of the red line have a positive longwave anomaly on average.

temperature is such that  $\sigma T^4$  is equal to the downwelling longwave radiation at the surface. For anomalously moist regions, high humidity in the boundary layer makes the effective downwelling level of emission close to the surface. Therefore, an increase in moisture does little to increase the downwelling longwave radiation. In these regions, an increase in moisture has more of an effect in raising the upwelling level of emission to a cooler level, decreasing OLR, reducing longwave cooling. For anomalously dry regions, the infrared atmospheric windows are largely transparent to longwave radiation, so the upwelling level of emission is low (enhanced OLR) and the downwelling level of emission is high (reduced downwelling radiation). In these regions, the free troposphere is very dry, so humidity variations are mainly affected by changes in boundary layer humidity. An increase in humidity in these dry regions has more of an effect in lowering the downwelling level of emission than raising the upwelling level of emission. Therefore, increasing humidity leads to a lowering of the downwelling emission level, increasing downwelling longwave radiation, enhancing longwave cooling. Upwelling and downwelling longwave fluxes are shown as a function of  $\hat{h}'_n$  in Figure 3.13. Specific humidity profiles and effective emission levels as a function of  $\hat{h}'_n$  for each SST are shown in Figure 3.14.

With the mean longwave heating rates skewed more toward the Clear longwave heating rates with increasing SST, there is a greater quantity of Clear regions with positive  $LW'$ . This can be seen in the bottom panel of Figure 3.13, noting the tails of the  $\hat{h}'_n$  distributions extend more into the regions with positive longwave heating anomalies as SST increases. This has the effect of lowering the  $LW'_n \times \hat{h}'_n$  covariance of the H-L- regions, increasing the contribution of H-L+ regions to the longwave feedback term, and making the total Clear regions' contribution to the longwave term negative at high SSTs.

### 3.4.3 Shortwave Interactions

Figure 3.9b shows that shortwave feedbacks in the Clear regions contribute the most to the shortwave term once the domain is aggregated. However, this is an artifact of the

---

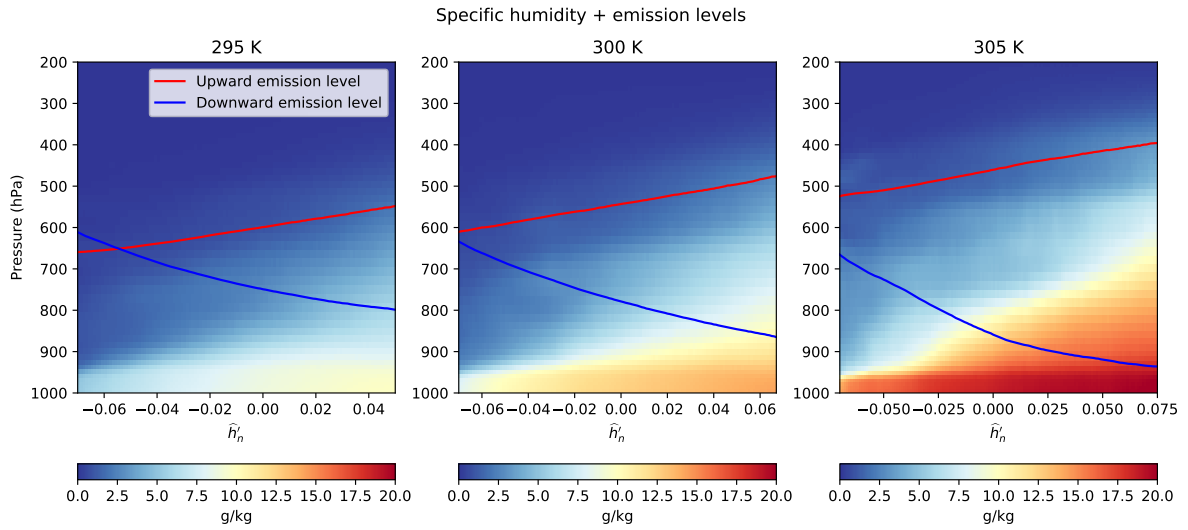


Figure 3.14: Specific humidity profiles against  $\hat{h}'_n$  in the Clear regions for each of the *LARGE* domain simulations the final 20 days at. Effective level of outgoing TOA longwave emission shown in red, effective level of longwave emission into the surface shown in blue.

large fraction of the Clear regions. It can be seen from Figure 3.6b & d that there is a very strong relationship between both FMSE and shortwave anomalies. This is because variations of FMSE are dominated by changes in water vapour, which is an excellent absorber of shortwave radiation. This results in the shortwave-FMSE covariance being positive at almost every location (e.g. Arnold and Putman, 2018).

A large portion of the cloud contribution to the shortwave term is due to the amount of water vapour in the column. The contribution of water vapour to the column shortwave heating rate can be quantified by calculating the clear-sky heating rates and dividing by the total heating rates for each category as shown in Figure 3.9h. The Clear regions have the second lowest  $SW'_n \times \hat{h}'_n$  covariance behind High clouds, yet they contribute the most to the shortwave term due to the abundance of Clear regions. The total shortwave heating rates can almost entirely be explained by the column WVP, particularly at higher temperatures where the quantity of water vapour is higher, making the condensed water content less significant at higher temperatures. The clear-sky component of the total shortwave heating

rate is lowest for clouds with the highest CWP since there is a higher fraction of the heating rate due to condensed water. The clear-sky heating rate is sometimes higher than the all-sky heating rate for the high clouds since the cloud reflects the radiation that would otherwise have been absorbed by the low-level water vapour.

The contribution of the shortwave term to aggregation is highly sensitive to SST, becoming less important as SST increases. This is because the range of  $SW'_n$  decreases with increasing SST, whereas the range of  $\hat{h}_n$  remains similar. This results in the domain-mean normalised shortwave-FMSE covariance, and therefore, the shortwave term, decreasing with SST (analysis not shown). The range of column WVP across the domain increases exponentially with SST, whereas the relationship between column shortwave heating with WVP is logarithmic (Vaquero-Martínez et al., 2018). This results in the range of shortwave heating across the domain being approximately linear. Once the shortwave heating anomalies are normalised (divided by  $\hat{h}_{max} - \hat{h}_{min}$ ),  $SW'_n$  decreases with increasing SST.

### 3.5 Cloud Type Contributions throughout the Aggregation Process

So far, we have only discussed the radiative interactions within the already-aggregated *LARGE* domains. In this section, we look at the key radiative-convective interactions responsible for the development of aggregation in the Growth phase, studying how these interactions depend on SST, and how they are sensitive to aggregation.

Interactions between  $\hat{h}$  and longwave radiation are the main drivers of self-aggregation at early times (Figure 3.5d). The longwave term is insensitive to SST during the Growth phase, whereas an SST sensitivity develops once the aggregation is Mature, with the mean longwave term decreasing with SST. Throughout the aggregation process, the magnitude of each cloud type's contribution to both radiative terms tends to increase. This is because the magnitude of  $\hat{h}'$  increases, and thus the positive radiative feedbacks increase.

During the Growth phase, the contributions of the different cloud types to the longwave term remain similar with SST, with longwave interactions with high-topped clouds and Clear regions driving aggregation. Perhaps coincidentally, SST trends in the domain fractions of these cloud types are balanced by opposite trends in the  $LW'_n \times \widehat{h}'_n$  covariance resulting in their contributions to the longwave term being similar.

The development of the negative SST-dependence of the longwave term during the Mature phase can be largely attributed to the amount the high-topped cloud fraction reduces from the Growth phase to the Mature phase, which is greater in relative terms for higher SSTs. The SST trend of the  $LW'_n \times \widehat{h}'_n$  covariance of High clouds also becomes more negative during the Mature phase. Figure 3.9g shows that the  $LW'$  remains approximately constant with aggregation for all categories, so High clouds' increasingly negative  $LW'_n \times \widehat{h}'_n$  covariance with SST during the Mature phase has to do with how  $\widehat{h}'_n$  for High clouds changes with aggregation. Because of the stability iris mechanism described by (Bony et al., 2016), anvil clouds extend further away from the updrafts at cooler SSTs, allowing anvil clouds to occur in lower FMSE regions. This effect is enhanced with disaggregated convection where the horizontal scale of the moist regions is small. For aggregated convection, the moist regions are much larger in size, so even anvils that extend far beyond the updraft will remain in anomalously moist environments, enhancing the longwave-FMSE feedback. Therefore, the  $\widehat{h}'_n$  of High clouds increases less with aggregation at higher SSTs. This, combined with the decrease in high-topped cloud fraction with SST, decreases the cloud contribution to the longwave feedback during the Mature phase as SST increases.

The longwave feedback in the Clear regions is positive and insensitive to SST during Growth phase. The H-L- and H+L- categories are the only Clear categories that have a significant impact during the Growth phase, with the H-L- having the largest contribution to the longwave term (Figure 3.11a). During the Growth phase, the contribution of the H-L- category remains similar since the increase in its fraction with SST is perhaps coin-

cidentally balanced by the decrease in  $LW'_n \times \widehat{h}'_n$  covariance. As the convection becomes more aggregated, the fraction of the H-L- regions becomes more constant with SST. The  $LW'_n \times \widehat{h}'_n$  covariance also becomes increasingly negative with SST because  $\widehat{h}'_n$  becomes less anomalously negative. These factors result in the longwave feedback of the Clear regions developing the negative SST dependence once the convection aggregates.

Wing and Cronin (2016) find the clear-sky longwave feedback increases with SST particularly during the Growth phase, which is consistent with the simple two-layer model outlined in Emanuel et al. (2014) that suggests the clear-sky longwave feedback becomes more positive with SST. This is because at low SSTs, the tropospheric longwave opacity is low, so an increase in humidity results in an increase in atmospheric longwave cooling (negative feedback). At high SSTs, the tropospheric longwave opacity is higher due to increased water vapour. Here, an increase in humidity results in a decrease in longwave cooling (positive feedback). We find the Clear regions' longwave contribution to the domain-mean longwave feedback is similar with SST during the Growth phase, then decreases with SST during the Mature phase. This effect is not a disagreement with those studies, as this study does not consider the clear-sky radiative fluxes separately. Instead, we only use the total radiative fluxes and we break down the domain-mean longwave feedback into contributions from Clear and cloudy regions. Our study finds the longwave contribution of the Clear regions decreases with SST because their longwave cooling becomes less anomalous with SST due to the reduction of high-topped clouds.

The shortwave interactions become less significant for driving aggregation as SST increases. The clear-sky shortwave contribution is inversely proportional to the difference between  $\widehat{h}_{\max}$  and  $\widehat{h}_{\min}$ , and the difference in shortwave absorption between cloudy and clear regions decreases with SST as the atmosphere contains more water vapour. This results in the shortwave interactions being approximately 2.5 times more important in driving aggregation at 295 K compared to 305 K (Figure 3.9b & 3.5d).

The shortwave anomalies increase in magnitude as aggregation increases, since the

cloudy regions become more humid and the clear regions become drier, amplifying the shortwave heating anomalies. Because of this, the shortwave feedback is more effective in maintaining aggregation than driving it. However, at very early times, particularly for cooler SSTs, the shortwave absorption by clouds can have a significant impact on increasing aggregation. This can be seen in Figure 3.9h, with the clear-sky component contributing more to shortwave heating during the Mature phase, and also in the time series of the clear-sky component of the shortwave term (using clear-sky radiative transfer calculations) shown in Figure 3.15. At very early times, there is little variation in horizontal distribution of water vapour, so the shortwave absorption by clouds has a significant impact on the mean  $SW'_n \times \widehat{h}'_n$  covariance. At these times, the shortwave absorption by clouds accounts for between 30% and 50% of the shortwave term, with clouds having a larger impact at colder SSTs due to the decrease in tropospheric water vapour. This SST dependence is consistent with Wing and Cronin (2016). As soon as dry and moist patches begin to develop, the horizontal variations in the shortwave absorption of water vapour dominate the shortwave term, accounting for 87% - 96% of the shortwave term as SST increases once the domains are aggregated.

### 3.6 Comparison of Convection within High-Resolution Simulations

In the previous sections, only radiative interactions within *LARGE* domain simulations have been analysed. In addition to these, we have also simulated the three-SST RCEMIP cases in three other model configurations on smaller ( $100 \text{ km} \times 100 \text{ km}$ ) domains to investigate how radiative interactions with clouds and moisture may be affected by horizontal grid spacing and the treatment of subgrid condensation. Our *SMALL* and *SMALL\_RHCRIT* simulations have a grid spacing of 1 km, while the *SMALL\_HI* simulations have a grid spacing of 0.1 km. While the *SMALL* and *SMALL\_HI* both have a uniform RHcrit pa-

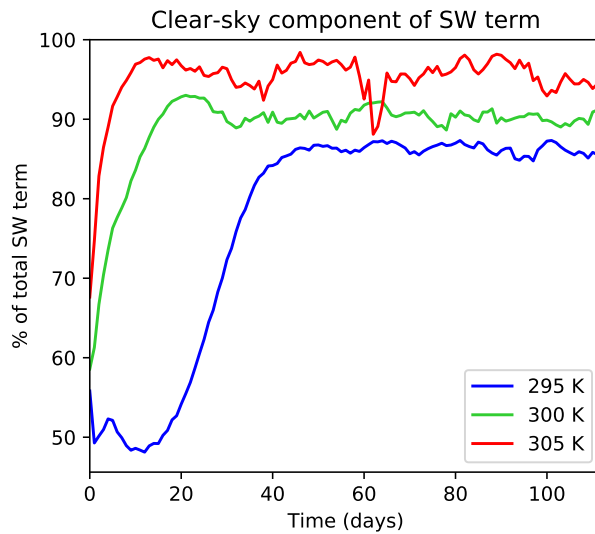


Figure 3.15: Time series of the daily-mean clear-sky component of the shortwave term, calculated as the domain-mean shortwave term using clear-sky heating divided by the domain-mean shortwave term.

parameter of 99%, the *SMALL\_RHCRIT* simulations have  $RH_{crit}$  decreasing from 96% near the surface to 80% at 900 m and above.

With the length scale of the aggregated features in the *LARGE* domain being many times larger than the dimensions of our smaller simulations, we are not able to quantify how these changes in resolution and  $RH_{crit}$  explicitly affect aggregation. However, we are able to see how the radiative properties of the clouds are affected. We can then infer how these changes in the radiative properties of cloud may impact aggregation in larger-scale simulations.

Convection displays some degree of aggregation in all of our simulations except for the *SMALL\_HI* 295 K case. On average, the large domain simulations reach a maximum  $\text{var}(\hat{h}_n)$  of  $2.5 \times 10^{-3}$ , the *SMALL* and *SMALL\_RHCRIT* simulations reach  $1.2 \times 10^{-3}$ , and the *SMALL\_HI* simulations reach an average of  $0.21 \times 10^{-3}$ . Time series of  $\text{var}(\hat{h}_n)$  for each domain and SST are shown in Figure 3.16. To compare radiative interactions with clouds across our domains, disregarding the influence of strong aggregation, we compare times

at which  $\text{var}(\hat{h}_n)$  is less than  $4 \times 10^{-4}$ . We also neglect the first two days of the *LARGE*, *SMALL* and *SMALL-RHCRIT*, and the first five days of the *SMALL-HI* simulations, to ignore the spin-up phase of the simulations

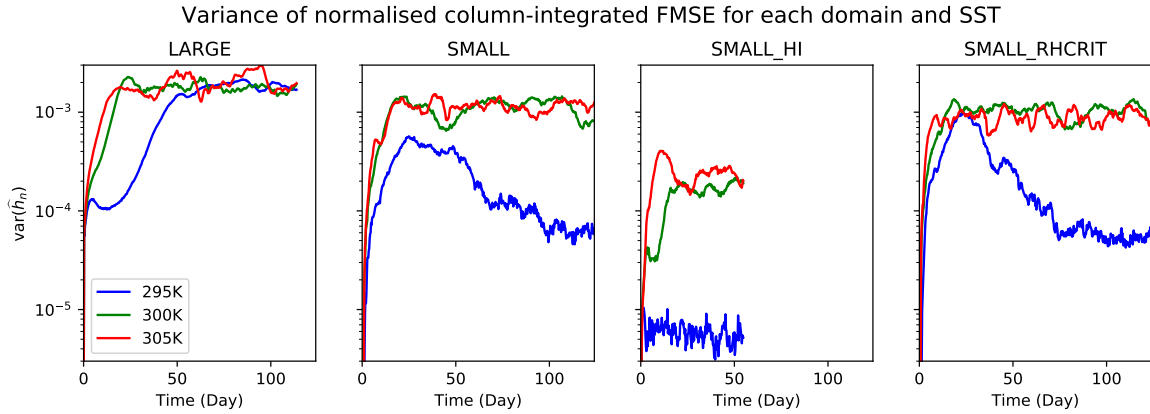


Figure 3.16: Time series of the variance of normalised FMSE for all domains and SSTs.

Profiles of cloud fraction reveal that both grid spacing and RHcrit strongly influence the vertical structure of clouds across the domain (Figure 3.17). This figure shows only the 295 K simulations, although similar changes are seen at the other SSTs. As the grid spacing is reduced, there is a sharp increase in the quantity of low and mid-level cloud, with this increase being most apparent when looking at the *SMALL-HI* simulation. Low-level clouds generally have smaller length scales so cannot be resolved in coarser grid spacings due to the unrealistically high RHcrit value used. Our original RHcrit value becomes more suitable at lower grid spacings, effectively representing these small-scale clouds more realistically. There is also a decrease in altitude of high-level clouds with decreasing grid spacing.

As the RHcrit is decreased to that used in the Met Office UKV model, the overall cloud amount increases. This comes from an increase of more than an order of magnitude in low-level cloud and also a significant increase in mid-level cloud. The upper-level cloud

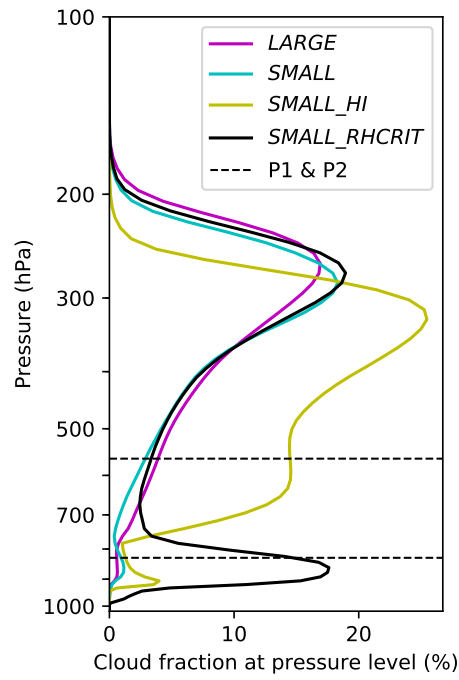


Figure 3.17: Temporally-averaged cloud fraction profiles after the spin-up period and while  $\text{var}(\hat{h}_n) < 4 \times 10^{-4}$  for each domain setup at 295 K. Horizontal dashed lines represent the low and high cloud thresholds (P1 and P2).

amounts remain largely unchanged. Fractions of the High, and High & Mid cloud types are greatly reduced due to the increase in low and mid-level clouds, in turn increasing the quantities of the High & Low and Deep cloud types.

Longwave interactions with FMSE are the main drivers of self-aggregation in our models (Section 3.3, Figure 3.5). With cloud-longwave heating rates remaining largely insensitive to aggregation, a fair comparison of cloud-longwave interactions across our domains can be made. We do not compare the FMSE anomalies of the cloud types as the degrees of aggregation, and hence FMSE anomalies of different cloud types, are very different across the domains, despite neglecting the mature phase of aggregation. We also do not compare the shortwave heating anomalies for the same reason. With shortwave heating rates being mostly dependent on the column water vapour, the changes in shortwave heating rates due to the resolution dependence of cloud structures would be overshadowed by the effects of different degrees of aggregation.

Comparisons of cloud type fraction, normalised longwave heating anomaly, absolute longwave heating, and CWP for each cloud category, SST and domain configuration are shown in Figure 3.18. From this, the resolution dependence of the longwave term for self-aggregation may be inferred. There is a significant decrease in the longwave heating rates, and longwave heating anomalies of high-topped clouds with both decreasing grid spacing and decreasing RHcrit. This is mainly due to an increase in OLR rather than an increase in the downwelling longwave radiation which remains approximately constant for these categories with grid spacing (not shown). This increase in OLR may be mostly explained by the change in cloud top height as well as the decrease of CWP. There is an associated increase in cloud top temperature with decreasing altitude, which increases OLR. One plausible explanation for the reduced cloud top height is that increased updraft mixing at higher resolutions decreases updraft buoyancy and thus reduces the maximum altitude of the plume (this analysis is outside the scope of this thesis). The CWP decreases for the majority of cloud types as the critical condensation humidity is reached more widely,

i.e. by decreasing RHcrit or decreasing the grid spacing. Since water vapour is more readily condensed, the clouds that do form are more widespread and less concentrated. A decreasing CWP of these high-topped clouds decreases their opacity to longwave radiation, decreasing the effective level of emission. This also increases OLR, helping to lower their longwave heating rates.

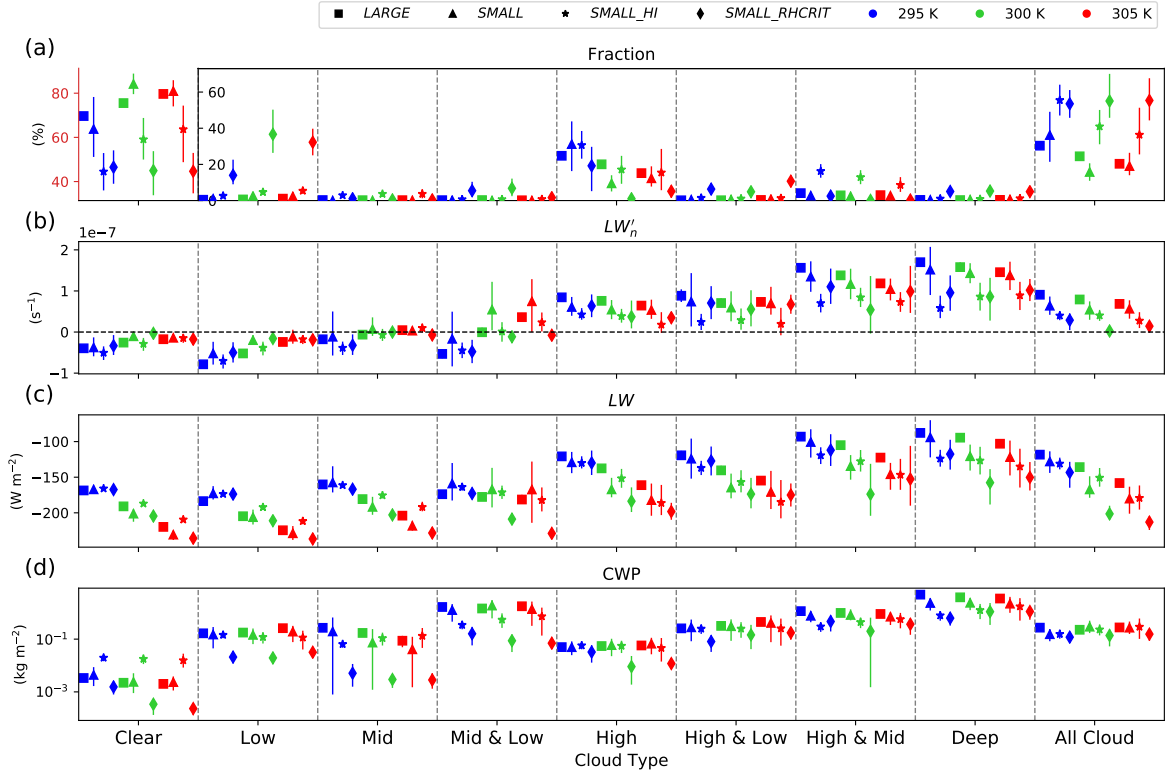


Figure 3.18: Instantaneous domain-means of (a) domain fraction, (b) normalised longwave heating anomaly, (c) absolute longwave heating, and (d) condensed water path, for each cloud category within all domain setups and SSTs. Data taken after the spin-up period and while  $\text{var}(\hat{h}_n) < 4 \times 10^{-4}$  for each domain setup. Note that the fraction of the Clear regions (top-left panel) are on a separate axis to the remaining cloud types. Vertical bars represent the range of the 10th to 90th percentile.

The longwave heating anomalies of the remaining cloud categories without high-level cloud remain similar with grid spacing and RHcrit. As shown in Figure 3.7a, the longwave heating rates of these cloud types are less dependent on CWP in the *LARGE* simulations.

The combined fractions of the lower longwave heating rate categories (the combined sum of the Clear, Low, Mid and Mid & Low categories) remains similar with resolution and RHcrit, and remain far more abundant than the high-topped cloud categories with relatively high longwave heating rate categories. This reduces the spread of longwave heating rates across the domain, decreasing the magnitude of the longwave anomalies for the majority of categories. This may decrease the  $LW'_n \times \widehat{h}'_n$  covariance in moist regions and may significantly reduce the longwave term. An increase in Low and Mid & Low cloud may also significantly reduce the longwave term since they have strong negative heating rates and are mainly found in positive FMSE anomaly regions, so have a negative  $LW'_n \times \widehat{h}'_n$  covariance on average.

Figure 3.17 shows that as grid spacing is reduced, there is a large increase in cloud fraction in the mid-troposphere. This results in the fraction of the High category decreasing, and the High & Mid and Deep category fractions increasing. These categories typically have higher  $LW'_n$  than High clouds. However, the mean  $LW'_n$  of all clouds in the domain is reduced as grid spacing is reduced. With clouds tending to occur in high-FMSE regions, the domain-mean longwave term would likely be reduced. We find a similar result in the reduced RHcrit simulations. With an increase in the low-level cloud, the domain fractions of the High and High & Mid categories decrease, whereas the fraction of Deep clouds increases. Again, Deep clouds tend to have very high  $LW'_n$ , however the mean  $LW'_n$  of all the clouds is again reduced, and is mainly a result of the increased Low cloud fraction with negative  $LW'_n$ .

In our *LARGE* simulations, the contributions of longwave interactions with FMSE to aggregation decrease with SST as anvil cloud fraction reduces. These cloud-radiation trends with SST are largely consistent with those in the simulations with different grid spacing (*SMALL* and *SMALL-HI*). The total high-topped cloud fraction decreases with SST by a similar amount, as does the decrease in  $LW'_n$  for these clouds, meaning trends in the radiative terms to aggregation with SST would likely be similar. For the *SMALL-RHCRIT*

simulations however, with Low cloud approximately doubling from 295 K to 305 K, the magnitude of the longwave term would decrease faster with SST than our original higher-RHcrit simulations. In the *LARGE* simulations, we also find that Clear regions have a significant positive contribution to aggregation at cooler SSTs, with this contribution decreasing with SST and becoming negative. The longwave heating rates of high-topped clouds are more negative in the reduced RHcrit simulations, in turn increasing the domain-mean longwave cooling. This makes the longwave heating anomalies of the Clear regions less negative, which would further lower the Clear contributions to the longwave term. This remains a consistent trend across all of our simulations.

These results can be used to infer how aggregation may be affected in large domains with smaller grid spacings and at the lower RHcrit. Reductions in both grid spacing and RHcrit are associated with a decrease in the anomalous longwave heating of high-topped clouds and an increase in Low cloud fraction. These effects increase the mean radiative cooling of the entire domain, making the clear regions' longwave cooling less anomalous. With reduced anomalous longwave heating in high-FMSE regions and reduced anomalous cooling in low-FMSE regions, the  $LW'_n \times \hat{h}'_n$  covariance would be reduced on average across the domain, slowing the rate of aggregation.

### 3.7 Conclusions

In this chapter, we quantify the dominant direct radiative interactions that drive and maintain aggregation within large channel domain simulations of radiative-convective equilibrium (RCE) of the Met Office Unified Model version 11.0 (submitted to RCEMIP as “UMKOi-vn11.0-RA1-T” (Wing et al., 2018)). We have assessed the sensitivity of these interactions to sea surface temperature (SST) by comparing simulations with fixed SSTs of 295, 300 and 305 K using the normalised vertically-integrated FMSE ( $\hat{h}_n$ ) variance budget as our framework for studying self-aggregation. We define the “Growth” and “Mature”

phases of aggregation using specific ranges of normalised FMSE to ensure a fair comparison of convection across our simulations during these periods. We particularly focus on the role of cloud-radiative interactions, assigning one of eight different cloud types to each grid column based on the heights at which cloud occurs. We also investigate how the key radiative interactions are affected by both grid spacing and the critical condensation relative humidity parameter (RHcrit) using smaller ( $100 \text{ km} \times 100 \text{ km}$ ) domains.

$\hat{h}$  is normalised between an upper and lower limit that are functions of SST, giving values of  $\hat{h}_n$  between 0 and 1. Variations in  $\hat{h}_n$  are dominated by variations in moisture for all of our SSTs. The difference between the upper and lower limits of  $\hat{h}$  is proportional to the magnitude of the FMSE anomalies, making  $\hat{h}_n$  approximately SST-independent.

The instantaneous horizontal variance of normalised vertically-integrated FMSE,  $\text{var}(\hat{h}_n)$ , is a consistent aggregation metric across all SSTs, with values below  $10^{-4}$  corresponding to randomly scattered convection, and values greater than  $10^{-3}$  corresponding to highly aggregated convection. The  $\text{var}(\hat{h}_n)$  budget equation (Equation 2.2) states how the rate of change of  $\text{var}(\hat{h}_n)$ , and hence the rate of change of aggregation, is driven by feedbacks between anomalies in  $\hat{h}_n$  and anomalies in normalised column-integrated longwave heating, shortwave heating, surface fluxes, and advection of  $\hat{h}_n$ . This study focuses on the two radiative feedback terms of this equation (longwave and shortwave), which show that regions with a positive covariance between the normalised radiative anomalies ( $LW'_n$  and  $SW'_n$ ) and  $\hat{h}'_n$  help to increase aggregation.

During the Growth phase of aggregation, the longwave radiative term in Equation (2.2) is the main driver in increasing the horizontal variance of  $\hat{h}_n$ , hence increasing aggregation. The shortwave term is positive, though highly sensitive to SST, contributing 2.5 times more to increasing  $\text{var}(\hat{h}_n)$  at 295 K than 305 K. The surface flux feedback is almost always negative in our simulations and becomes increasingly positive with increasing SST, resulting in the sum of the diabatic terms remaining similar during the Growth phase of aggregation. Despite the sum of the diabatic terms being similar across SSTs, the rate of

aggregation increases with SST. This is because the (usually negative) advection feedback becomes increasingly positive with SST during early stages of aggregation. This allows anomalies in  $\widehat{h}_n$  to amplify more readily at higher SSTs.

During the Mature stage, both radiative terms are key maintainers of aggregation, with the shortwave term being approximately three quarters the magnitude of the longwave term. The longwave term's contribution to the maintenance of  $\text{var}(\widehat{h}_n)$  decreases with SST during the maintenance phase, as does the shortwave term's contribution. The decrease in these terms is then balanced by an increase in the (negative) surface flux and advection terms.

High-topped clouds produce the largest positive column-integrated longwave heating anomalies, whereas low-level clouds produce negative anomalies. The mean  $\widehat{h}'_n$  for each cloud type is positive, therefore clouds with a positive radiative anomaly have a positive radiative-FMSE feedback and vice versa. Longwave interactions with high-topped clouds are the main drivers of self-aggregation because they have a high  $LW'_n \times \widehat{h}'_n$  covariance and they are the most abundant types of cloud. The contributions from these cloud types remain similar with SST during the Growth phase, however their contributions to the maintenance of aggregation decreases with SST as cloud fraction decreases.

Longwave interactions within the clear regions can have a large impact on the total longwave term, although their contributions to the longwave term are highly sensitive to SST and aggregation. The longwave contribution of the clear regions is large and positive during early stages of aggregation and decreases with aggregation and SST, becoming strongly negative during the fully aggregated stage of the high-SST simulation. We show that once the convection is aggregated, the typically negative longwave heating anomalies in the clear regions become less negative with SST as a result of the domain-mean longwave heating becoming increasingly negative. This is due to the reduction of high-topped clouds which have a strong anomalous longwave heating effect, increasing the domain-mean radiative cooling, resulting in the mean longwave heating anomaly of

the clear regions becoming roughly 50% less negative. The mean covariance between the longwave heating and FMSE anomalies becomes negative, meaning the clear regions have a negative contribution to aggregation at high SSTs.

The domain-mean shortwave term is similar in magnitude to the longwave term during the Mature phase because the  $SW'_n \times \widehat{h}'_n$  covariance is positive at almost all times and locations. The mean shortwave-FMSE feedback is heavily dependent on the horizontal spread of water vapour and therefore the state of aggregation, being less important in driving aggregation than maintaining it. The contribution of clouds to the shortwave term also depends on the level of aggregation. At very early times, the additional shortwave absorption of condensed water results in clouds contributing to around 50% of the shortwave term at 295 K and 30% at 305 K SST. As soon as distinct moist and dry patches begin to develop, the differential absorption of shortwave radiation by water vapour rapidly increases the clear-sky component of the shortwave term to 87%-96% of the total shortwave term (from 295 K - 305 K).

Model grid spacing affects the radiative properties of clouds in a number of ways. We find that decreasing grid spacing reduces the mean CWP of clouds, decreases the cloud top height of high clouds, and produces more low and mid-level cloud. The overall effect of these changes to the cloud properties is a reduced mean longwave heating anomaly of high-FMSE cloudy regions. This would decrease the domain-mean covariance between longwave heating and FMSE anomalies, slowing the rate of aggregation for hypothetical high-resolution large-domain simulations. Sensitivities with SST that we find in the large domain remain similar with grid spacing, meaning the magnitude of the decrease in the longwave term with SST would likely remain similar with reduced grid spacing in larger simulations.

The RHcrit parameter used in our simulations is unrealistically high for the grid spacings used, resulting in unrealistic cloud distributions. When lowering the RHcrit to that used in the Met Office UKV model, we find significant changes in the distribution, struc-

ture, and radiative properties of cloud. The combined effects of using the decreased RHcrit would likely reduce the direct longwave contributions to aggregation. Firstly, the CWP of high clouds reduces as RHcrit is decreased although their domain-fraction remains similar. The reduced CWP decreases their longwave heating anomalies and would significantly reduce their contribution to the longwave term. Secondly, there is a large increase in the fraction of low cloud, which would likely further reduce the longwave term due to low cloud's typically negative  $LW'_n \times \widehat{h}'_n$  covariance. However, with the increase in low cloud, the radiatively-driven low-cloud circulations described by Muller and Bony (2015) could become more common, increasing the upgradient transport of FMSE. It is not clear whether this indirect low cloud effect would overcompensate, increasing the rate of aggregation.

The vertical distribution of clouds in our models make these simulations outliers compared to other models submitted to RCEMIP (Wing et al., 2020). Our large-channel simulations have the lowest low-level cloud fraction and one of the highest high-cloud fractions out of the other submitted cloud-resolving models. With high-topped clouds generally having strongly positive  $LW'_n \times \widehat{h}'_n$  covariances, and low clouds having negative covariances, the domain-mean longwave-FMSE feedbacks may be unusually high. Previous literature has highlighted the importance of upgradient FMSE transport by shallow overturning circulations associated with low clouds (Muller and Held, 2012; Muller and Bony, 2015). These circulations could be less prevalent in our simulations compared to other RCEMIP simulations, and may result in the advection feedback in our simulations being lower than simulations with a more realistic vertical cloud distribution.

There is much variability in the degrees of aggregation between numerical models of RCE, which has important consequences for our understanding of weather and climate (Wing et al., 2020). With radiative interactions between cloud and moisture being the dominant drivers and maintainers of aggregation in our models, understanding how these interactions vary between other RCE models may go some way in explaining the differences

in self-aggregation. This is a focus of Chapter 4. By building on the analysis technique of Wing and Emanuel (2014), our normalised FMSE variance budget framework allows for the comparison of cloud-radiative interactions and their contributions to self-aggregation across a range of models and SSTs. This technique is suitable for all models with a fixed SST. Its use for model/reanalysis studies with a varying SST would require the normalisation of  $\hat{h}$  to vary in space and time.

In Chapter 4, we use the  $\text{var}(\hat{h}_n)$  budget framework to study aggregation and cloud-radiation interactions within the CRMs and GCMs in RCEMIP. We compare the results from these models to the results from the UK Met Office UM found in this chapter to test whether our results are robust across these RCEMIP models to achieve the second thesis objective described in Section 1.2. In addition, we assess how the magnitude of cloud-radiation interactions affects the rate of aggregation within these models to achieve our third thesis objective.

## CHAPTER 4

# RADIATION, CLOUDS, AND SELF-AGGREGATION IN RCEMIP SIMULATIONS

### Opening remarks

The work in this chapter has been published as Pope et al. (2023) and is largely unchanged from the paper, except some of the Introduction and Methods from the paper have been moved to Chapters 1 & 2. This chapter makes frequent references to the results of Chapter 3, which is also a published article (Pope et al., 2021). Because of the frequency of references to this article, we choose to abbreviate the citation to “P21”.

### 4.1 Introduction

Convective self-aggregation was first identified in numerical models of radiative-convective equilibrium (RCE) (Held et al., 1993), but the processes influencing it are relevant to real world convection (Holloway et al., 2017) and it has major implications for weather and climate (e.g. Wing et al., 2017). Because of this, it has been the focus of many studies in recent years and continues to be an active area of research. However, there remains

much debate as to the mechanisms and feedbacks responsible for controlling aggregation, which is in part due to the inter-model variability in the structures and dynamics of convection within these models (Wing et al., 2017). Aggregated convection is associated with increased longwave cooling, so the response of aggregation to warming has important consequences for climate sensitivity. The wide variety in responses of aggregation to warming within numerical models leads to a major source of uncertainty in climate sensitivity estimates (Sherwood et al., 2020).

Despite there being debate as to the processes driving and maintaining aggregation, the majority of studies find that interactions between convection, clouds, and longwave radiation are key drivers and maintainers of aggregation (Wing et al., 2017). Most research on cloud feedbacks relies on either general circulation models (GCMs) that use parameterised convection, or limited-area cloud-system resolving models (CRMs) with explicit convection that are too small to represent global-scale circulations. The climate feedback and SST sensitivity of aggregation are different for GCMs and CRMs in the Radiative-Convective Equilibrium Model Intercomparison Project (RCEMIP; Wing et al., 2018, 2020), with GCMs typically having a lower climate sensitivity due to convection becoming more aggregated on average at higher SSTs Becker and Wing (2020). This response is not seen on average in CRMs.

P21 quantified the contribution of direct radiative interactions with different cloud types to longwave and shortwave feedbacks with FMSE using a set of simulations from the UK Met Office Unified Model which are submitted to RCEMIP as UKMOi-vn11.0-RA1-T (referred as UKMO-RA1-T hereafter). They used a similar FMSE variance budget framework to Wing and Emanuel (2014) but normalise  $\hat{h}$  in such a way so that its SST dependence is eliminated, thus making the analysis framework insensitive to SST. They found the direct longwave interactions with high-topped cloud and clear regions to be the main drivers of self-aggregation. High-topped clouds typically occur in anomalously-high  $\hat{h}$  regions and drastically decrease atmospheric radiative cooling, leading to a positive

longwave-FMSE feedback. Similarly, clear regions have anomalously high radiative cooling rates and tend to be found in anomalously-low  $\hat{h}$  regions, again leading to a positive longwave-FMSE feedback and driving aggregation.

P21 found the main maintainers of aggregation were longwave interactions with high-topped cloud, and shortwave interactions with water vapour. The shortwave-water vapour feedback contributes 87-96% of the total shortwave feedback during the mature phase of aggregation, with cloud-shortwave interactions being less important at higher SSTs and higher degrees of aggregation. Anomalously humid environments occur in positive  $\hat{h}'$  regions and are able to absorb more solar radiation leading to a positive feedback. The difference in humidity between the moist and dry regions increases with aggregation, hence the shortwave-moisture feedback has a higher impact during mature aggregation. The extents of the contributions of these feedbacks to aggregation are sensitive to SST. In their simulations, the longwave contribution to aggregation is insensitive to SST during the growth phase of aggregation, but there is a smaller longwave contribution to aggregation maintenance as SST increases due to the reduction of high-topped cloud fraction. This decrease in high-topped cloud fraction is consistent with the stability iris mechanism described by Bony et al. (2016), who describe the reduction in anvil cloud as a consequence of increased anvil stability and decreased convective outflow with increasing SST. Shortwave interactions with moisture become less important to aggregation maintenance at warmer SSTs. This is because the variability in atmospheric solar heating between humid and dry regions contributes to a smaller fraction of the total  $\hat{h}$  variability as SST increases. Despite radiative interactions with cloud and moisture being the main drivers of self-aggregation, the rate of aggregation was most strongly moderated by circulations that generally oppose aggregation, but become less negative at warmer SSTs, resulting in faster aggregation at warmer SSTs.

Wing et al. (2020) showed that the UKMO-RA1-T model is an outlier compared to the other RCEMIP models in several ways. With the upper troposphere being almost fully

saturated, it has one of the largest high cloud fractions and one of the smallest low cloud fractions compared to the other models. In addition, out of all the small  $100 \text{ km} \times 100 \text{ km}$  domain simulations, the UKMO-RA1-T simulations are the only ones that display aggregation. This highlights that the conclusions from P21 are only strictly applicable to the simulations they studied and may not, in some cases, be relevant for other simulations and real-world convection.

In this chapter, we test the robustness of the conclusions from P21 by applying their analysis framework to the CRM and GCM simulations in RCEMIP. We quantify the contributions of cloud-radiation interactions to self-aggregation at different stages of organisation and study their SST dependence. We investigate whether the differences in cloud-radiation interactions between models and model types can explain the differences in the behaviour of self-aggregation. In doing this, we achieve our second and third research objectives that are outlined in Section 1.2.

## 4.2 Methods

### 4.2.1 Normalised FMSE Framework for the CRMs and GCMs in RCEMIP

We analyse the RCEMIP CRMs and GCMs (briefly described in Section 2.1) using the  $\text{var}(\hat{h}_n)$  budget framework to study aggregation (described in Section 2.3). However, to make the comparison between CRMs and the  $40\times$  coarser GCMs as fair as possible, we horizontally smooth the raw output fields of the CRMs so that every grid box is the mean of the  $40 \times 40$  grid boxes surrounding it (accounting for the periodic boundary conditions). This is because  $\text{var}(\hat{h}_n)$  is not only dependent on spatial aggregation, but it is also sensitive to grid spacing, particularly while convection is randomly scattered (analysis not shown). This is due to small-scale features, e.g. convective updrafts and downdrafts that tend to have strong positive and negative  $\hat{h}'_n$  respectively, not being resolved at coarser resolutions. This leads to a smaller  $\text{var}(\hat{h}_n)$  for coarser horizontal

resolutions. As the size of the convective clusters increase and  $\widehat{h}_n$  anomalies are strong over large areas,  $\text{var}(\widehat{h}_n)$  becomes relatively less sensitive to grid spacing. For example, when the CRMs have a  $\text{var}(\widehat{h}_n)$  of  $1 \times 10^{-4}$ , the average  $\text{var}(\widehat{h}_n)$  after smoothing is around 60% lower. When  $\text{var}(\widehat{h}_n)$  is  $1 \times 10^{-3}$  for CRMs, the  $\text{var}(\widehat{h}_n)$  after smoothing is around 25% lower. When using this smoothing technique in the analysis, we refer to the CRMs as Smoothed CRMs. Assuming that GCMs represent their subgrid scale processes in a similar way to how CRMs resolve them, we would expect similar results between GCMs and Smoothed CRMs.

In a similar way to P21, we define Growth and Mature phases of aggregation by two ranges of  $\text{var}(\widehat{h}_n)$  for which convection is randomly scattered or strongly clustered, respectively. The  $\text{var}(\widehat{h}_n)$  ranges used in this study vary slightly from P21. This is so that as many simulations as possible have a defined Growth and Mature period which satisfy the aforementioned criteria, while the  $\text{var}(\widehat{h}_n)$  ranges remain small. Note that not all models reach the Mature phase because these models do not appear strongly clustered at any point in time. The Growth phase is identified as any time after day 2 (to neglect spin-up effects) when  $\text{var}(\widehat{h}_n)$  for GCMs and Smoothed CRMs is between  $0.8 \times 10^{-4}$  and  $2.4 \times 10^{-4}$ . The Mature phase is identified as any time when  $\text{var}(\widehat{h}_n)$  for GCMs and Smoothed CRMs is between  $0.8 \times 10^{-3}$  and  $2.4 \times 10^{-3}$ . Further justification of these ranges is given in Section 4.3.1. Given our previous notion that  $\text{var}(\widehat{h}_n)$  is sensitive to grid spacing, we use the times of the Growth and Mature phases identified from the Smoothed CRMs to also analyse the (non-Smoothed) CRMs.

Since  $\widehat{h}'_n$  is a factor of every term in Equation (2.2), one might expect the magnitude of the terms to increase with aggregation. By dividing each term by the instantaneous horizontal standard deviation of  $\widehat{h}_n$ , we can eliminate the dependence of the terms on the magnitude of  $\widehat{h}'_n$ . After dividing by this standard deviation, the sensitivity of the terms to aggregation will depend on the sensitivity of the other variable in the term and its correlation with  $\widehat{h}'_n$ .

### 4.2.2 Cloud Classification Scheme

We use a cloud classification scheme to define a cloud type at each grid point in the simulations. The contribution of radiative interactions with these cloud types to aggregation are calculated by multiplying each cloud type’s fraction by the mean covariance between its radiative and FMSE anomalies. This analysis technique is based on that used by P21, however the cloud type definitions in this study are different. In RCEMIP, 3D data are only available for the final 25 days of CRMs and GCMs, so we are not able to define cloud based on the vertical profile of condensed water for the full simulation as in P21. Instead, we define clouds using top of atmosphere (TOA) fluxes, using the same method as Becker and Wing (2020) (referenced as BW20 hereafter). This method produces four different cloud types: Clear, Shallow, Deep, and Other. The outgoing shortwave radiation (OSR) and outgoing longwave radiation (OLR) thresholds used to define the four cloud types are shown in Table 4.1. The Shallow cloud OLR threshold is consistent with the low-cloud threshold used by Fiedler et al. (2020), and the Deep OLR threshold is the same as the RCEMIP threshold to define deep convective cloud. Note that the thresholds in Table 4.1 are used for each SST and are valid for simulations with the fixed insolation and surface albedo used in all RCEMIP simulations (Section 2.1). Also note the convention of capitalising these cloud categories. The Clear category is not to be confused with clear-sky radiation - the radiative fluxes calculated by excluding any cloud from a particular scene.

Table 4.1: OSR and OLR thresholds used to define the cloud types.

Cloud type	OSR ( $\text{W m}^{-2}$ )	OLR ( $\text{W m}^{-2}$ )
Clear	$< 100$	N/A*
Shallow	$\geq 100$	$> 250$
Other	$\geq 100$	173 - 250
Deep	$\geq 100$	$< 173$

\* As long as  $\text{OSR} < 100 \text{ W m}^{-2}$ , the column is classified as Clear, regardless of OLR.

A comparison of the cloud type classification schemes between that used in P21 and this study is shown in Figure 4.1(a-d). These figures show the P21 cloud distributions for each of the BW20 cloud types across all of the CRMs. This comparison uses data from the final 25 days of the simulations; the period for which 3D data is available. Approximately 80% of this study's Clear category is made up of the Clear type defined in P21, meaning the condensed water content is less than  $10^{-6}$  kg m<sup>-3</sup> everywhere in the column. The remainder of the BW20 Clear category is mostly made up of optically-thin High and Low cloud. The Shallow cloud type is mostly made up of Low cloud, and the Deep cloud is almost entirely made up of the high-topped cloud (High, High & Mid, High & Low, and Deep). The Other cloud type is made up of approximately two thirds high-topped cloud that is perhaps too optically thin or having too small a vertical extent to lead to an OLR less than  $173$  W m<sup>-2</sup> and be classed as Deep.

Cloud types are redefined using the Smoothed radiative fluxes in order to make a fairer comparison to GCMs. The distribution of the P21 cloud types for each Smoothed cloud type is shown in Figure 4.1(e-h). Again, this comparison uses data for the final 25 days of the simulations. The Smoothed Clear and Deep categories are mainly made up of the P21 Clear and high-topped cloud categories respectively. There is little difference between the Smoothed and non-Smoothed distributions for these cloud types. The Smoothed Shallow cloud is mostly made up of Clear and low to mid-topped cloud. The Smoothed Other cloud type is mostly composed of high-topped cloud. The main difference between the non-Smoothed and Smoothed distributions is the increase in fraction of Smoothed Other cloud and the decrease in fraction of the Smoothed Deep cloud.

Figure 4.2 shows the fraction of different cloud types as a function of FMSE percentile during the final 24 hours of the simulations. Differences in the BW20 and P21 cloud classification schemes within the CRMs can be seen by comparing Figures 4.2a and 4.2c. Cloud fraction increases with FMSE percentile regardless of the cloud classification scheme used. There is a lower cloud fraction in the BW20 cloud types compared to the P21 cloud

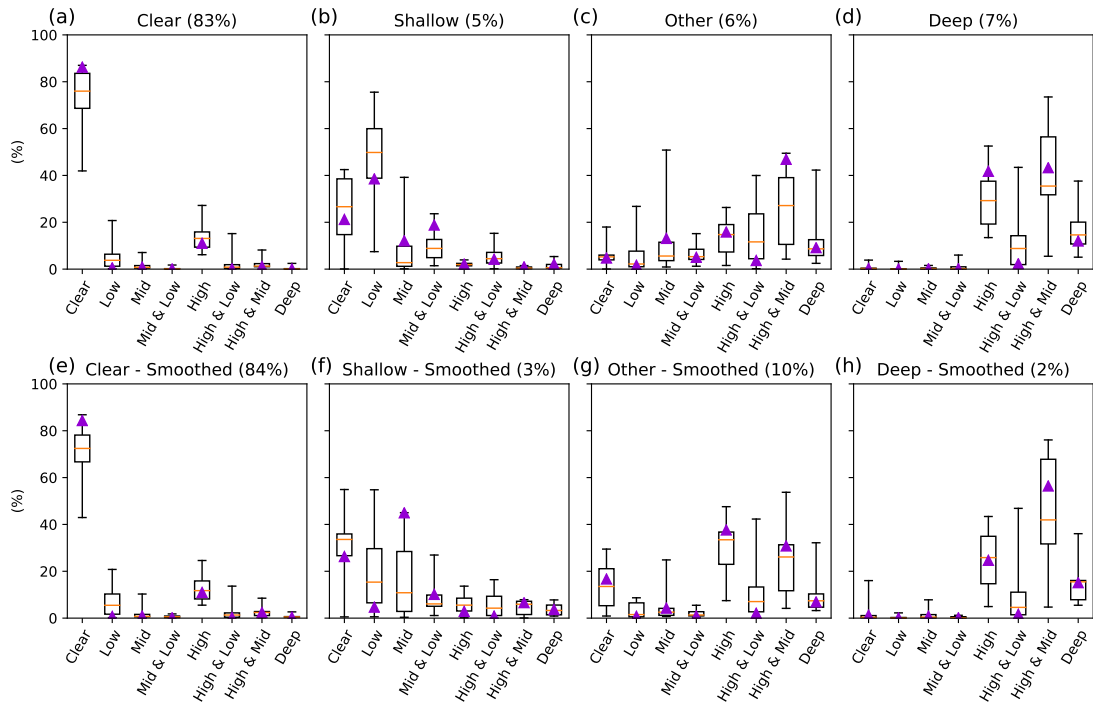


Figure 4.1: (a-d) Distributions of the cloud categories used in P21 for each of the four cloud types used in this study. (e-h) Distributions of the cloud categories used in P21 for each of the Smoothed cloud types. Data is averaged over the final 25 days of the CRMs for all SSTs. Orange lines represent the median, boxes represent the interquartile range, and whiskers represent the full range of the models. The UKMO-RA1-T model is shown in purple triangles. Average domain fraction is shown in the subplot titles.

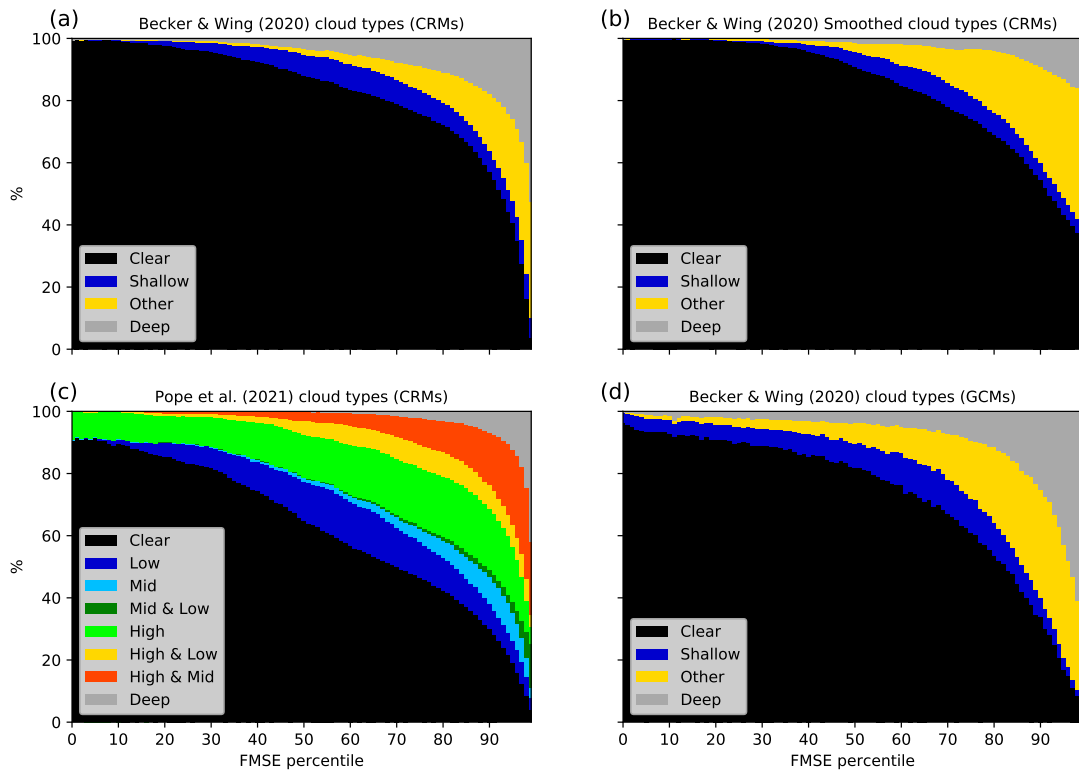


Figure 4.2: Cloud type fraction vs FMSE percentile for the (a) BW20 cloud types for all CRMs, (b) Smoothed BW20 cloud types for all CRMs, (c) P21 cloud types for all CRMs, and (d) BW20 cloud types for the GCMs during the final 24 hours of the simulations.

types at all FMSE percentiles except for the extremely moist environments in which the cloud fraction is close to 100%. There is more high-topped cloud in the P21 classification scheme compared to the BW20 Deep cloud which may be due to the presence of optically-thin High cloud that has  $OSR < 100 \text{ W m}^{-2}$ . There is also a greater fraction of P21 Low cloud compared to BW20 Shallow cloud at all FMSE percentiles, again due to the presence of optically thin Low cloud with  $OSR < 100 \text{ W m}^{-2}$ .

The effect of Smoothing is shown by comparing Figures 4.2a with 4.2b. Smoothing reduces the total cloud fraction in the lower 40% and upper 10% of FMSE values. The fraction of Deep cloud is reduced and the fraction of Other cloud is increased at all FMSE percentiles. The difference between Smoothed CRMs and GCMs can be seen by comparing Figures 4.2b and 4.2d. There is a greater cloud fraction in GCMs at all FMSE percentiles, which is largely due to the increase in Deep cloud fraction. There is also a greater Shallow cloud fraction particularly at lower FMSE values, and a lower Other cloud fraction at higher FMSE values. The effects of Smoothing, and comparisons between CRMs and GCMs are discussed further in Section 4.4. The cloud type fractions of the non-Smoothed CRMs are most similar to the fractions of the GCMs, suggesting GCMs may be tuned to have a more accurate cloud fraction in a discrete grid box sense rather than on subgrid scales. Yet GCMs still have a greater average cloud fraction particularly at higher  $\widehat{h}'_n$  regions.

Radiative interactions with high-topped cloud and Clear regions are shown to have the largest role in aggregation in P21. With the majority of BW20 Clear and Deep clouds being collocated with P21 Clear and high-topped cloud respectively, results from P21 can be fairly compared to results from this study.

## 4.3 Variance of Normalised FMSE

### 4.3.1 Evolution of Normalised FMSE variance in RCEMIP simulations

The RCEMIP CRMs simulate a wide range of convective characteristics (Wing et al., 2020). All models analysed in this chapter display aggregation to some degree except for the UKMO-CASIM model at 305 K, whose convection remains scattered throughout the entire simulation. Figure 4.3 shows 24-hour running averages of  $\text{var}(\hat{h}_n)$  for each Smoothed CRM and SST. Also shown are the  $\text{var}(\hat{h}_n)$  limits for the Growth and Mature phase of aggregation (introduced in Section 4.2) which will be discussed in Sections 4.3.2 and 4.4. There is much variability in the rate of aggregation amongst the CRMs as well as the maximum degree of aggregation, with no consistent SST dependence. The inconsistent SST dependence of aggregation is seen regardless of aggregation metric used Wing et al. (2020).

In the majority of CRMs, aggregation begins as dry patches form and expand in size. These dry regions get drier while moist regions get moister. The dry patches in these models continue to grow until the convection is constrained to 3-8 quasi-stationary bands orientated along the short axis of the domain. In CM1, SCALE, and WRF-COL-CRM (and DAM to a lesser extent), waves continuously propagate across the domain, taking approximately 3 days to traverse the long axis. These models typically exhibit rapid fluctuations in  $\text{var}(\hat{h}_n)$  (Figure 4.3). Intense convection is generated within these waves, and horizontal humidity variations are smoothed out behind the waves. These waves inhibit aggregation, so these simulations often do not reach the Mature phase. UKMO-CASIM is unique in the way moist regions seem to amplify first in the 295 K and 300 K simulations, generating convergence within the moist regions. Dry patches then begin to develop in the divergent regions but they struggle to amplify, often becoming remoistened particularly at warmer SSTs. At 305 K, both the moist and the dry regions in UKMO-CASIM fail to amplify. Not all models reach both the Growth and Mature stages of

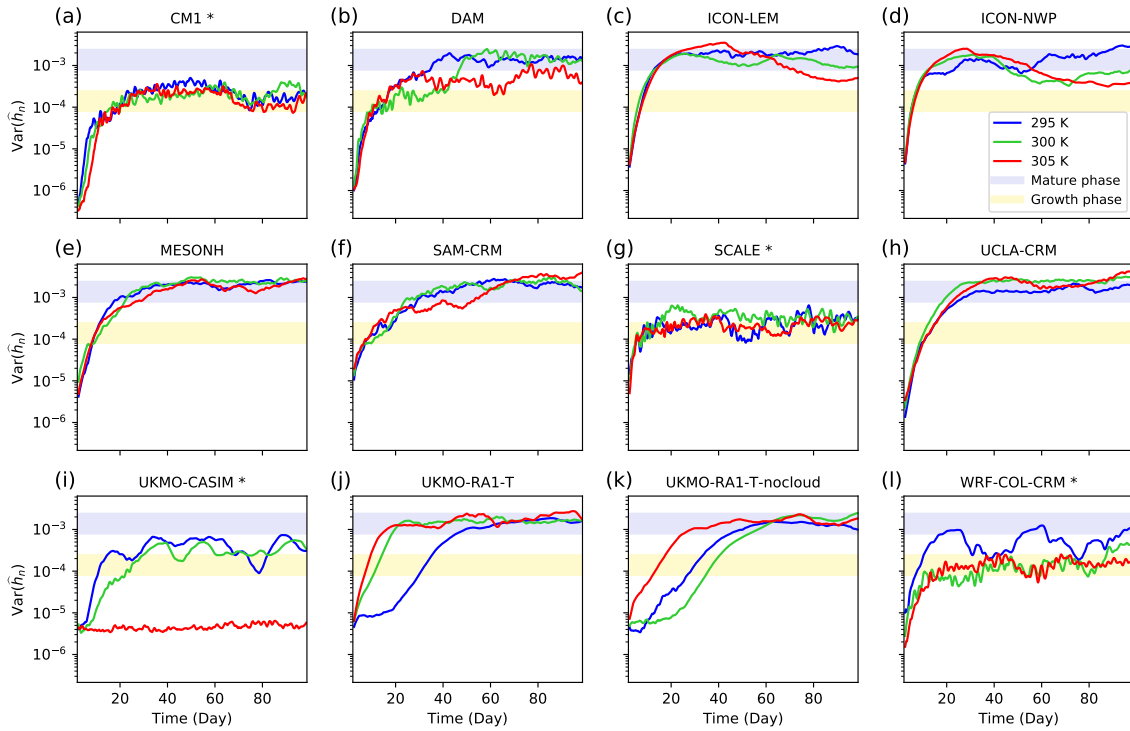


Figure 4.3: Time series of  $\text{var}(\hat{h}_n)$  for each Smoothed CRM and SST neglecting the first two days accounting for model spin-up (24-hour running averages). The Growth and Mature phases are indicated by the yellow and blue shaded regions respectively. Models marked with an asterisk (\*) are excluded in future model-mean calculations as not all of their simulations reach the Growth and Mature phase for all SSTs.

aggregation at all three SSTs. These models are marked with an asterisk in Figure 4.3 and do not contribute to model-mean calculations to prevent skewing the results.

Figure 4.4 shows 24-hour running averages of  $\text{var}(\widehat{h}_n)$  for each GCM and SST. Also shown are the  $\text{var}(\widehat{h}_n)$  limits for the Growth and Mature phase of aggregation. All of the GCMs aggregate, again displaying a wide range of characteristics Wing et al. (2020). Like the majority of CRMs, dry patches develop and expand, while moist regions become moister and increasingly confined until an equilibrium state is reached. Unlike the CRMs, aggregation increases with SST in the majority of GCMs. GCMs that reach a more aggregated state at warmer SSTs do not usually aggregate faster as SST increases, but they tend to continue aggregating for a longer duration.

As with the CRMs, we do not include all GCMs in the model-mean calculations as not all models have data in both the Growth and Mature phases of aggregation for each of the SSTs. These models are marked with an asterisk in Figure 4.4. Note CAM5 and CAM6 have FMSE data only for the final 25 days of the 1095-day simulation. ICON-GCM at 300 K already has a variance greater than the upper limit for the Growth phase after two days (which we consider the spin-up period) so is not included in model-mean calculations. ECHAM6 and GEOS *are* included in the model-mean calculations because the 295 K simulations reach the Mature stage after the 100 days shown in Figure 4.4.

The Growth and Mature thresholds for a given model are fairly arbitrary. So any  $\text{var}(\widehat{h}_n)$  range which satisfies the criteria of the convection being randomly scattered (Growth) or strongly clustered (Mature) may be used to define the two phases to study any one particular model. However, we want each model to have the same  $\text{var}(\widehat{h}_n)$  thresholds to make the comparisons in this study as fair as possible. The Growth phase range chosen allows the vast majority of models to be included in the Growth phase. The convection becomes significantly clustered above the upper limit of the Growth phase. Having the lower limit of the Mature phase at  $0.8 \times 10^{-3}$  allows the ECHAM6 and GEOS GCMs to be included, but excludes the CM1, SCALE and UKMO-CASIM CRMs, which do

not become “strongly clustered”. Despite all models aggregating to some degree (except UKMO-CASIM at 305 K), we have chosen not to define the Growth and Mature phases relative to the evolution of aggregation within each model because of the extensive range in aggregation among the models. Using Growth and Mature phases defined in that way could result in confusion comparing feedbacks across models because those differences could either be due to changes between the models themselves or due to changes in aggregation. The Growth and Mature definitions used in this study have been chosen in an attempt to make comparisons between the models as fair as possible.

### 4.3.2 Normalised FMSE variance budget analysis

Figure 4.5 shows the spatiotemporal mean of the budget terms during the entirety of the Growth and Mature phase of aggregation for Smoothed CRMs and GCMs and for each SST. From this figure, we can see which FMSE covariances are enhancing or opposing aggregation at these different stages. The  $\text{var}(\hat{h}_n)$  tendency is calculated using a second-order finite difference approximation from 6-hourly calculated  $\text{var}(\hat{h}_n)$ . The diabatic terms are explicitly calculated from hourly-averaged data, whereas the advection term is calculated as a residual of the other terms. This is because the FMSE diagnostic is output as instantaneous values rather than hourly-averaged values for most models that provided it, and FMSE advection is not a diagnostic in all models. By comparing GCMs to the Smoothed CRMs, we remove biases that may be a result of the small-scale features that cannot be resolved in the larger grid spacing in GCMs. Also shown in this figure, are the model-mean longwave and shortwave feedbacks using clear-sky radiation. This allows us to quantify the influence clear-sky radiation on the radiative feedbacks.

Figure 4.5 shows that for all model types, and at all SSTs, FMSE feedbacks with longwave radiation and surface fluxes are typically the main drivers of self-aggregation in the Growth phase, however the magnitude of each feedback is highly variable from model to model. The shortwave term is consistently small and positive and has little inter-model

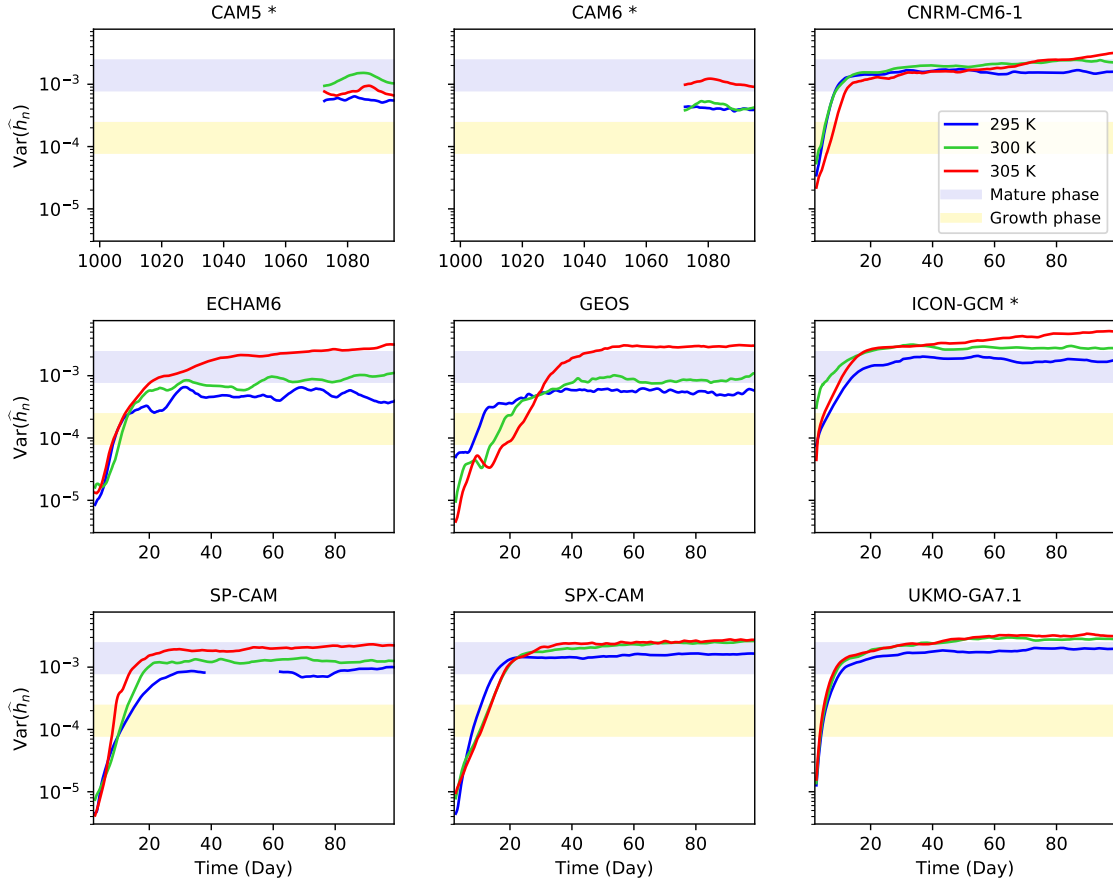


Figure 4.4: Time series of  $\text{var}(\hat{h}_n)$  for each GCM and SST for the first 100 days, neglecting the first two days accounting for model spin-up (24-hour running averages). Note that CAM5 and CAM6 only have FMSE output for the final 25 days of their 1095-day simulations, so we can only analyse that time period for those models. Also note there is missing data for the 295 K SP-CAM simulation from days 37-63 and days 762-800 due to errors in the model output. The Growth and Mature phases are indicated by the yellow and blue shaded regions respectively. Models marked with an asterisk (\*) are excluded in future model-mean calculations.

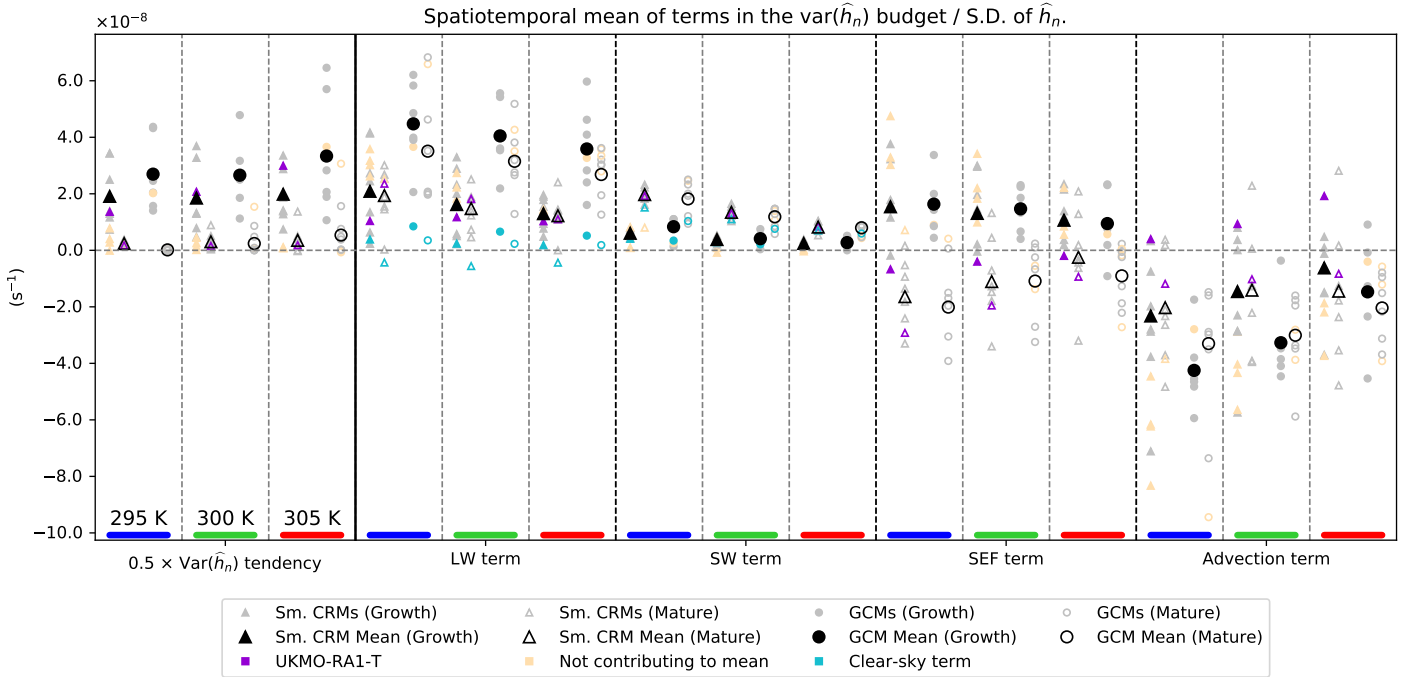


Figure 4.5: Spatiotemporal mean of terms in the  $\text{var}(\hat{h}_n)$  budget equation divided by the instantaneous standard deviation of  $\hat{h}_n$  for Smoothed CRMs (triangles) and GCMs (circles) at each SST during the Growth phase (filled markers) and Mature phase (open markers) of aggregation. For each term, SST increases to the right. The mean for the Smoothed CRMs and GCMs for each SST are shown in black markers. Models that do not reach both the Growth and Mature phase at all three SSTs are shown with orange markers and do not contribute to the mean. UKMO-RA1-T is shown in purple. Model-mean longwave and shortwave terms using clear-sky radiation are shown in cyan markers.

variability. The advection term typically opposes aggregation and is the greatest source of variability for the rate of aggregation across the models. The extensive variability in the budget terms highlights that the physical processes affecting aggregation are highly variable from model to model. In addition, the SST dependence of the model mean terms do not represent the SST dependence of the terms in each model. For example, Coppin and Bony (2015) studied the SST dependence of drivers of aggregation in the ISL-CM5A-LR GCM (not in RCEMIP), highlighting that the surface flux term becomes relatively more important as SST increases, in contrast to the RCEMIP model mean terms.

The RCEMIP CRMs that do not contribute to the model mean values are largely those models with waves that rapidly propagate across the domain and smooth horizontal humidity variations (CM1, SCALE, and WRF-COL-CRM). Deep convection occurs in these waves which generate high surface winds. Apparently related to these waves, these models tend to have higher than average longwave and wind-induced surface flux feedbacks, as well as a more negative advection feedback.

During the Mature phase of aggregation, both the longwave and shortwave feedbacks maintain aggregation, and are balanced by the typically-negative surface flux and advection feedbacks. On average, the magnitude of the longwave feedback has little dependence on the degree of aggregation in CRMs, but there is a slight decrease in the majority of GCMs with increased aggregation which is similar in magnitude to the decrease in the clear-sky longwave feedback. The shortwave feedback increases with aggregation as moist and dry regions amplify, leading to larger differences in shortwave absorption between positive and negative  $\widehat{h}'_n$  regions. The surface flux feedback is usually positive during the Growth phase as higher surface wind speeds in moist convective regions leads to a positive feedback. During the mature phase, the wind speed-surface flux feedback becomes overcompensated by the negative air-sea disequilibrium feedback, whereby surface evaporation rates are enhanced in drier environments (Wing and Emanuel, 2014). The surface flux feedback during the Mature phase at higher SSTs may be less negative due to the

wind-evaporation feedback being relatively stronger Coppin and Bony (2015).

The magnitude of the clear-sky longwave feedback is small in comparison to the total longwave feedback, decreasing slightly as aggregation increases, in agreement with Wing and Cronin (2016). The clear-sky shortwave feedback contributes to a much greater fraction of the total shortwave feedback compared to the clear-sky longwave feedback. This is because the shortwave feedback is mainly driven by the shortwave absorption by water vapor, which comprises a greater fraction of the total shortwave feedback as SST increases (Wing and Emanuel, 2014; Wing and Cronin, 2016; Pope et al., 2021).

As noted by Wing et al. (2020), GCMs tend to reach a higher degree of aggregation at higher SSTs. With only a slight increase in aggregation rate with SST in GCMs during the Growth phase, aggregation rates increase with SST most significantly for  $\text{var}(\hat{h}_n)$  in between the Growth and Mature phases. This can be seen in many of the models in Figure 4.4. Note that in Figure 4.5, the  $\text{var}(\hat{h}_n)$  tendency of GCMs during the Mature phase continues to increase slightly with SST.

For GCMs during the Growth phase, the sum of the diabatic terms decrease in magnitude with increasing SST, yet the advection term becomes more positive with SST, resulting in a small SST dependence in the rate of aggregation in the Growth phase. After the Growth phase however, the sum of the diabatic feedbacks becomes less SST dependent (because the surface flux feedback becomes more positive with increased SST), while the advection term remains more positive with SST. This results in a greater rate of aggregation after our defined Growth phase. In CRMs, the sum of the diabatic terms also becomes less sensitive to SST after the Growth phase, though they still have a more negative SST dependence than the average of the GCMs. The SST sensitivity of the CRMs' advection feedback tends to oppose the SST sensitivity of their diabatic feedbacks at all stages of aggregation.

The longwave feedback is on average a factor 2 greater in GCMs compared to CRMs for all stages of aggregation. The larger longwave feedback in GCMs is the main difference in

terms of the diabatic feedbacks between CRMs and GCMs. This results in GCMs having an overall larger diabatic feedback, corresponding to a more negative advection feedback and/or a higher rate of aggregation in the Growth phase. There is, however, a large spread in the models' advection term and aggregation rate. The difference between the mean advection term between GCMs and Smoothed CRMs is not statistically significant at the 95% confidence level for a given SST, even when including the models that are neglected from the model-mean comparisons. The increase in mean aggregation rate from the Smoothed CRMs to the GCMs is only significant at each SST when we include the models neglected from the model-mean comparisons. The difference in the longwave feedbacks in CRMs and GCMs is significant and will be discussed further in Section 4.4.2.

There is little difference in the budget terms between the non-Smoothed and Smoothed CRMs (not shown). After dividing the terms by the standard deviation of  $\hat{h}_n$ , the rate of aggregation, longwave term, and shortwave term remain similar on average. The most significant difference between the non-Smoothed and Smoothed CRMs is the magnitude of the surface flux term during the Growth phase, which is about 40% smaller in the Smoothed CRMs. We do not have an explanation for why this is. With the surface flux term decreasing in the Growth phase, and the other diabatic terms and  $\text{var}(\hat{h}_n)$  tendency term remaining similar, the advection term becomes more positive after smoothing as it is calculated as a residual of the other terms.

If FMSE feedbacks in CRMs and GCMs are represented similarly despite the different grid spacings, the budget terms in GCMs should be similar to the budget terms in the Smoothed CRMs. For both CRMs and GCMs, each of the diabatic terms are typically positive during the Growth phase but on average decrease in magnitude as SST increases (Figure 4.5). The SST dependence of the radiative terms found here is only in partial agreement with P21, who studied the UKMO-RA1-T model simulations which are represented by the purple, triangular data points in Figures 4.5, 4.7 & 4.8. They analysed this SST dependence of the UKMO-RA1-T CRM and found the longwave feedback de-

creases with increasing SST due to the reduction of high-cloud fraction at higher SSTs. However in their study, this SST dependence was only found in the Mature phase. We explore how high-cloud fraction affects the longwave feedback in the RCEMIP CRMs and GCMs in Section 4.4. P21 found that the shortwave feedback decreases with increasing SST, and is inversely proportional to the difference between  $\hat{h}_{\max}$  and  $\hat{h}_{\min}$ . This finding is consistent with the RCEMIP models and physically means that the shortwave heating anomalies contribute similar amounts to increasing the non-normalised FMSE variance at different SSTs. This is because the range of water vapor path (WVP) increases with SST, while the radiative absorption efficiency decreases with increasing WVP Vaquero-Martínez et al. (2018) resulting in little difference in horizontal net shortwave heating variance with SST. However, since FMSE anomalies are higher at warmer SSTs, the shortwave heating anomalies contribute to a smaller fraction of FMSE variance.

Some of the results from the mean of the models are in contrast to the results found in P21. According to the model means, the surface flux feedback is almost as important as the longwave feedback in driving aggregation, which is in stark contrast to the UKMO-RA1-T model that shows the surface flux feedback to be slightly negative even during the Growth phase. This suggests the air-sea disequilibrium feedback in the UKMO-RA1-T model dominates over the wind speed-surface flux feedback to a larger degree than in the majority of models. The sum of the diabatic terms decreases with increasing SST for the model means, yet it is more constant with SST in the UKMO-RA1-T simulations and is also more negative. Despite the more negative diabatic feedback in UKMO-RA1-T, the rate of aggregation is faster than the model means at 300 K and 305 K. This is because the UKMO-RA1-T model has the most positive advection feedback of all models. This feedback increases with SST despite the diabatic terms remaining similar, resulting in faster aggregation at higher SSTs in UKMO-RA1-T. For both CRMs and GCMs in RCEMIP, the advection term is inversely proportional to the sum of the diabatic terms, becoming less negative with increasing SST. The result is that the rate of aggregation

during the Growth phase for both CRMs and GCMs does not depend strongly on SST.

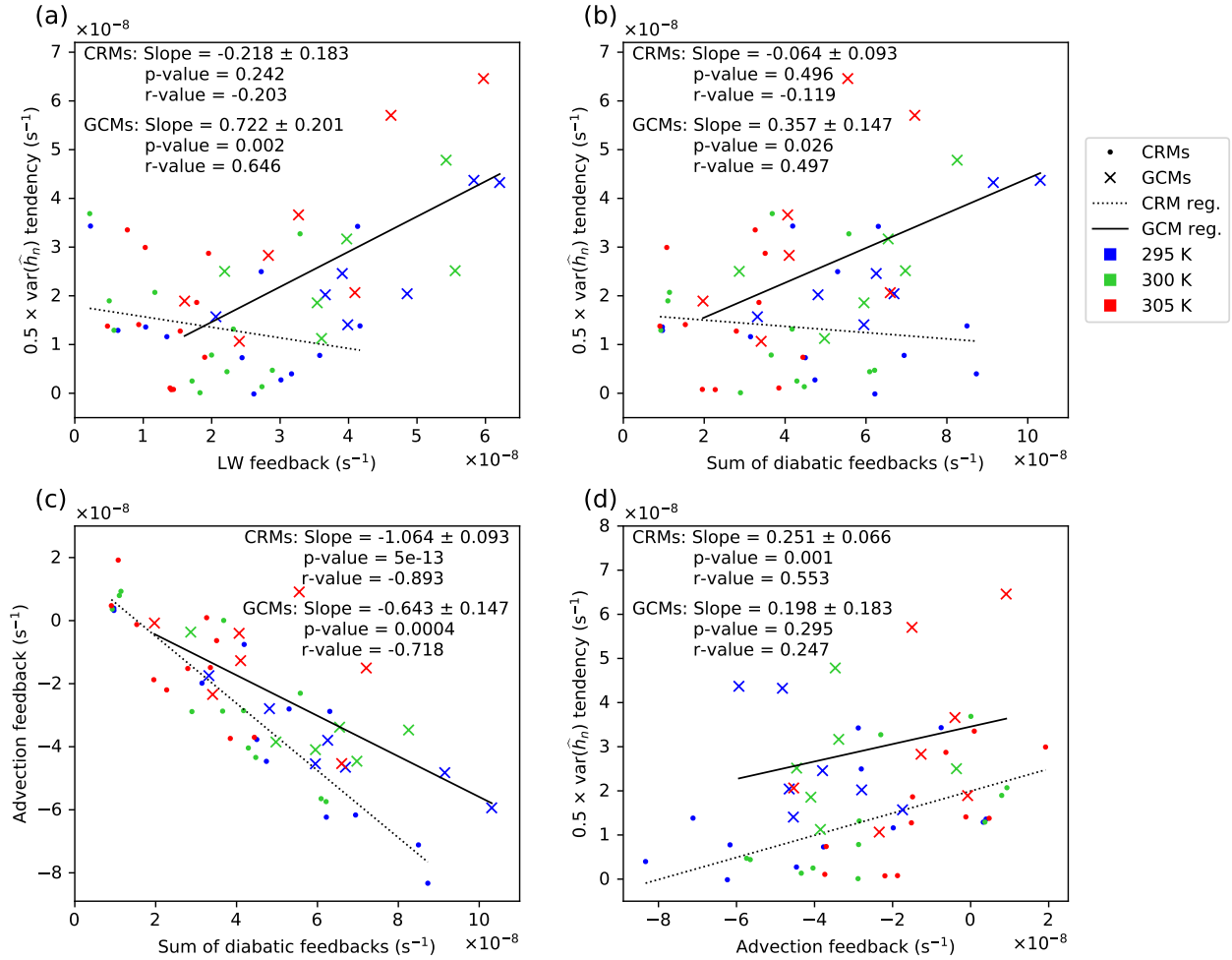


Figure 4.6: (a) Average of the  $\text{var}(\hat{h}_n)$  tendency term vs the longwave term in Equation (2.2), (b) average of the  $\text{var}(\hat{h}_n)$  tendency term vs the sum of the three diabatic terms (longwave, shortwave & surface flux), (c) average of the advection term vs the sum of the diabatic terms, and (d) average  $\text{var}(\hat{h}_n)$  tendency term vs the advection term, for each Smoothed CRM (points) and GCM (crosses) averaged over the Growth phase. Also shown is the regression line for CRMs (dotted) and GCMs (solid line), as well as their slope, p-value and r-value.

Previous literature has shown the diabatic terms to be essential drivers of aggregation, so we would expect that a greater diabatic-FMSE feedback would lead to an increased rate of aggregation. Despite the diabatic terms driving aggregation in the Growth phase

of the RCEMIP simulations (Figure 4.5), we cannot conclude that the magnitude of the sum of the diabatic terms is correlated to the rate of aggregation. Figure 4.6a shows the correlation between the longwave term and the  $\text{var}(\widehat{h}_n)$  tendency term in Equation (2.2) during the Growth phase for Smoothed CRMs and GCMs. We find there is a significant correlation between the longwave term and rate of aggregation in the GCMs, but there is no significant correlation between the longwave term and rate of aggregation in the CRMs (regardless of Smoothing). Figure 4.6b shows the correlation between the sum of the diabatic terms and the  $\text{var}(\widehat{h}_n)$  tendency term. Again there is a significant positive correlation between the diabatic feedbacks and rate of aggregation in the GCMs, but not for the CRMs. A greater diabatic feedback is associated with a more negative advection feedback (Figure 4.6c). In the CRMs, the sum of the diabatic terms is, on average, proportional to the magnitude of the advection feedback, hence there is no significant relationship between the diabatic feedbacks and aggregation rate. There is a less negative relationship between the sum of the diabatic terms and the advection term in the GCMs, allowing GCMs with a higher diabatic feedback to aggregate faster. The rate of aggregation in CRMs is most strongly correlated with the advection feedback (Figure 4.6d), with no significant correlation between the advection feedback and aggregation rate in the GCMs.

The longwave feedback is one of the key drivers and maintainers of aggregation in the majority of models at each SST. It is typically a larger feedback in GCMs, resulting in largely faster aggregation rates compared to CRMs. The longwave feedback is a major factor in determining the model spread in the rate of aggregation in GCMs. We explore the contributions of different cloud-radiation interactions to the longwave feedback in the following section. We assess their SST sensitivities, and compare and contrast CRMs and GCMs.

## 4.4 Contributions of Cloud-Radiation Interactions to Aggregation

In this section, we compare longwave-cloud interactions within the CRMs and GCMs. We first study these interactions in the CRMs to test the robustness of the conclusions in P21. We then compare CRMs to GCMs by first seeing how cloud-longwave interactions are affected by coarsened grid spacing using the Smoothed CRMs. Then we compare the Smoothed CRMs to GCMs to study why the longwave feedback tends to be stronger in GCMs.

### 4.4.1 Cloud-Radiation Interactions within CRMs

The contributions to aggregation from longwave interactions with each of the cloud types in Table 4.1 for CRMs and Smoothed CRMs are shown in Figure 4.7a, comparing SST and phase of aggregation. Each model that contributes to the mean is shown in grey, the model mean shown in black, UKMO-RA1-T is shown in purple, and models that do not contribute to the mean are shown in light orange. The model-mean contributions to the longwave term using clear-sky radiation are shown in the cyan points. We first focus on the (non-Smoothed) CRMs.

There is great variability between the models in terms of cloud fraction, and the  $LW'$  and  $\widehat{h}'_n$  of the different cloud types, so the factors affecting the longwave feedback vary considerably from model to model. However, for the CRMs during the Growth phase of aggregation, longwave interactions with the Clear and Deep regions typically contribute most to the longwave feedback. The Clear regions have a large contribution mainly because of their large domain-fraction (Figure 4.7b) and positive  $LW'_n \times \widehat{h}'_n$  covariance (Figure 4.7c), despite the covariance being on average the lowest in magnitude out of all cloud types. Deep clouds are the next most abundant cloud type on average and typically have the largest  $LW'_n \times \widehat{h}'_n$  covariance of all cloud types. They have the largest  $LW'_n$  due to their

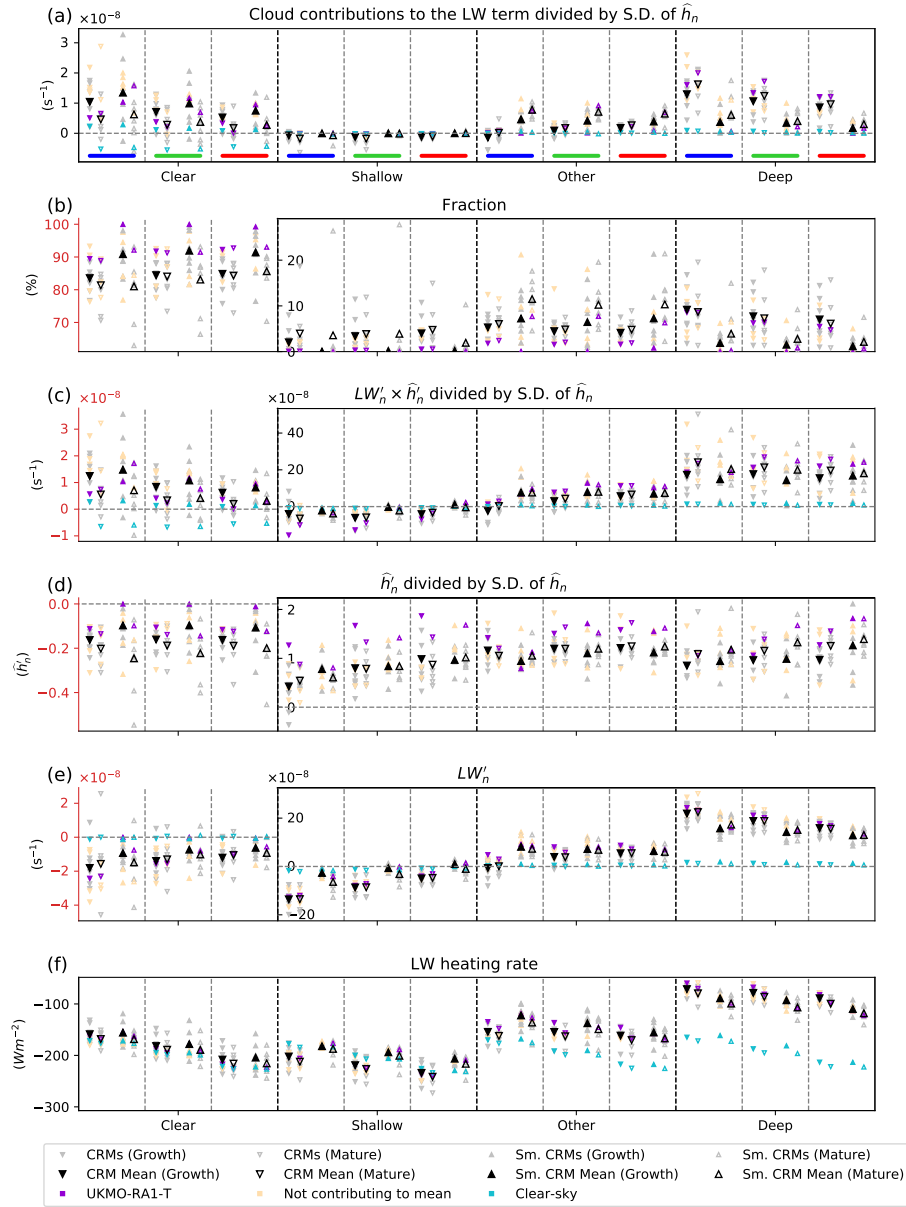


Figure 4.7: CRMs (downward triangles) vs Smoothed CRMs (upward triangles): (a) Contributions of longwave interactions for each cloud type in Table 4.1 to the longwave term in Equation (2.2) (equal to the cloud type fraction multiplied by their mean  $LW'_n \times \widehat{h}'_n$  covariance) divided by the standard deviation of  $\widehat{h}_n$ , (b) cloud type fraction, (c)  $LW'_n \times \widehat{h}'_n$  covariance divided by the standard deviation of  $\widehat{h}_n$ , (d)  $\widehat{h}'_n$  divided by the standard deviation of  $\widehat{h}_n$ , (e)  $LW'_n$ , and (f) net longwave heating (Equation 1.3). Data points represent spatiotemporal means. The layout follows the same protocol as Figure 4.5. Note different y-axis ranges for Clear in b, c, d & e.

cold cloud tops (Figure 4.7e) and have the second highest  $\widehat{h}'_n$  of the cloud types (Figure 4.7d). A large portion of the Deep category comes from thin anvil cloud which often extend a great distance from the high-FMSE updraft that they originated from. This transport of high cloud to lower-FMSE regions lowers the average  $\widehat{h}'_n$  of the Deep category. The Shallow and Other cloud types have an insignificant contribution to the longwave feedback in comparison because their  $LW'_n \times \widehat{h}'_n$  covariance is small in magnitude (mostly due to a small-magnitude  $LW'_n$ ) and they have a small fraction (although the fraction is highly variable between models).

The negative SST dependence of the longwave feedback, as seen in Figure 4.5, can be explained by the negative SST dependence of the longwave interactions with the Deep and Clear regions as follows, in agreement with P21. During both the Growth and the Mature phases, the  $LW'_n \times \widehat{h}'_n$  covariance of the Deep regions remains similar with SST (Figure 4.7c) while the Deep cloud fraction steadily decreases (Figure 4.7b), so the SST dependence of the Deep cloud's longwave contribution to aggregation is primarily due to the decrease in Deep cloud fraction.

The contribution of the Clear regions decreases with increasing SST due to the decrease in the Clear  $LW'_n \times \widehat{h}'_n$  covariance. We do not find the clear-sky longwave feedback in the Clear regions decreasing with SST by the same extent, indicating that the SST sensitivity of the Clear regions' longwave feedback is a side effect of the cloud response to SST. There are multiple factors that influence this SST dependence: the change in longwave heating rates of the different cloud types, the change in their fraction, the increase in the range of  $\widehat{h}_{\max}$  and  $\widehat{h}_{\min}$ , and the change in correlation between longwave and FMSE anomalies in the Clear regions. The correlation between  $LW'_n$  and  $\widehat{h}'_n$  remains similar with SST (15% decrease in the correlation coefficient from 0.173 at 295 K to 0.147 at 305 K), as does the mean  $\widehat{h}'_n$  (Figure 4.7d). The change in the Clear  $LW'_n \times \widehat{h}'_n$  covariance is therefore mainly due to the change in Clear  $LW'_n$ .

To isolate the effects of the changing longwave heating rates with SST on the Clear

longwave feedback, we use the average cloud type fractions at 295 K with the average cloud type longwave heating rates at 305 K. By taking the sum of the product of these cloud fractions and their longwave heating rates, we calculate a hypothetical new domain-mean longwave heating rate. Then a new hypothetical  $LW'$  for each cloud type is calculated by subtracting the new domain-mean heating rate from the cloud type net longwave heating rates. We find that the average Clear  $LW'$  becomes 74% more negative compared to the values at 295 K. However, after normalising  $LW'$  to account for the changing SST, we find this hypothetical new Clear  $LW'_n$  is largely insensitive to SST. We next isolate the effect of the changing cloud fraction with SST by using the average cloud type longwave heating rates at 295 K with the average cloud type fractions at 305 K to calculate the cloud types'  $LW'$ . We find the domain-mean longwave cooling rate increases by approximately  $3 \text{ W m}^{-2}$  compared to the value at 295 K, and is mainly a result of the decreasing Deep cloud fraction allowing for enhanced radiative cooling. The increased domain-mean cooling rate is closer to the mean cooling rate of the Clear regions, making their  $LW'$  37% less anomalously negative. This is close to the actual 30% decrease in the mean  $LW'_n$  of the Clear regions. This shows that the SST sensitivity of the Clear  $LW'_n$  is primarily due to changes in cloud fraction with SST.

The contribution of the clear-sky longwave feedback to the total feedback is negligible in the cloudy regions (Figure 4.7a). This is because the clear-sky longwave heating anomalies are much smaller than the total longwave heating anomalies (Figure 4.7e), showing that the longwave feedback is mainly a result of the longwave interactions with clouds. Even the Clear regions' longwave contribution is more positive than the clear-sky feedback because the longwave anomalies in Clear regions are more anomalously negative within a domain containing clouds.

For the Clear regions, the decrease in their longwave feedback with increasing aggregation is largely a clear-sky effect, with their total longwave feedback and their clear-sky longwave feedback decreasing by a similar magnitude (Figure 4.7a & c). On average, the

Clear regions'  $LW'_n$  remains similar with aggregation (becoming very slightly more positive) and their  $\widehat{h}'_n$  becomes more negative. But the changes in these model-mean values are not enough to explain the decrease in the mean  $LW'_n \times \widehat{h}'_n$  covariance in the Clear regions. The decrease in this covariance must be due to a decrease in the correlation between  $LW'_n$  and  $\widehat{h}'_n$  as aggregation increases, which is a clear-sky radiation effect. During the Growth phase, there is a positive correlation between  $\widehat{h}'_n$  and clear-sky  $LW'_n$ . This is because regions with increasingly positive  $\widehat{h}'_n$  have a greater column-integrated WVP, thus a higher effective level of OLR emission, reduced OLR (Allan et al., 1999), and therefore a higher  $LW'$ . During the Mature phase, there is a greater abundance of extremely dry regions. In these extremely dry regions, an increase in WVP more readily lowers the effective emission level of downwelling longwave radiation (Ruckstuhl et al., 2007) than increases the effective emission level of OLR (Chapter 3, Figure 3.14). The consequence is increasingly negative  $LW'$  at higher  $\widehat{h}'_n$ . This is a negative correlation, and helps to make the total Clear longwave feedback more negative in the Mature phase. The transition of the driest regions' clear-sky longwave feedback from initially positive to negative as aggregation increases is also described by Wing and Emanuel (2014), who explain it as a competition between local and remote effects using a simple two-layer model.

Next, we look at the effects of smoothing on cloud-longwave interactions in the CRMs to see how a coarser grid spacing affects cloud-longwave interactions. After smoothing the TOA radiative fluxes and reclassifying the cloud types using the smoothed radiation, there is a large difference in the fraction of the different cloud types (Figure 4.7b). Firstly, there is an almost complete elimination of Shallow cloud in the Smoothed CRMs during the Growth phase, with a large reduction in Deep cloud in the Growth and Mature phases. This is because the Shallow and Deep clouds are often small in area, particularly during the Growth phase, meaning that after averaging the TOA radiative fluxes across the surrounding  $120 \text{ km} \times 120 \text{ km}$  area, these clouds are often reclassified as either Clear or Other clouds. This results in an increase in Other cloud, although there is an approximate

halving of the total cloud fraction during the Growth phase. During the Mature phase, all cloud types increase in fraction in the Smoothed CRMs as a likely result from increased cloud clustering. The total cloud fraction in the Mature phase is similar to the non-Smoothed CRMs.

Smoothing also has an effect on the average  $LW'_n \times \widehat{h}'_n$  covariance of the cloud types (Figure 4.7c). The covariance remains similar for Deep cloud, but increases slightly for the Other cloud, perhaps a result of a significant proportion of the non-Smoothed Deep cloud regions becoming reclassified as Other after Smoothing, as can be inferred by comparing Figures 4.2a & b. The combined effects of the change in cloud fraction and  $LW'_n \times \widehat{h}'_n$  covariance after Smoothing is a reduction in the contribution from Deep cloud with subsequent increases in the contributions from the Other and Clear cloud types during all stages of aggregation. Smoothing has a negligible effect on the clear-sky longwave feedback.

#### 4.4.2 Comparison of Cloud-Radiation Interactions within CRMs and GCMs

In Figure 4.8, we compare the longwave-cloud interactions between the Smoothed CRMs and GCMs. Figure 4.8a shows that during the Growth phase, longwave interactions with the Clear regions and Deep regions are the main drivers of self-aggregation for GCMs, with interactions with Other clouds also having a significant contribution. Contributions of each of these cloud types to the total longwave feedback are higher in GCMs compared to the Smoothed CRMs. This is largely due to the increased fraction of the Other and Deep cloud types (Figure 4.8b), but also the increased  $LW'_n \times \widehat{h}'_n$  covariance of the Deep and Clear cloud types (Figure 4.8c).

The absolute net longwave heating rate (defined in Equation 1.3) of Deep cloud is similar in the Smoothed CRMs and GCMs, but in the Clear regions, the longwave heating rate is more negative on average for GCMs (Figure 4.8f). Given that the clear-sky

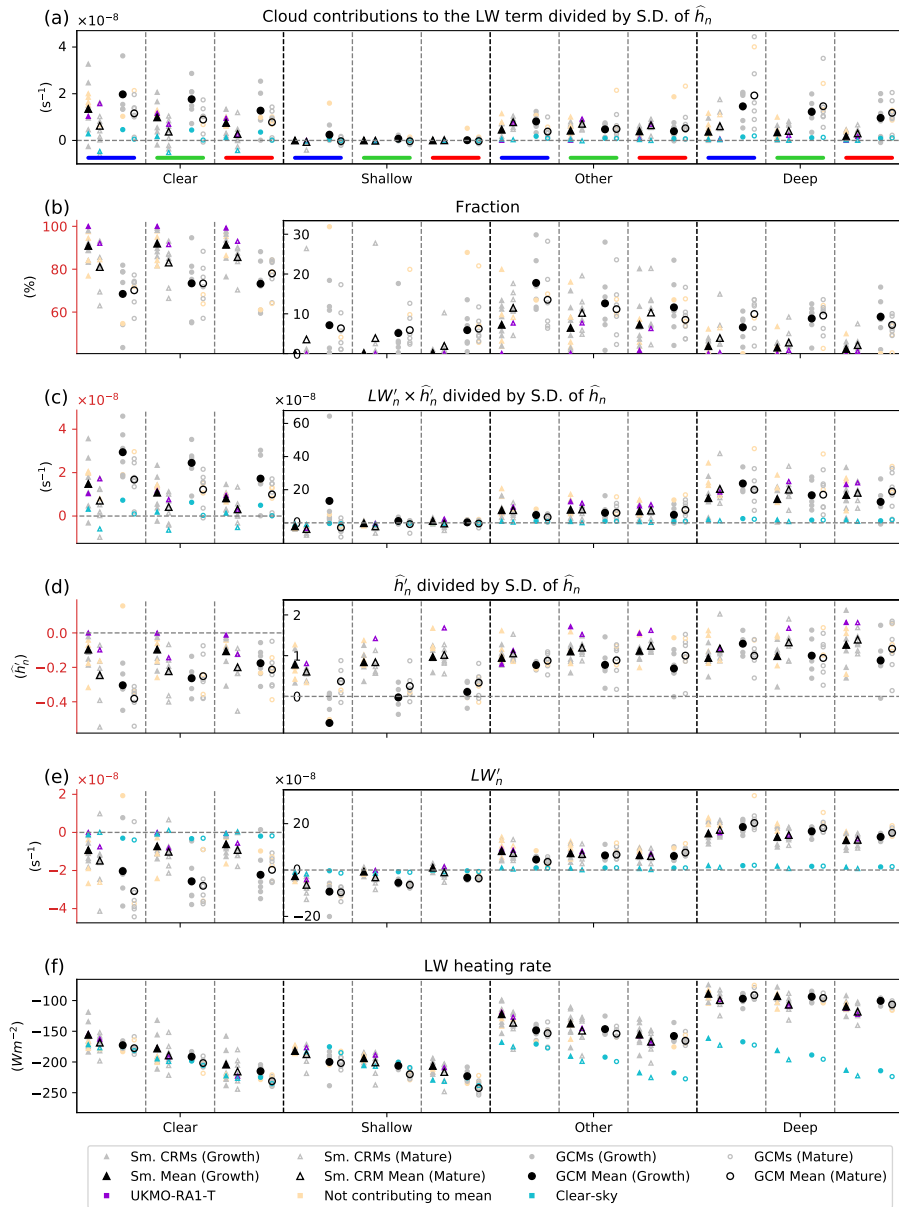


Figure 4.8: Smoothed CRMs (upward triangles) vs GCMs (circles): (a) Contributions of longwave interactions for each cloud type in Table 4.1 to the longwave term in Equation (2.2) (equal to the cloud type fraction multiplied by their mean  $LW'_n \times \hat{h}'_n$  covariance) divided by the standard deviation of  $\hat{h}_n$ , (b) cloud type fraction, (c)  $LW'_n \times \hat{h}'_n$  covariance divided by the standard deviation of  $\hat{h}_n$ , (d)  $\hat{h}'_n$  divided by the standard deviation of  $\hat{h}_n$ , (e)  $LW'_n$ , and (f) net longwave heating (Equation 1.3). Data points represent spatiotemporal means. The layout follows the same protocol as Figure 4.5. Note different  $y$ -axis ranges for Clear in b, c, d & e.

longwave heating rate in the Clear regions is similar in CRMs and GCMs, the decreased longwave cooling in CRMs is likely a result of more thin high cloud being present in the Clear regions. Since Clear regions occupy the majority of the domain, the domain-mean longwave emission is closely linked to that of the Clear regions. This makes the  $LW'_n$  of Deep clouds in GCMs more positive  $LW'_n$  (Figure 4.8e), and helps to increase the mean  $LW'_n \times \widehat{h}'_n$  covariance of Deep clouds.

The  $LW'_n \times \widehat{h}'_n$  covariance of the Clear regions is more than double that of the Smoothed CRMs. This is in part because Clear regions in GCMs typically occur in more negative  $\widehat{h}'_n$  regions compared to Smoothed CRMs (Figure 4.8d), which is a likely consequence of the greater cloud fraction in GCMs, confining the Clear regions to drier environments. The  $LW'_n$  is also more negative in GCMs partially due to the mean net longwave heating rates being more negative on average, but mainly because of the difference in cloud fraction between the model types. To isolate the effect of the difference in cloud fraction between CRMs and GCMs on the Clear regions' longwave feedback, we use the mean longwave heating rates of the cloud types in the Smoothed CRMs with the cloud fractions of the GCMs. We then calculate a hypothetical new domain-mean longwave cooling by taking the sum of the product of these cloud fractions and net longwave heating rates and then find the new hypothetical cloud type  $LW'$ . We find that the  $LW'_n$  of the Clear regions becomes approximately 2.5 times more negative. This is thanks to the Deep and Other clouds lowering the domain-mean longwave cooling rate in GCMs, hence making the Clear regions more anomalously negative. These effects suggest that the greater high-topped cloud fraction in GCMs is a key factor in the enhanced total longwave-FMSE feedback, and therefore rate of aggregation in GCMs compared to CRMs. The non-Smoothed CRMs have a similar Deep cloud fraction and Deep  $LW'_n \times \widehat{h}'_n$  covariance to the GCMs, yet the contributions from Other and Clear cloud types remain larger in GCMs thanks to the increase in the Other cloud fraction in GCMs. The increase in Other cloud fraction, with their positive  $LW'$ , helps further lower the (negative)  $LW'$

of the Clear regions in GCMs compared to non-Smoothed CRMs, helping increase these cloud types' contributions to the longwave feedback.

As the convection reaches the Mature phase, longwave interactions in the Clear, Other and Deep cloud types maintain aggregation in the Smoothed CRMs. For GCMs, longwave interactions with the Clear and Deep cloud types are the key maintainers of aggregation. The contribution from the Clear regions decreases with aggregation in both the CRMs and GCMs because of the clear-sky effect described in Section 4.4.1. Despite the GCMs having a larger Shallow fraction, these clouds have a similarly insignificant contribution to the longwave feedback as in the Smoothed CRMs. Their  $LW'_n \times \widehat{h}'_n$  covariance is consistently close to 0 because both their  $LW'_n$  and  $\widehat{h}'_n$  are small.

The SST sensitivity of the longwave feedback in GCMs is less straightforward than CRMs with multiple factors playing a role. As with the CRMs, there is great variability between the models in the factors affecting the longwave feedback. On average, during the Growth and Mature phases, the longwave feedback decreases with increasing SST because of a decrease in the contributions from the Clear and Deep categories. The decrease in the contributions from Clear regions comes from their decreasing  $LW'_n \times \widehat{h}'_n$  covariance. During both phases of aggregation, the Clear  $\widehat{h}'_n$  becomes less negative, which is in part a result of the decreased Deep and Other cloud fraction. These clouds form in anomalously positive  $\widehat{h}'_n$  regions, so a decrease in their abundance with increasing SST will result in an increase in anomalously moist Clear regions, thus decreasing the mean Clear  $LW'_n \times \widehat{h}'_n$  covariance. The main factors responsible for the decreasing contribution from Deep cloud is the increase in the range of  $\widehat{h}_{\max}$  and  $\widehat{h}_{\min}$  that is used to normalise the longwave heating anomalies, as well as a decrease in their average  $\widehat{h}'_n$  in the Growth phase.

## 4.5 Conclusions

In this chapter, we compare the effects of cloud-radiation interactions on convective self-aggregation within the CRMs and GCMs submitted to RCEMIP (Wing et al., 2018, 2020). We use the normalised vertically-integrated FMSE variance ( $\text{var}(\widehat{h}_n)$ ) budget framework to study aggregation (Pope et al., 2021, referred to as P21.), and define “Growth” and “Mature” phases of aggregation to compare how FMSE feedbacks contribute to aggregation at similar stages of aggregation across the range of models. We define four different cloud types based on the top of atmosphere radiative fluxes following the method from Becker and Wing (2020) and calculate the contribution of radiative interactions with these cloud types to aggregation. These cloud types are: Clear, Shallow, Deep and Other. GCMs have on average a 40 times larger grid spacing than CRMs. When comparing these two model types we account for biases in our analysis technique due to the resolution difference by horizontally smoothing the CRMs so that each grid point is an average of the  $40 \times 40$  grid points surrounding it, referred to as Smoothed CRMs.

The goals of the study are to:

- Validate the robustness of the results in P21 who studied the effects of cloud-radiation interactions on self-aggregation within the Met Office Unified Model version 11.0 CRM (submitted to RCEMIP and referred to as “UKMO-RA1-T”).
- Investigate to what extent differences in cloud-radiation interactions affect self-aggregation within CRMs and GCMs, and how these are sensitive to SST.

### 4.5.1 Robustness of Pope et al. (2021) results

We consider the robustness of the following five conclusions from P21:

1. Key **drivers** of aggregation are longwave interactions with high-topped clouds and Clear regions. (*Robust*)

Most CRMs and GCMs are in agreement with this conclusion when considering that Deep cloud are mostly equivalent to high-topped clouds in P21. Deep clouds have strong longwave heating anomalies and occur in anomalously moist regions. Clear regions typically have negative longwave heating anomalies and tend to occur in anomalously dry regions. Both of these radiative interactions result in a strongly positive longwave feedback.

2. The main **maintainers** of aggregation are longwave interactions with high-topped clouds and shortwave interactions with water vapour. (*Robust*)

Most CRMs and GCMs are in agreement that these radiative interactions are key maintainers of aggregation. The shortwave feedback increases with aggregation as moist and dry regions amplify, leading to a greater contrast in shortwave absorption by water vapour between the moist and dry regions, resulting in an enhanced shortwave-FMSE feedback.

3. The main **resistors** of aggregation are negative surface flux and advection feedbacks. (*Not Robust for surface flux in the Growth phase*)

In the majority of models, the surface flux feedback is actually a key *driver* of aggregation, with the UKMO-RA1-T model having the most negative surface flux contribution during the Growth phase. In most models, this is likely due to a strong wind speed-induced surface flux feedback outweighing the air-sea disequilibrium feedback during the Growth phase of aggregation (unlike in UKMO-RA1-T where the opposite is true). As aggregation matures, the models are in agreement that the surface flux feedback becomes increasingly negative and often opposes aggregation. The advection feedback is typically negative and highly variable between models.

4. The **SST-dependence** of the longwave feedback is absent during the Growth phase, but is negative in the Mature phase. (*Not Robust for Growth phase*)

For the RCEMIP models, the domain-mean longwave feedback decreases with increasing SST at *all stages* of aggregation, which is primarily due to the decrease in Deep and/or Other cloud fraction at warmer SSTs. P21 also find the high-topped cloud fraction decreases with increasing SST, however this is compensated by an increase in their mean longwave-FMSE covariance in the Growth phase. We do not find the longwave-FMSE covariance of the Deep and Other clouds increasing with SST in the majority of RCEMIP models, hence their domain mean longwave feedback tends to decrease with SST.

The RCEMIP CRMs and GCMs differ in the processes leading to the decrease in the longwave feedback with increasing SST. For the CRMs, the average longwave-FMSE covariance of these clouds remains similar with SST, so the decrease in their cloud fraction reduces their total aggregating influence. A secondary effect of the decreased Deep cloud fraction is an increase in the magnitude of domain mean longwave cooling. This makes the typically-negative longwave heating anomalies of the Clear regions less anomalous, also decreasing the Clear regions' aggregating influence at warmer SSTs. In GCMs, the longwave feedback decreases with SST because the normalised longwave heating anomalies of Deep clouds decreases, reducing their aggregating influence. In addition, the Clear regions occur in less anomalously dry regions due to the reduced total cloud fraction, also reducing their average aggregating influence as SST increases.

5. The **SST-dependence** of the aggregation rate is positive because the advection feedback becomes increasingly positive with SST. (*Not Robust for SST-dependence of the aggregation rate. Robust for the SST-dependence of the advection feedback*)

P21 find the sum of the diabatic feedbacks are insensitive to SST during the Growth phase. However, for the RCEMIP CRMs and GCMs, each diabatic feedback tends to decrease with increasing SST during the Growth phase. Despite the sum of these

diabatic feedbacks decreasing with SST, the rate of aggregation remains similar on average. The sum of the diabatic feedbacks tends to be proportional to the magnitude of the (negative) advection feedback, resulting in little change in aggregation rate with SST.

#### 4.5.2 Differences between GCMs and CRMs

Using  $\text{var}(\hat{h}_n)$  as our aggregation metric, we find there is much variability in the rate of aggregation and the maximum degree of aggregation within the CRMs, with no consistent SST dependence on the rate of aggregation and the maximum degree of aggregation. GCMs, on the other hand, aggregate faster than CRMs on average, and tend to be more aggregated at higher SSTs.

Both the contributions of shortwave-FMSE and surface flux-FMSE feedbacks to aggregation are similar in magnitude in Smoothed CRMs and GCMs. However, the longwave-FMSE feedback is, on average, approximately twice as strong in GCMs compared with CRMs. This results in typically faster rates of aggregation in GCMs. This is primarily due to GCMs having a larger cloud fraction than Smoothed CRMs, but more crucially a larger Deep cloud fraction. However, if GCMs are instead compared to the non-Smoothed CRMs, GCMs have a similar Deep fraction but a larger Other fraction (which is mostly comprised of thinner high-topped cloud), which still results in a greater total longwave-FMSE feedback. The longwave-FMSE feedback is strongest for Deep clouds because they typically occur in anomalously-high FMSE regions, and have anomalously strong positive longwave heating rates. Like with the SST sensitivity of cloud fraction in CRMs, a secondary effect of the increased Deep cloud fraction in GCMs is an increase in the longwave-FMSE feedback in the Clear regions. This is because an increased cloud fraction reduces the magnitude of domain-mean longwave cooling. With Clear regions occupying the majority of the domain, their typically-negative longwave heating anomalies become more negative, increasing their longwave-FMSE feedback. The increase in the contributions from Deep

and Clear regions to the longwave-FMSE feedback accounts for the doubling of the total feedback.

As previously mentioned, the sum of the diabatic feedbacks with FMSE tend to decrease with increasing SST during the Growth phase, yet the aggregation rate remains insensitive to SST thanks to the increasingly positive advection feedback. After the Growth phase however, the sum of the diabatic feedbacks becomes less SST dependent, yet the advection feedback remains more positive at higher SSTs in GCMs, resulting in GCMs being more aggregated at higher SSTs. This finding, and the point made above about differences in cloud amount between GCMs and CRMs, suggests that GCMs should be compared more systematically to CRMs to investigate their total cloud amount.

Despite the difference in the diabatic feedbacks between GCMs and CRMs accounting for the difference in the aggregation rate between these model types, there is no evidence that the model spread in the magnitude of the diabatic feedbacks can explain the model spread in the rate of aggregation in CRMs. On average for CRMs, the magnitude of the (negative) advection feedback is proportional to the sum of the diabatic feedbacks. The advection term may be largely influenced by deep overturning circulations that transport FMSE from moist to dry regions, dampening aggregation. The rate of aggregation in CRMs is most strongly correlated with the magnitude of the advection term. Unlike in CRMs, the diabatic feedbacks are significantly correlated with aggregation rate in GCMs. This may suggest that the overturning circulations that smooth horizontal humidity gradients are relatively weaker compared to the diabatic feedbacks in GCMs than CRMs. One possibility is that GCMs are not capturing key circulations that would otherwise mediate aggregation, although circulations in CRMs could also be too strong. These effects are not investigated in this study.

We have shown that the production of cloud in CRMs and GCMs, in terms of quantity and distribution, is very different. This in turn, results in largely different longwave-FMSE feedbacks that alter the rate and degree of aggregation. Not only are the longwave-FMSE

interactions enhanced in GCMs, but there is a less negative correlation between the diabatic and advection feedbacks in GCMs than CRMs. This suggests that the response of circulations to diabatic heating are different in GCMs and CRMs. These factors highlight our limitations to accurately represent the cloud response to warming in climate studies. CRMs are often used to study the cloud response to warming, but are too small to capture the large-scale circulations that affect the total cloud feedback. GCMs are used in climate modelling studies because they are complete representations of the climate system, and they can perform hundreds of years of global-scale simulations. However, there are discrepancies in cloud-radiation interactions and circulations between GCMs and CRMs. Both CRMs and GCMs should be evaluated against observations in an effort to make these aspects of clouds and circulations more realistic.

In Chapter 5, we modify cloud radiation interactions within explicit and parameterised convection simulations to assess the sensitivity of aggregation and the advection feedback to these interactions to achieve our fourth thesis objective. This helps highlight key differences in the processes affecting aggregation between explicit and parameterised simulations. We test whether an enhanced cloud-longwave feedback in explicit convection simulations affects aggregation rate despite there being little connection between these feedbacks and aggregation rate in the RCEMIP CRMs. We also investigate whether aggregation in parameterised convection simulations behaves more similarly to explicit simulations if the cloud-radiation interactions are more similar.

## CHAPTER 5

# THE RESPONSE OF CONVECTIVE SELF-AGGREGATION TO ENHANCED RADIATIVE-CONVECTIVE INTERACTIONS IN EXPLICIT AND PARAMETERISED CONVECTION SIMULATIONS

### 5.1 Introduction

In our previous chapters, we have found that direct interactions between longwave radiation and FMSE are crucial drivers and maintainers of self-aggregation within both the explicit and parameterised convection simulations in RCEMIP. The longwave-FMSE feedback is often the dominant diabatic FMSE feedback throughout the RCEMIP simulations. Specifically, longwave interactions with high-topped clouds and clear regions have the greatest contributions to the total longwave-FMSE feedback, but longwave interactions with high-topped cloud directly and indirectly affects the longwave feedback in the cloudy and clear regions respectively. We have seen that the sum of the diabatic feedbacks with FMSE tend to decrease with SST during the Growth and Mature phases of aggregation, yet there is no consistent SST dependence on the aggregation rate in both the explicit and

parameterised convection simulations. In addition, despite the wide range in the magnitude of the diabatic feedbacks, there is no correlation between these feedbacks and the rate of aggregation amongst the explicit convection simulations. However, there is a significant correlation for the parameterised convection simulations, with higher diabatic feedbacks leading to faster aggregation. The reason for there being little correlation between these diabatic feedbacks and aggregation in the explicit convection simulations has to do with the response of the advection feedback to the diabatic feedbacks. The (typically negative) advection feedback becomes increasingly negative as the diabatic feedbacks increase, often leading to no relationship between the diabatic feedbacks and aggregation rate. With cloud-radiation interactions being one of the largest sources of variability amongst RCE models, the question is raised: To what extent would a change in cloud-radiation interactions affect the rate of aggregation?

Bretherton et al. (2005) showed in a sensitivity test that by artificially doubling the total radiative heating anomalies throughout every column, the rate of aggregation increases in an explicit convection simulation. This result seemingly opposes the results from Chapter 4. Many studies have then shown that radiative interactions with clouds are essential for the development of non-rotating aggregation through mechanism denial experiments (e.g. Muller and Held, 2012; Holloway and Woolnough, 2016). With these cloud-radiation interactions turned off, the convection does not aggregate. Cloud-radiative interactions aid the development of tropical cyclones in rotating domains, however they are not essential for tropical cyclone development (Wing et al., 2016). They help to accelerate tropical cyclone formation (Ruppert et al., 2020), and help to strengthen and broaden the cyclone's circulation Bu et al. (2014).

In non-rotating domains, aggregation often starts with the development of dry patches that continue to expand, confining convection into small, intensely precipitating regions. Fan et al. (2021) show that these dry patches are not guaranteed to continue expanding and amplifying without sufficient cloud-radiative forcing, otherwise deep convective circu-

lations could engulf these initial dry patches, preventing aggregation. They modify cloud radiative forcing in the model by adjusting the threshold radius of cloud ice crystals before they are converted to snow. A greater threshold radius increases anvil cloud fraction, thus increasing the cloud-longwave radiative effect, resulting in faster aggregation. By modifying this threshold, the vertical structure of clouds are modified. As the threshold is increased, anvil cloud fraction increases, whereas the low cloud fraction remains largely unchanged. Therefore, this approach only tests the sensitivity of aggregation to anvil cloud fraction.

By modifying the strength of cloud-radiation effects in the radiation scheme, we can test how the magnitude of cloud-radiation interactions affect convective self aggregation without explicitly affecting the cloud structure. In this chapter, we study the effects of modified longwave-cloud interactions on self-aggregation in idealised explicit and parameterised convection simulations.

## 5.2 Methods

### 5.2.1 Experiment Design

In this chapter, we use two sets of RCE simulations of the UK Met Office Unified Model. We run an explicit convection and a parameterised convection set, simulated over a fixed SST of 300 K. The explicit simulations are based on the *LARGE* simulations used in Chapter 3. This is an idealised, elongated channel simulation that is 6,048 km  $\times$  432 km in size with a 3 km horizontal grid spacing. The parameterised simulations are based on the the Met Office Unified Model Global Atmosphere (GA7.1, CMIP6 model version) (Walters et al., 2019) that has an RCEMIP GCM submission labelled “UKMO-GA7.1” (Wing et al., 2018). We have modified this version to occur on an elongated, bicyclic channel domain that is 6,040 km  $\times$  440 km (approximating the RCEMIP elongated channel domain explicit simulations) with a 20 km grid spacing.

We modify the cloud-longwave interactions by systematically scaling the parameter that controls the total cloud cover seen by the longwave radiation scheme within a grid column ( $C_{\text{tot}}$ ).  $C_{\text{tot}}$  is a parameter used in the Monte Carlo Independent Column Approximation (McICA) radiation scheme, developed by Pincus et al. (2003). The grid box cloud fraction itself is not directly affected by  $C_{\text{tot}}$ ; this parameter is only used by the longwave radiation scheme. In adjusting this parameter, we do not directly affect the cloud structures, we only affect the cloud’s radiative forcing. Each set has a “Control” simulation in which  $C_{\text{tot}}$  is not adjusted. Additionally, two experiments are performed: one with  $C_{\text{tot}}$  halved (“Halve”) and another with  $C_{\text{tot}}$  doubled (“Double”). Note that the Double simulations often have total cloud cover in the longwave radiation scheme greater than 100%, however this unphysical scenario does not result in model error and acts to enhance the cloud emissivity.

The McICA radiation scheme is used in GA7.1 by default, but we have had to modify the explicit convection model configuration to use McICA. This scheme is designed to be implemented in large-scale models with a coarse grid spacing on the order of dozens to hundreds of kilometres; within which, a wide variety of cloud structures could develop. It is designed to represent the radiative transfer of sub-grid cloud structures in a computationally-efficient and unbiased way, calculating 1-dimensional radiative fluxes vertically throughout the column. We have chosen to use this radiation scheme because it is straightforward to scale the radiative influence of cloud. In comparing the explicit Control simulation to the *LARGE* 300 K simulation in Chapter 3, we find very little difference in terms of rate and degree of aggregation, as well as the structure of aggregated convection.

The Independent Column Approximation (ICA) can quite accurately represent the domain mean radiative flux by calculating the clear-sky radiative flux and the average radiative flux within each possible vertical cloud structure, weighted by the probability of the cloud structure occurring (Cahalan et al., 1994; Barker et al., 1999). The ICA approximates radiative fluxes throughout a grid column ( $F^{\text{ICA}}$ ) by the equation:

$$F^{\text{ICA}} = (1 - C_{\text{tot}})F^{\text{clr}} + C_{\text{tot}}\overline{F^{\text{cld}}} \quad (5.1)$$

Where  $F^{\text{clr}}$  is the clear-sky radiative fluxes calculated at each vertical level throughout the column, and  $\overline{F^{\text{cld}}}$  is sum of radiative fluxes at each spectral band, averaged over all possible subgrid cloud structures. The subgrid cloud structures are calculated from cloud fraction and in-cloud condensate within each grid cell, which are then overlapped following additional overlap assumptions (using the stochastic cloud generator described by Räisänen et al. (2004) in our configuration).  $C_{\text{tot}}$  is the sum of the probabilities of these sub-grid cloud structures. Radiative fluxes are more uniform in clear skies compared to cloudy skies, so  $F^{\text{clr}}$  is only calculated once. It is usually very computationally expensive to calculate the full ICA of  $\overline{F^{\text{cld}}}$ , so the McICA scheme approximates  $\overline{F^{\text{cld}}}$  by calculating radiative fluxes for a number of sampled possible cloud structures. In our configuration, we use the Optimal Spectral Sampling method of McICA described by Räisänen and Barker (2004). This McICA method approximates  $\overline{F^{\text{cld}}}$  by the formula:

$$\overline{F^{\text{cld}}} \approx \sum_{k=1}^K \left( \frac{1}{N_k} \sum_{n=1}^{N_k} F_{n,k}^{\text{cld}} \right) \quad (5.2)$$

Where  $k$  is a spectral interval within the k-distribution of radiation,  $K$  is the number of spectral intervals used to approximate the k-distribution,  $N_k$  is the number of randomly selected cloudy subcolumns, and  $F_{n,k}^{\text{cld}}$  is the radiative flux of the randomly selected cloud column for the spectral interval. So, this is an approximate average radiative flux of the cloudy subcolumns within a grid column.

Rearranging Equation (5.1) gives Equation (5.3). In our experiments, we systematically scale  $C_{\text{tot}}$  for longwave radiation only, running experiments for Halve  $C_{\text{tot}}$  and Double  $C_{\text{tot}}$ . So we provide less or more weight to the cloudy columns in our experiments, therefore weakening or enhancing the effect of cloud-longwave interactions.

$$F^{\text{ICA}} = F^{\text{clr}} + C_{\text{tot}}(\overline{F^{\text{cld}}} - F^{\text{clr}}) \quad (5.3)$$

### 5.2.2 Analysis Framework

The cloud classification scheme used in this chapter is similar to that described in Section 3.2.2 and used in Chapter 3, but we combine some of the categories with similar longwave radiation properties for ease of analysis. The cloud classification scheme is originally based on that used by Hill et al. (2018) who use the vertical profile of condensed water content to define different cloud types. They use a lower and an upper pressure level threshold to define low, high and mid-level cloud, with cloud types spanning multiple levels having their own separate category. In Chapter 3, cloud types are defined by the vertical profile of condensed water in relation to the lower and upper thresholds, resulting in eight different cloud types: Clear, Low, Low & Mid, High, High & Low, High & Mid, and Deep. In this chapter, we ignore the low threshold. Here, a condensed water profile with cloud below the high threshold only is defined as “Shallow”, cloud above the high threshold only is defined as “High”, and cloud above the threshold in addition to cloud below is defined as “High+”.

In Chapter 3, we define the lower and upper thresholds based on the vertical distribution of cloud bases averaged throughout the entire large channel simulations (as in Figure 3.1 in Chapter 3). The high-level threshold is defined as the highest-altitude cloud base distribution local minimum. We use the mean cloud base distribution of the Control explicit convection simulation to define the threshold and we use this value for each of our simulations. The upper level threshold is 469 hPa.

We use the same variance of normalised frozen moist static energy (FMSE) budget framework that is based on the framework by Wing and Emanuel (2014) as described in Section 2.3. Aggregation is measured by the variance of normalised vertically-integrated FMSE ( $\text{var}(\widehat{h}_n)$ ). The framework allows us to compare the aggregating influence of feed-

backs between FMSE and longwave radiation, shortwave radiation, surface enthalpy fluxes, and advection of FMSE. Since we only analyse simulations over one SST in this chapter, we could have used the Wing and Emanuel (2014) framework and yielded the same results. However the use of the normalised framework allows us to compare these results to those in the previous chapters.

To make a fair comparison between our explicit and parameterised simulations, we horizontally smooth the explicit simulations in a similar way to the Smoothed CRMs in Chapter 4. The parameterised convection simulations have a grid spacing that is approximately 7 times greater than the explicit simulations. Therefore, we horizontally smooth the 2-dimensional and 3-dimensional fields so that each gridbox is an average of the  $7 \times 7$  gridboxes surrounding it. We only analyse the smoothed explicit simulations in this chapter.

We discuss the characteristics of the simulations in terms of two distinct phases of aggregation: one in which the aggregation is rapidly increasing (“Growth”) and another in which the domain displays strongly aggregated convection (“Mature”). The Growth phase for both the parameterised and explicit convection simulations is defined as any time at which  $\text{var}(\hat{h}_n)$  is between  $2 \times 10^{-4}$  and  $4 \times 10^{-4}$ . The Mature phase is defined as any time at which  $\text{var}(\hat{h}_n)$  is between  $1 \times 10^{-3}$  and  $2 \times 10^{-3}$ .

### 5.2.3 Expected Cloud-Longwave Forcing Response to Modified $C_{\text{tot}}$

By modifying the cloud-longwave radiation interactions through adjusting  $C_{\text{tot}}$ , we intend to alter the amount of longwave radiation absorbed and emitted by the cloud for a given condensed water content, thus altering the cloud column-integrated longwave heating anomalies. A simple schematic of radiative interactions with different cloud types is shown in Figure 1.1 and can be used to infer how modifying  $C_{\text{tot}}$  may impact the column longwave heating rates for each cloud type. As discussed in Chapter 1, and shown in Figures 3.9g & 4.8f, high-topped clouds anomalously warm the atmospheric column and

shallow clouds tend to have slightly greater longwave cooling than Clear columns. Equation (5.3) shows that as  $C_{\text{tot}}$  increases, the difference between the cloudy fluxes and clear fluxes will provide a larger contribution to the total radiative flux.

Equation (5.3) shows that when we halve  $C_{\text{tot}}$ , the contribution from the cloud fluxes ranges from 0% to 50% of the total flux, and the contribution from the clear-sky fluxes ranges from 50% to 100%. So we would expect the cloudy regions' cloud effects to be halved. When we double  $C_{\text{tot}}$ , we would expect the cloudy regions' cloud effects to be doubled. The contribution from the cloud fluxes ranges between 0% and 200%, and the clear fluxes contribute between 100% and -100%. In all experiments, the total clear fraction plus cloud fraction always equals 100%, but the Double experiment leads to some unphysical radiative fluxes. For example, if a column contains thick high-topped cloud, with all subgrid columns containing cloud, and with OLR less than half of the clear-sky OLR,  $C_{\text{tot}}$  would equal 200%. This means the top of atmosphere flux would equal  $2 \times$  the cloud OLR minus  $1 \times$  the clear-sky OLR, and this scenario would yield negative OLR. In both the explicit and parameterised Double simulations, this occurs in around 3% of grid boxes. Despite this being unphysical, the result is an enhanced radiation-cloud interaction leading to greater longwave heating rates associated with these high-topped clouds, which is the intention of the experiment.

An alternative methodology to alter the magnitude of cloud-radiation interactions that does not result in such unphysical features may be preferential to ours, as it is not immediately clear how the model responds to these features and what their consequences are. For example, a future experiment could modify cloud optical depth by scaling the amount of condensed water seen by the radiation scheme. Greater condensed water content would increase cloud optical depth and enhance cloud-radiation interactions, but would not result in unphysical radiative fluxes. A drawback of this approach is that the sensitivity of the net longwave heating rate to condensed water path is highly dependent on cloud type and condensed water path itself (Figure 3.7). For example, in an experiment where

CWP is doubled in the radiation scheme, the net longwave heating rate would be increased more for thin high cloud compared to thick high cloud. Additionally, the net longwave heating of a column with a typical shallow cloud would be less affected by the increased CWP than a column containing a typical high cloud. Our experiment more fairly scales all cloud-radiative effects, but at the expense of being unphysical.

### 5.3 Response of Cloud to Modified Cloud-Radiation Interactions

The longwave heating rates for a given condensed water path (CWP) for each cloud type in each of the simulations are shown in Figure 5.1 along with each cloud type's CWP probability distribution function. As expected, the High and the High+ cloud types have positive  $LW'$ , and the Shallow cloud type has negative  $LW'$  for the vast majority of the CWPs the clouds typically have. As intended, we find that High and High+ clouds have increasing longwave heating rates for a given CWP as  $C_{\text{tot}}$  increases, meanwhile the longwave heating rates of Shallow clouds becomes more negative. The longwave heating rates remain similar throughout the simulations and are not much affected by aggregation (not shown in this figure), which is consistent with the findings of Chapters 3 and 4.

Comparing explicit and parameterised convection simulations, the longwave heating rates for a given CWP for High and Shallow clouds are broadly similar. One of the key differences is the longwave heating rates of the High+ clouds, which are higher (less negative) for a given CWP in the parameterised convection simulations compared to the explicit simulations, particularly for CWPs greater than  $0.1 \text{ kg m}^{-2}$ . This difference is almost entirely due to the difference in OLR rather than the difference in DLR (not shown). This is discussed later in Section 5.5. The discrepancy in OLR between the parameterised simulations and explicit simulations is roughly an order of magnitude greater than the discrepancy in DLR.

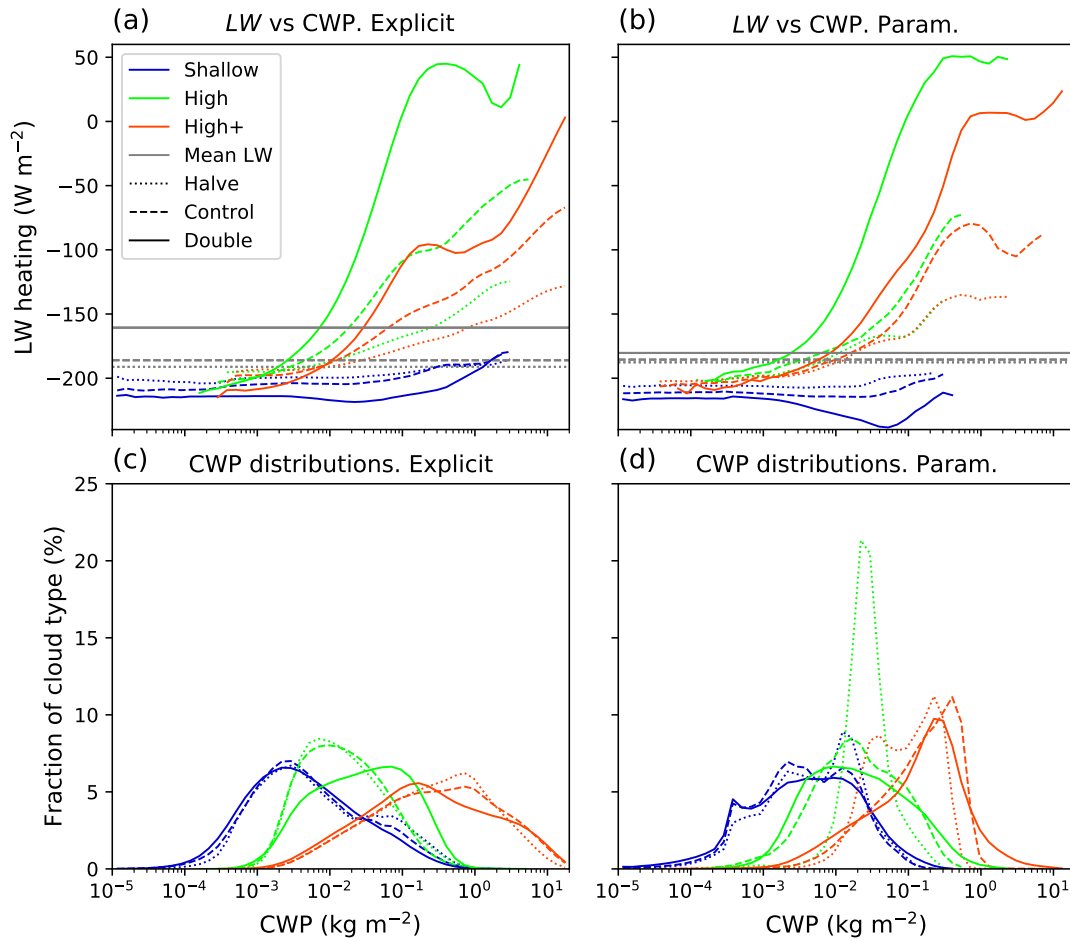


Figure 5.1: (a) longwave heating rate vs CWP throughout the whole of the simulations for Shallow (blue), High (green) and High+ (red) clouds within the explicit convection Halve (dotted), Control (dashed) and Double (solid lines) simulations. Lines are calculated by creating 50 logarithmically-spaced CWP bins and finding the mean LW for each cloud type within the bin. Domain-mean longwave heating rates are represented by horizontal lines. (b) Same as (a) but for the parameterised convection simulations. (c) Probability distribution function of CWP for each cloud type within the explicit convection simulations. (d) Same as (c) but for the parameterised simulations.

On average, High+ clouds have the highest CWP, followed by High cloud and Shallow cloud. This is consistent for all simulations. There are slight changes in the distributions of CWP for each cloud type as  $C_{\text{tot}}$  is modified, which will inevitably impact the longwave heating rate of the clouds, but this impact is small in comparison to the direct effect of  $C_{\text{tot}}$  on the longwave heating rates.

There are a variety of vertical distributions of cloud in our simulations, with the distribution being sensitive to  $C_{\text{tot}}$ , the degree of aggregation, and parameterisation of convection, as seen in Figure 5.2. For the explicit convection simulations during the Growth phase, there is broadly little difference in the mean cloud fraction profile with  $C_{\text{tot}}$ . However, the vertical structure of cloud is more sensitive to  $C_{\text{tot}}$  during the Growth phase in the parameterised convection simulation, with a decrease in fraction of low clouds as  $C_{\text{tot}}$  increases. The distribution of high cloud is similar in the Control and Double simulations, but approximately double for the Halve simulation. This may be because the atmosphere in the cloudy regions on the Halve simulations cool more than they should, yielding greater instability, resulting in more convection. More convective heating is needed to balance the enhanced radiative cooling, which may be the cause of this greater cloud fraction. Note, however, that we do not see a similar large cloud amount in the explicit simulation, highlighting that the cloud response to enhanced radiative cooling is very different between these simulations. During the Mature phase, high cloud fraction increases slightly as  $C_{\text{tot}}$  increases for the explicit simulations but decreases for the parameterised convection simulations. The fraction of mid-level cloud decreases with  $C_{\text{tot}}$  in both sets of simulations, with low cloud fraction decreasing slightly for the explicit, and remaining similar in the parameterised convection simulations.

In all simulations, high cloud fraction decreases with aggregation (going from Growth to Mature), which is consistent with the majority of studies with CRMs, (e.g. Wing and Cronin, 2016) and GCMs (e.g. Bony et al., 2016). We also see a reduction in low cloud with aggregation in each simulation, particularly in the parameterised Control and Double

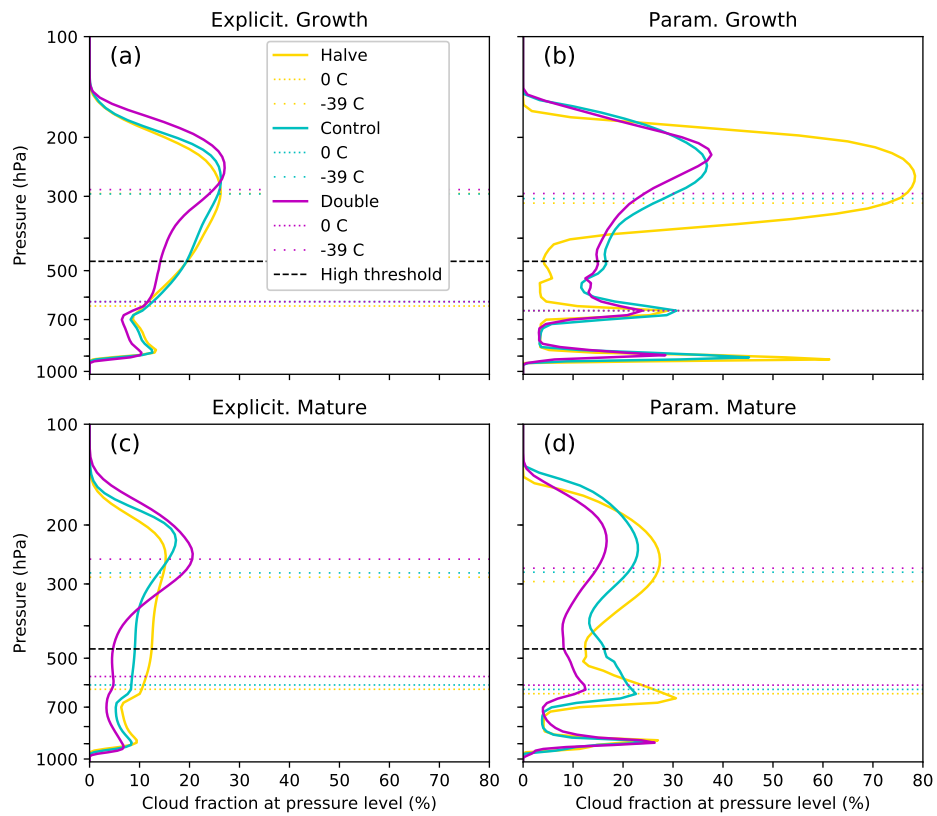


Figure 5.2: Cloud fraction profiles for each of the explicit (a & c) and parameterised simulations (b & d) during the Growth (a & b) and Mature phase (c & d). The high cloud threshold is shown by the black dashed line. The 0°C and -39°C isotherms are represented by dotted lines.

simulations.

The heights of the isotherms in Figure 5.2 are slightly lower in the parameterised simulations, indicating the mean temperature of the troposphere is colder. In addition, the cloud top pressure tends to be slightly lower in the parameterised simulations. Both of these factors would contribute to reduced cloud top emission and an overall greater atmospheric longwave heating rate for high-topped clouds. This may help to explain why the High+ longwave heating rates in Figure 5.1 are higher for a given CWP in the parameterised simulations.

To see how  $C_{\text{tot}}$  affects the vertical profile of the radiative heating rate, Figure 5.3 shows total radiative heating rate profiles as a function of  $\hat{h}$  percentile for each simulation during the Growth and Mature phase. In addition, cloud fraction contours (using a minimum condensed water content of  $10^{-6}$  kg m $^{-3}$  to define a cloud) as a function of  $\hat{h}$  percentile and pressure is overlaid. In all simulations, at all stages of aggregation, there is a greater concentration of deep convective cloud at higher  $\hat{h}$  percentiles. These deep convective clouds are associated with radiative heating throughout the majority of the column, with strong radiative cooling at their cloud tops. By design, the magnitude of these heating rates increases with  $C_{\text{tot}}$ .

The  $\hat{h}$  percentile range of the deep convective regions and anvil cloud are strongly affected by  $C_{\text{tot}}$ . Firstly, during the Growth phase of the explicit simulations, we find little difference in the cloud distribution between the Halve and Control simulations. But we find a larger  $\hat{h}$  percentile range of anvil cloud associated with radiative heating for the explicit Double simulation. An increase in anvil cloud fraction in drier regions with increasing  $C_{\text{tot}}$  is a common feature across both the explicit and parameterised simulations, being particularly notable at higher degrees of aggregation. The presence of high cloud prevents much of the upwelling radiation from lower levels escaping to space, having a warming effect throughout the entire column. The greatest anvil cloud warming may be where the anvil cloud is thick and the upwelling radiation below it is strong. Note in

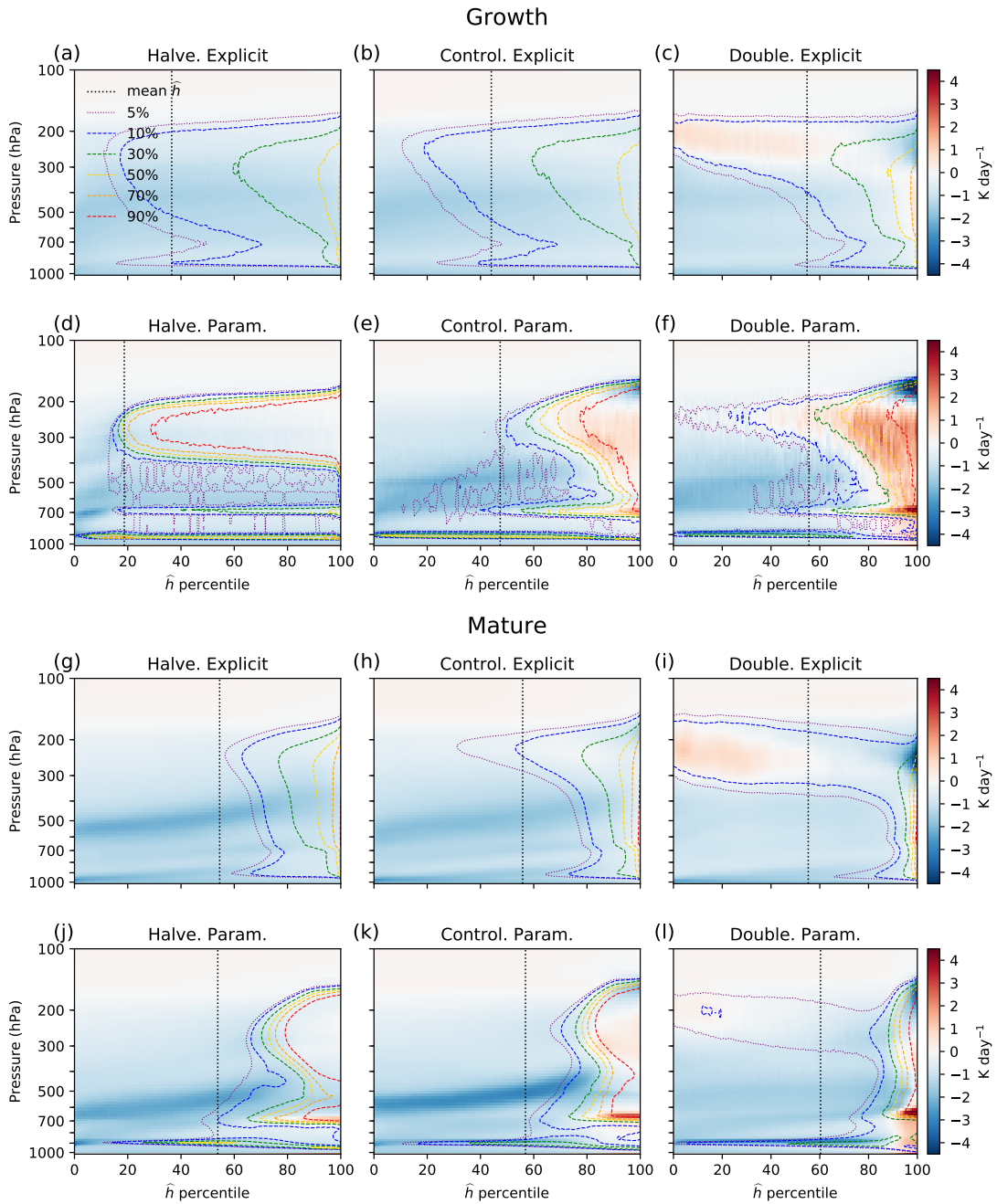


Figure 5.3: Total radiative heating rate profiles vs  $\hat{h}$  percentile, with overlaid cloud fraction contours, for each simulation during the Growth (upper half) and Mature (lower half) phase. Cloud fraction contours indicate the fraction of cloudy grid boxes for a given  $\hat{h}$  percentile and pressure. The domain-mean  $\hat{h}$  is represented by the vertical dotted line.

Figures 5.3c, i and l, the anvil cloud heating is notably stronger in the drier columns where the upwelling emission is coming from a higher effective temperature. It is not immediately apparent what the cause of this extensive high cloud at higher  $C_{\text{tot}}$  is. Perhaps a greater radiatively-driven instability is generated within anvil cloud that is stronger as  $C_{\text{tot}}$  is increased. With larger anvil base heating and cloud top cooling, a circulation may be generated, capable of maintaining high cloud.

There is a greater fraction of high-topped cloud in moist regions in the parameterised simulations at both phases of aggregation, with an associated increase in longwave heating rates throughout the column. The altitude of the convective cloud tops also tends to be higher in parameterised simulations, further enhancing column radiative heating. Additionally, there is a greater fraction of very shallow cloud atop the boundary layer in the parameterised simulations which extends far into the dry regions. These clouds are associated with strong radiative cooling and are not as much of a feature in the explicit simulations, with much of their low-level cloud perhaps being developing cumulus towers. Furthermore, there is a lower fraction of high cloud in the drier regions in the higher  $C_{\text{tot}}$  simulations for the parameterised simulations. All of these effects may help enhance the longwave-FMSE feedback in the parameterised simulations compared to the explicit simulations. This is discussed in more detail in Section 5.5.

The change in cloud fraction with  $C_{\text{tot}}$  may be linked to the amount of convection needed to maintain radiative convective equilibrium (RCE). For simulations in equilibrium, atmospheric radiative cooling is balanced by convective heating via latent heat release and sensible heat transport. This convective heating originates from the surface sensible and latent heat fluxes, meaning the total radiative cooling is balanced by surface heat fluxes. In our simulations, around 94% of the total surface enthalpy flux comes from the latent heat flux. Figure 5.4 shows that the total radiative cooling rate (longwave plus shortwave) tends to be higher as  $C_{\text{tot}}$  decreases. This is primarily due to the reduced ability of high-topped clouds to prevent radiation escaping to space, and may result in a greater

amount of deep convection. The change in radiative cooling with  $C_{\text{tot}}$  is associated with a change in surface heat fluxes and therefore convective heating. However, there is a particularly large discrepancy between radiative cooling and surface fluxes in the Double simulations, especially during the times before the Mature phase. Discrepancies in domain-mean surface fluxes and radiative cooling will result in a nonzero net atmospheric energy balance, meaning the simulations are not in RCE during these times. This highlights that our approach to study the effects of enhanced cloud-radiation interactions on self-aggregation in RCE experiments by adjusting  $C_{\text{tot}}$  is flawed to some extent. For the times at which the simulations are approximately in RCE, both the radiative cooling and convective heating reduce as  $C_{\text{tot}}$  increases.

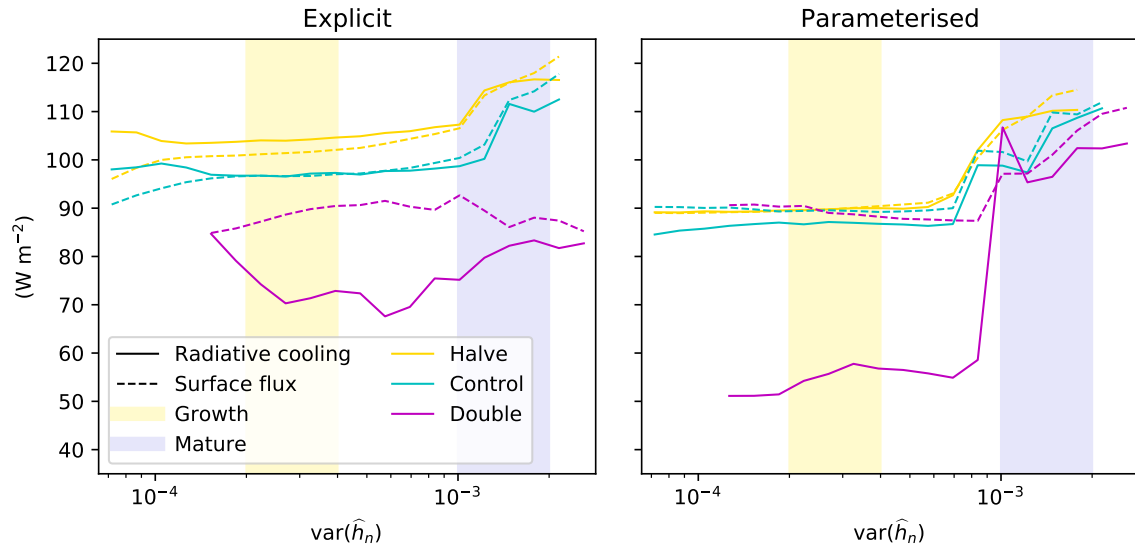


Figure 5.4: Total atmospheric radiative cooling (shortwave plus longwave) (solid lines) and total surface heat flux (latent plus sensible) (dashed lines) for each of the explicit (left) and parameterised (right) simulations, plotted against  $\text{var}(\hat{h}_n)$ .

## 5.4 Self-Aggregation within the Simulations

Convection within each of our simulations is initially randomly distributed throughout the domain. Over the course of tens of days, convection becomes organised into moist and dry regions, eventually forming multiple quasi-stationary moist bands with intense convection separated by dry, subsiding regions. Figure 5.5 shows Hovmöller plots for each simulation, with  $\widehat{h}'_n$  being averaged along the short axis of the domain. Positive  $\widehat{h}'_n$  is associated with moist convective regions and negative  $\widehat{h}'_n$  is associated with dry subsiding regions. From this figure, we can see that moist and dry regions amplify faster as  $C_{\text{tot}}$  increases. We also find the length scale of organisation to be greater with  $C_{\text{tot}}$  once the convective organisation reaches equilibrium. The length scale of organisation is also greater in the parameterised convection simulations for a given  $C_{\text{tot}}$ .

The time series of  $\text{var}(\widehat{h}_n)$  is shown in Figure 5.6a & b for each of our simulations. As implied in Figure 5.5, the convection aggregates faster as  $C_{\text{tot}}$  increases in both the explicit and parameterised convection simulations via the  $\text{var}(\widehat{h}_n)$  metric. There is little difference in the final degree of aggregation in both sets of simulations via this metric. The  $e$ -folding of the autocorrelation function of  $\widehat{h}_n$  ( $L_{\text{cor}}$ ) is used as a measure of the length scale of organisation and the time series of this is shown in Figure 5.6c & d. We find the length scale of aggregation is not perfectly correlated with  $\text{var}(\widehat{h}_n)$ , continuing to increase for a time even once  $\text{var}(\widehat{h}_n)$  first reaches equilibrium for the Control and Double simulations in particular.

The variance of  $\widehat{h}_n$  increases with aggregation because positive and negative anomalies in  $\widehat{h}_n$  tend to amplify as aggregation increases. To see how the amplification of  $\widehat{h}_n$  anomalies are affected by  $C_{\text{tot}}$  and parameterisation, the evolution of the probability distribution function of  $\widehat{h}_n$  for each simulation is shown in Figure 5.7. In both the explicit and parameterised simulations, we find the moist regions amplify faster as we increase  $C_{\text{tot}}$ . This is expected because moist regions are favourable for deep convection, producing high-topped

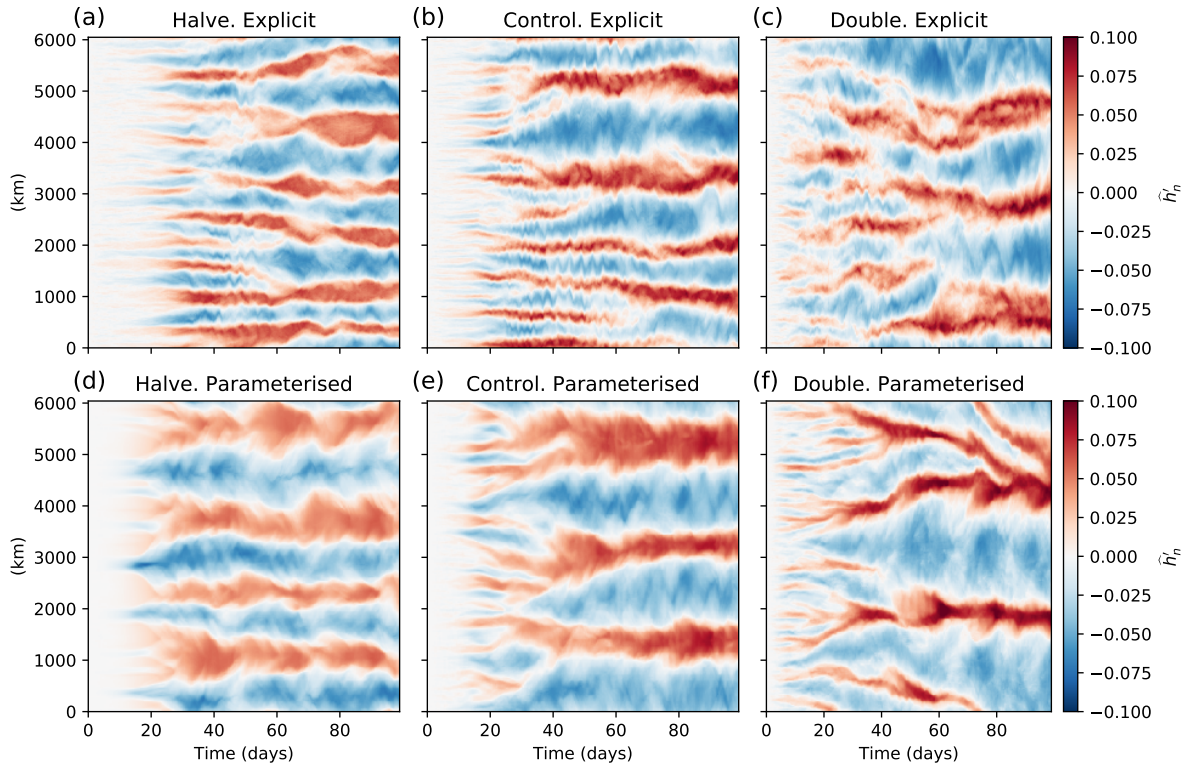


Figure 5.5: Hovmöller diagrams of  $\widehat{h}'_n$  for each simulation.  $\widehat{h}'_n$  is averaged across the short axis of the domain. Explicit convection simulations are on the top row and parameterised simulations on the bottom.  $C_{\text{tot}}$  increases left to right.

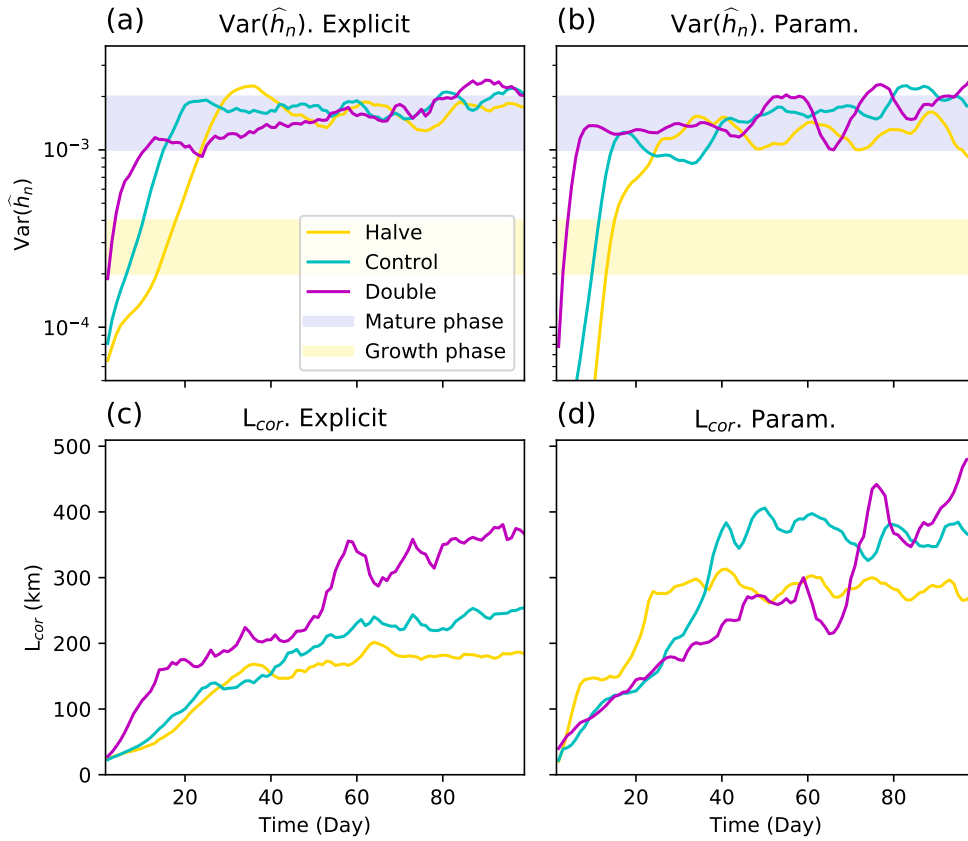


Figure 5.6: Time series of  $\text{var}(\hat{h}_n)$  (solid lines) and  $L_{cor}$  (dashed lines) for the Halve, Control and Double simulations of the (a) explicit convection simulations (after smoothing) and (b) parameterised convection simulations. Also indicated by the shaded regions are the  $\text{var}(\hat{h}_n)$  ranges of the Growth and Mature phases.

clouds which have strong positive longwave heating anomalies. Increased longwave heating anomalies in moist regions further heats moist regions, making them more favourable for deep convection. We find a greater concentration of grid cells in the very highest  $\widehat{h}'_n$  regions for the lower  $C_{\text{tot}}$  simulations, which may be a result of reduced noise in  $\widehat{h}'_n$  in moist regions due to the reduced influence of cloud-longwave interactions. In the Halve simulations, the most negative  $\widehat{h}'_n$  regions amplify faster than the most positive  $\widehat{h}'_n$  regions, but as  $C_{\text{tot}}$  increases, the rate of negative  $\widehat{h}'_n$  amplification appears to increase. However, this may be a result of the moist regions amplifying faster at higher  $C_{\text{tot}}$ , making the dry regions more anomalously negative at a faster rate.

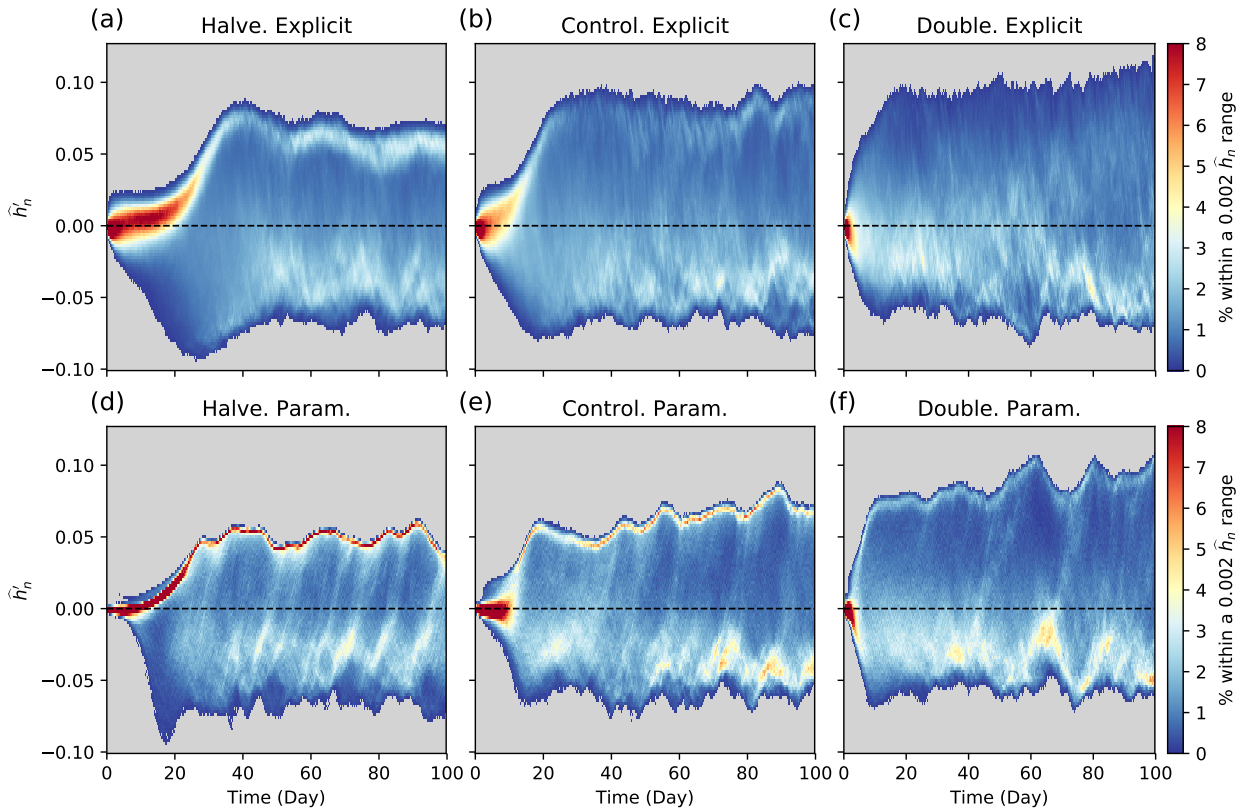


Figure 5.7: Time series of  $\widehat{h}'_n$  PDFs for each simulation. The instantaneous domain-mean  $\widehat{h}'_n$  is represented by the dashed line.

To see which feedbacks contribute to the rate of change of aggregation, and how these

feedbacks are affected by  $C_{\text{tot}}$  and parameterisation, the  $\text{var}(\hat{h}_n)$  budget terms in Equation (2.2) are plotted against  $\text{var}(\hat{h}_n)$  in Figure 5.8. For the majority of  $\text{var}(\hat{h}_n)$  lower than the Mature phase, the rate of aggregation increases as  $C_{\text{tot}}$  is increased. This is consistent in both the explicit and parameterised simulations. The aggregation rate is typically faster in the parameterised simulations for a given  $C_{\text{tot}}$ .

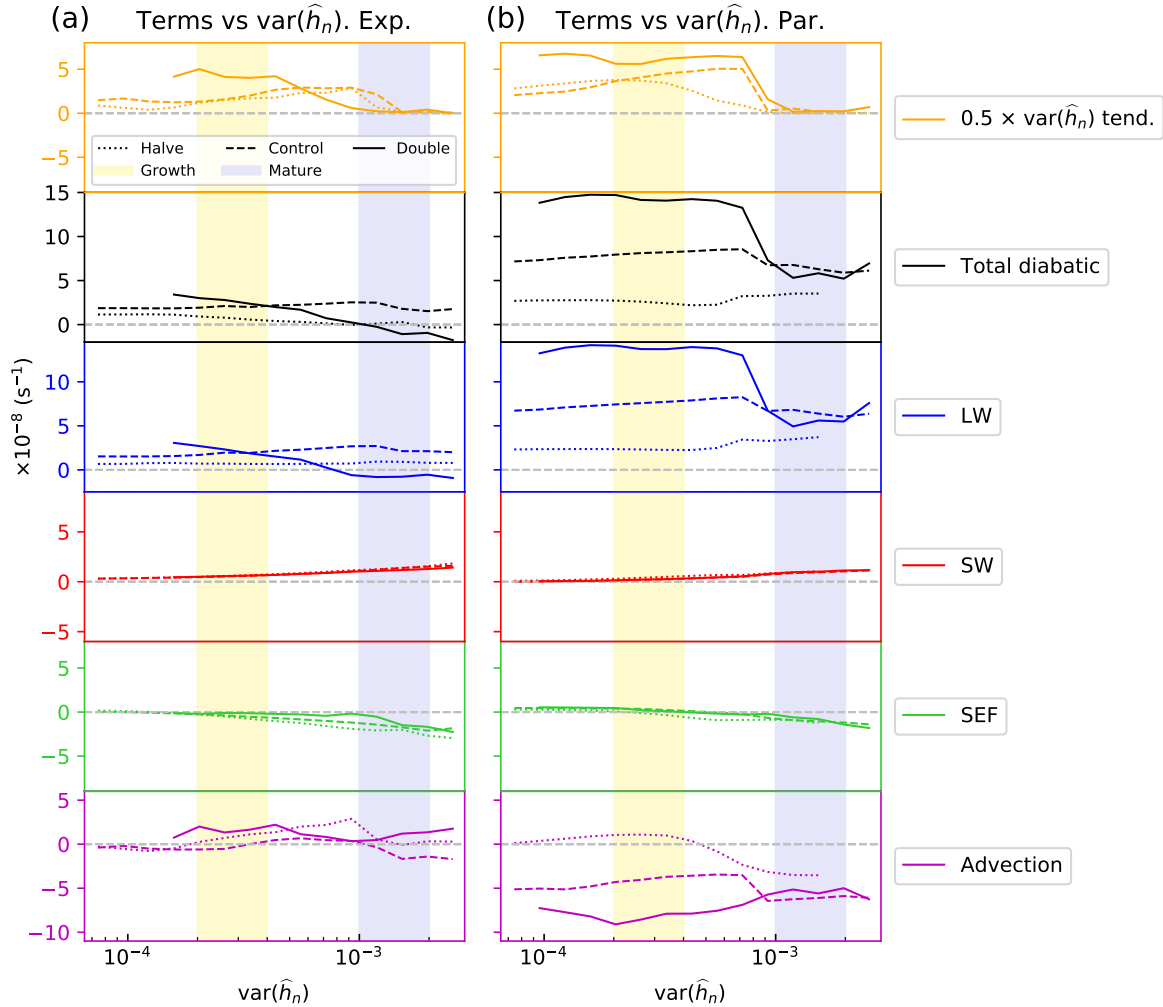


Figure 5.8: Terms in Equation (2.2) divided by the standard deviation of  $\hat{h}_n$  plotted against  $\text{var}(\hat{h}_n)$  for the (a) explicit and (b) parameterised simulations.

The rate of change of aggregation via the  $\text{var}(\hat{h}_n)$  metric is equal to the sum of the

diabatic terms plus the advection term. Firstly, the dependence of the shortwave term on  $\text{var}(\widehat{h}_n)$  is similar in all of our simulations. This is an expected result since it is shown by Wing and Emanuel (2014) and in Chapter 3 that the majority of the shortwave term can be explained by shortwave absorption by water vapour, with the absorbing affect of cloud having a small effect in comparison. The variability of  $\widehat{h}$  is dominated by the variability of vertically-integrated water vapour, so the relationship between the shortwave term and the  $\text{var}(\widehat{h}_n)$  should be consistent between simulations at the same temperature. This is verified in Chapter 4 with the shortwave term having the smallest inter-model variability for a given  $\text{var}(\widehat{h}_n)$  regardless of parameterisation.

The surface flux term is typically negative or close to zero during the early stages of aggregation which is consistent with the results in Chapter 3, but anomalously negative compared to the majority of simulations in Chapter 4. The surface flux term becomes increasingly negative as the convection becomes more aggregated. This is consistent with the findings in the previous chapters and consistent with the enhanced (negative) air-sea disequilibrium feedback as aggregation increases, as described by Wing and Emanuel (2014). In each of these simulations, the shortwave and surface flux terms approximately cancel each other, meaning that the total diabatic feedback is approximately equal to the longwave term.

The sensitivity of the longwave term to  $C_{\text{tot}}$  is more complicated than initially anticipated from the experiment design. We had expected the longwave term to increase with  $C_{\text{tot}}$  at all stages of aggregation due to an enhanced positive feedback between high-topped, deep convective cloud in moist regions leading to further anomalous heating and further deep convection. Our simulations do display an increase in the longwave term as  $C_{\text{tot}}$  increases, but only during the very early stages of aggregation in the explicit simulations, and up until the Mature phase of the parameterised simulations. The longwave feedback of the Double simulations becomes increasingly negative as aggregation develops and there is no consistent trend with  $C_{\text{tot}}$  after the convection becomes more aggregated. In the

explicit Double simulation, the longwave term becomes negative and the total diabatic-FMSE feedback turns negative in the Mature phase. However, the convection does not disaggregate because the advection term remains positive for this simulation.

The differences in the budget terms between the Halve and Control simulations were anticipated following the results of the previous chapters. The Control simulations have a higher longwave feedback than the Halve simulations at all stages of aggregation, resulting in the total diabatic term being higher in the Control simulations. The advection feedback is more negative, but the aggregation rate is faster. These outcomes are anticipated following the results in Chapter 4; in particular for the parameterised simulations, where the models with a stronger longwave feedback aggregate faster despite a more negative advection feedback. For simulations with a higher diabatic feedback, the advection feedback is expected to be more negative. The increased diabatic feedback has a greater tendency to amplify moist and dry regions, so the circulations that act to dampen aggregation will be acting across larger gradients of FMSE, and so the advection feedback becomes more negative.

It was unclear from Chapter 4 whether the enhanced longwave feedback would result in faster aggregation for the explicit convection simulations because the magnitude of the (negative) advection term was found to be proportional to the diabatic feedback in the explicit aggregation rates on average, with the longwave feedback having no correlation with aggregation rate. We find a higher diabatic feedback is associated with faster aggregation in the explicit simulations in this chapter, but it is not associated with an increasingly negative advection feedback, with the Double simulation often having the most positive advection feedback. This suggests that  $C_{\text{tot}}$ , and hence the cloud-longwave forcing, has a strong influence on radiatively-driven circulations that may favour aggregation, and these play a key role in the aggregation rate of explicit simulations.

The longwave feedback is greater in the parameterised simulations for all  $C_{\text{tot}}$ , which is consistent with the findings of Chapter 4. This results in a faster aggregation rate for a

given  $\text{var}(\widehat{h}_n)$  compared to the explicit simulations. In the parameterised simulations, the change in the magnitude of the advection feedback with  $C_{\text{tot}}$  is correlated with the total diabatic term, however the rate of aggregation remains most strongly correlated with the total diabatic feedback, which in turn is most influenced by the longwave feedback in our simulations.

The parameterised convection Halve simulation is most similar to the explicit Control simulation in terms of the magnitude of the longwave feedback, total diabatic feedback, advection feedback and aggregation rate for a given  $\text{var}(\widehat{h}_n)$ . It is also the most similar parameterised simulation in terms of the domain-mean radiative cooling rate and surface flux (Figure 5.4) and length scale of aggregation (Figures 5.5 & 5.6). This suggests that decreasing the cloud-longwave forcing in parameterised convection simulations may allow aggregation in parameterised simulations to behave more similarly to explicit convection simulations. However, there remains significant discrepancies in the distribution of cloud between these two simulations (Figures 5.2 & 5.3).

We have seen that for both the explicit and parameterised convection simulations, aggregation via the  $\text{var}(\widehat{h}_n)$  metric increases with  $C_{\text{tot}}$ , and that the rate of aggregation for a given  $C_{\text{tot}}$  and  $\text{var}(\widehat{h}_n)$  is greater in the parameterised simulations. This is mainly a result of the response of the longwave feedback to  $C_{\text{tot}}$  and parameterisation of convection, being greater in the parameterised simulations and increasing with  $C_{\text{tot}}$ . We explore the factors controlling the longwave feedback for each simulation at both stages of aggregation in the following section.

## 5.5 Influence of Enhanced Cloud-Radiation Interactions on the Longwave-FMSE Feedback

The longwave term in Equation 2.2 is the domain-mean covariance between longwave heating anomalies and  $\widehat{h}_n$  anomalies. This is equal to the integral of the  $LW' \times \widehat{h}'_n$

covariance multiplied by the probability distribution function (PDF) of the covariance. The integral can be separated into four covariance “quadrants”. These are the regions with both positive  $LW'$  &  $\widehat{h}'_n$  (positive contribution), positive  $LW'$  & negative  $\widehat{h}'_n$  (negative contribution), negative  $LW'$  & positive  $\widehat{h}'_n$  (negative contribution), and both negative  $LW'$  &  $\widehat{h}'_n$  (positive contribution).

The distribution of the  $LW' \times \widehat{h}'_n$  covariance multiplied by the PDF of the covariance is shown in Figure 5.9 for each simulation during the Growth phase and during the Mature phase. This figure gives an understanding as to which regions are contributing to the longwave term, and how this is sensitive to aggregation,  $C_{\text{tot}}$  and parameterisation of convection. Note that the values displaying the contributions to the domain-mean covariance are not divided by the standard deviation of  $\widehat{h}'_n$  as was the case in Figure 5.8.

During the Growth phase, we find the contributions from the positive covariance quadrants are large in comparison to the negative quadrants in all simulations. This means anomalously dry regions tend to have anomalously negative  $LW'$  and anomalously moist regions tend to have positive  $LW'$ . The total longwave term increases with  $C_{\text{tot}}$  for both explicit and parameterised convection. This is because the magnitude of the positive longwave anomalies increases as  $C_{\text{tot}}$  increases (as expected). There is a stronger correlation between  $\widehat{h}'_n$  and  $LW'$  in the parameterised convection simulations than the explicit simulations, resulting in a greater total longwave feedback.

The range of  $\widehat{h}'_n$  is higher in the Mature phase compared to the Growth phase since the magnitude of  $\widehat{h}'_n$  anomalies is greater. This increases the magnitude of the covariance quadrant contributions and domain-mean covariance. As with the Growth phase, the correlation between  $\widehat{h}'_n$  and  $LW'$  remains stronger in the parameterised simulations. The dependence with  $C_{\text{tot}}$  is less straightforward. From the Halve to Control simulations, the longwave term increases as the longwave anomalies amplify. In both the explicit and parameterised simulations, the Double simulation develops a significant amount of negative  $\widehat{h}'_n$  regions with strongly positive  $LW'$ . In addition, there is a reduced amount of positive

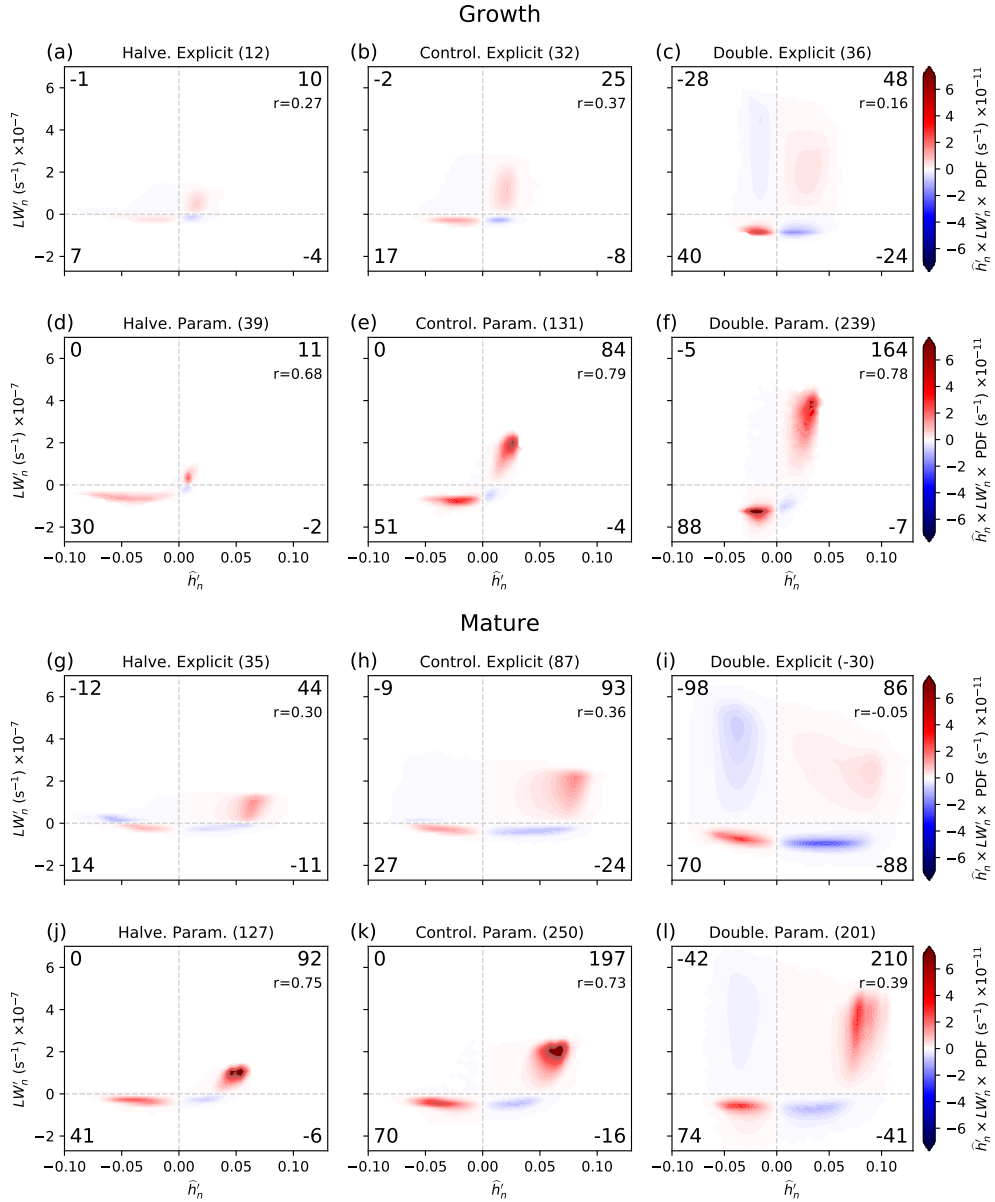


Figure 5.9: Distributions of the  $LW'_n \times \widehat{h}'_n$  covariance for each simulation during the Growth (upper half) and Mature phase (lower half). The strength of the colours represents the magnitude of the  $LW'_n \times \widehat{h}'_n$  covariance multiplied by its probability distribution function. The probability distribution function is calculated from a  $50 \times 50$  2-dimensional histogram of density using the  $x$  and  $y$  limits shown in the figures as the histogram boundaries. Values in the subplot corners show the contribution to the domain-mean  $LW'_n \times \widehat{h}'_n$  covariance of each covariance quadrant. The values in the plot titles show the domain-mean  $LW'_n \times \widehat{h}'_n$  covariance (multiplied by  $10^{11}$ ). The correlation coefficient ( $r$ ) between  $\widehat{h}'_n$  and  $LW'$  is also shown.

$\widehat{h}'_n$  regions with positive  $LW'$ . These factors reduce the correlation between  $\widehat{h}'_n$  and  $LW'$ , resulting in a sharp decrease in the total longwave term for the Double simulations.

To help explain how the longwave anomalies are affected by  $C_{\text{tot}}$ , parameterisation and aggregation, we show the distributions of cloud type  $LW$  for each simulation at both stages of aggregation in Figure 5.10. Firstly, as  $C_{\text{tot}}$  increases, the range of cloud  $LW$  increases. The  $LW$  of the High and High+ cloud types tends to become more positive and the Shallow cloud type becomes more negative. This is true for both the parameterised and explicit simulations and regardless of the degree of aggregation.  $C_{\text{tot}}$  does not affect the Clear longwave heating rates, so the longwave distribution for the Clear regions remains similar regardless of  $C_{\text{tot}}$ . The Clear distribution is also similar regardless of parameterisation and aggregation. The peak of the Clear distribution may change amplitude, but this is due to the change in the total Clear fraction.

The High and High+  $LW$  increases with  $C_{\text{tot}}$ , resulting in the domain mean  $LW$  increasing by up to a few tens of  $\text{W m}^{-2}$ . The main consequence of this is the Clear and Shallow regions become more anomalously negative. This makes the negative  $LW'$  covariance quadrants (shown in Figure 5.9) have a greater contribution to the total longwave feedback as  $C_{\text{tot}}$  increases.

The most significant difference between the explicit and parameterised simulations is the  $LW$  distribution of the High+ clouds in both the Growth and Mature phases. The parameterised simulations tend to have a larger amount of High+ cloud with greater  $LW$ . In Chapter 4, it was found that the mean high-topped cloud's  $LW$  remained similar between the Smoothed explicit convection simulations and parameterised simulations during the Growth phase, but was higher for the parameterised simulations in the Mature phase. However, the longwave *anomalies* were consistently higher in the parameterised simulations, which is what we find in our simulations here. Therefore, the change in the aggregating influence of longwave heating rates between the explicit and parameterised simulations are consistent in this chapter and Chapter 4.

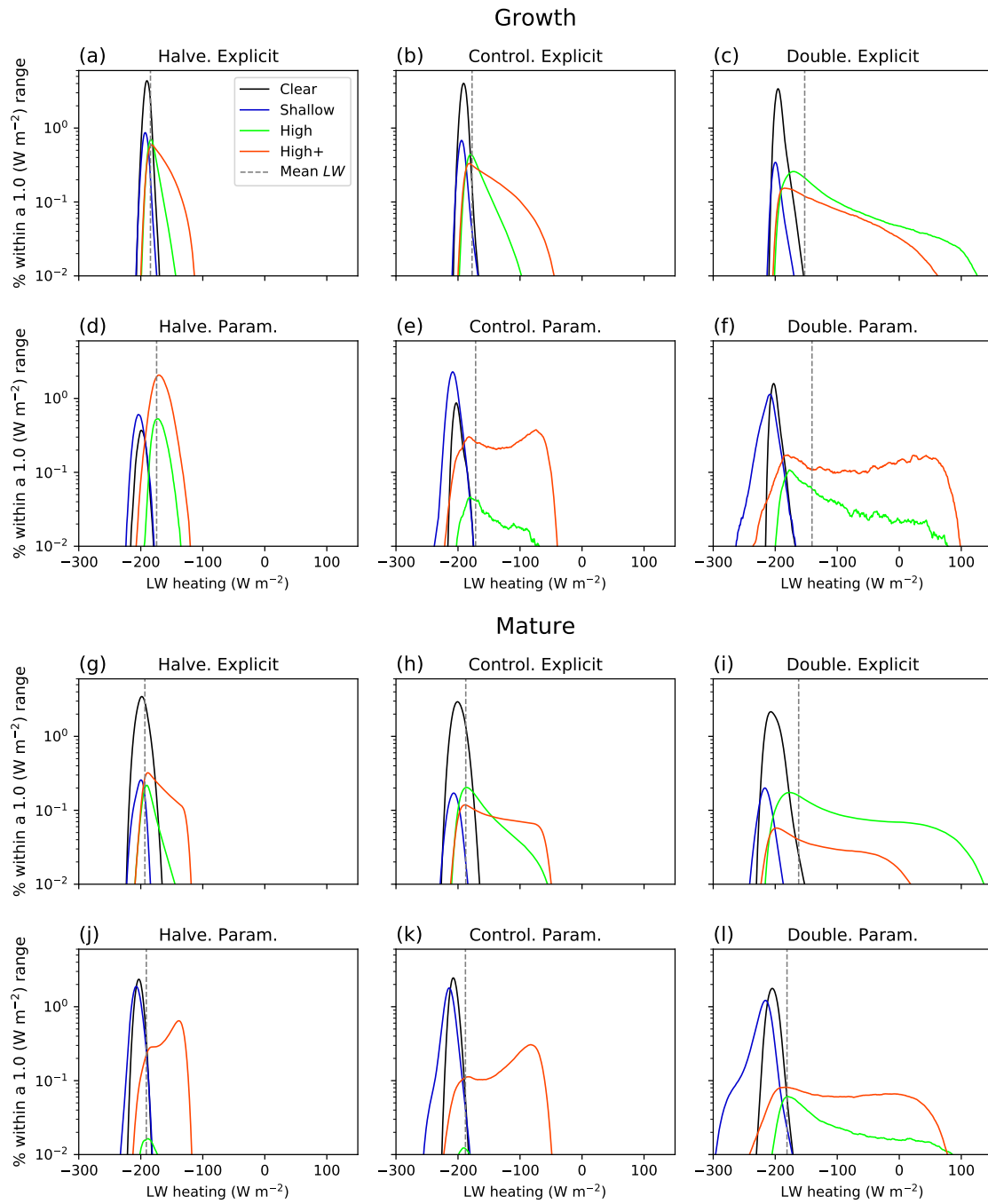


Figure 5.10: Domain fraction of each cloud type within a  $1 \text{ W m}^{-2}$  bin of longwave heating during the Growth (upper half) and Mature phase (lower half) of each simulation. The domain mean longwave heating rate is represented by the vertical dashed line.

To explain the sensitivity of  $\widehat{h}'_n$  to  $C_{\text{tot}}$ , parameterisation, and aggregation, we show each cloud type's  $\widehat{h}'_n$  distribution in Figure 5.11. Together with Figure 5.10, we can gain a deeper understanding of what influences the longwave-FMSE feedback.

During the Growth phase, there is a shift from a negatively skewed  $\widehat{h}'_n$  distribution for the Halve simulations, to a more normal distribution in the Control simulations, and then to a more positively skewed and Double simulations (not explicitly shown). The cloud types that occur in the negative  $\widehat{h}'_n$  regions tend to also have negative  $LW'$  in the Halve simulations, meaning the negative  $\widehat{h}'_n$  anomalies are able to amplify faster than the positive  $\widehat{h}'_n$ . This helps to explain why the dry regions amplify faster than the moist regions for the Halve simulations in Figure 5.7, but the moist and dry regions amplify at a similar rate to each other in the Control and Double simulations. Despite the amplification of the dry regions in the Halve simulations being faster than the amplification of the moist regions, it is still slower than the amplification of anomalously dry regions in the Control and Double simulations. As previously discussed, this is in part due to the increased rate of amplification of the moist regions making the dry regions more anomalously negative. However, Figure 5.10a - f shows the Clear and Shallow clouds have a far less anomalous  $LW'$  in the Halve simulations, thus further reducing their amplifying effect on negative  $\widehat{h}'_n$ .

As  $C_{\text{tot}}$  increases, we find the  $\widehat{h}'_n$  distribution of High cloud becomes increasingly negative in the Growth phase and particularly for the Mature phase. This increases the magnitude of the (negative) contribution from the negative  $\widehat{h}'_n$  & positive  $LW'$  quadrant, significantly reducing the magnitude of the longwave term particularly during the Mature phase.

Figure 5.9 showed that the parameterised simulations had a much smaller negative contribution from the negative covariance quadrants compared to the explicit simulations at both stages of aggregation. We can see from Figure 5.11 that there is a greater amount of High and High+ cloud types occurring in positive  $\widehat{h}'_n$  regions, and that the Clear and

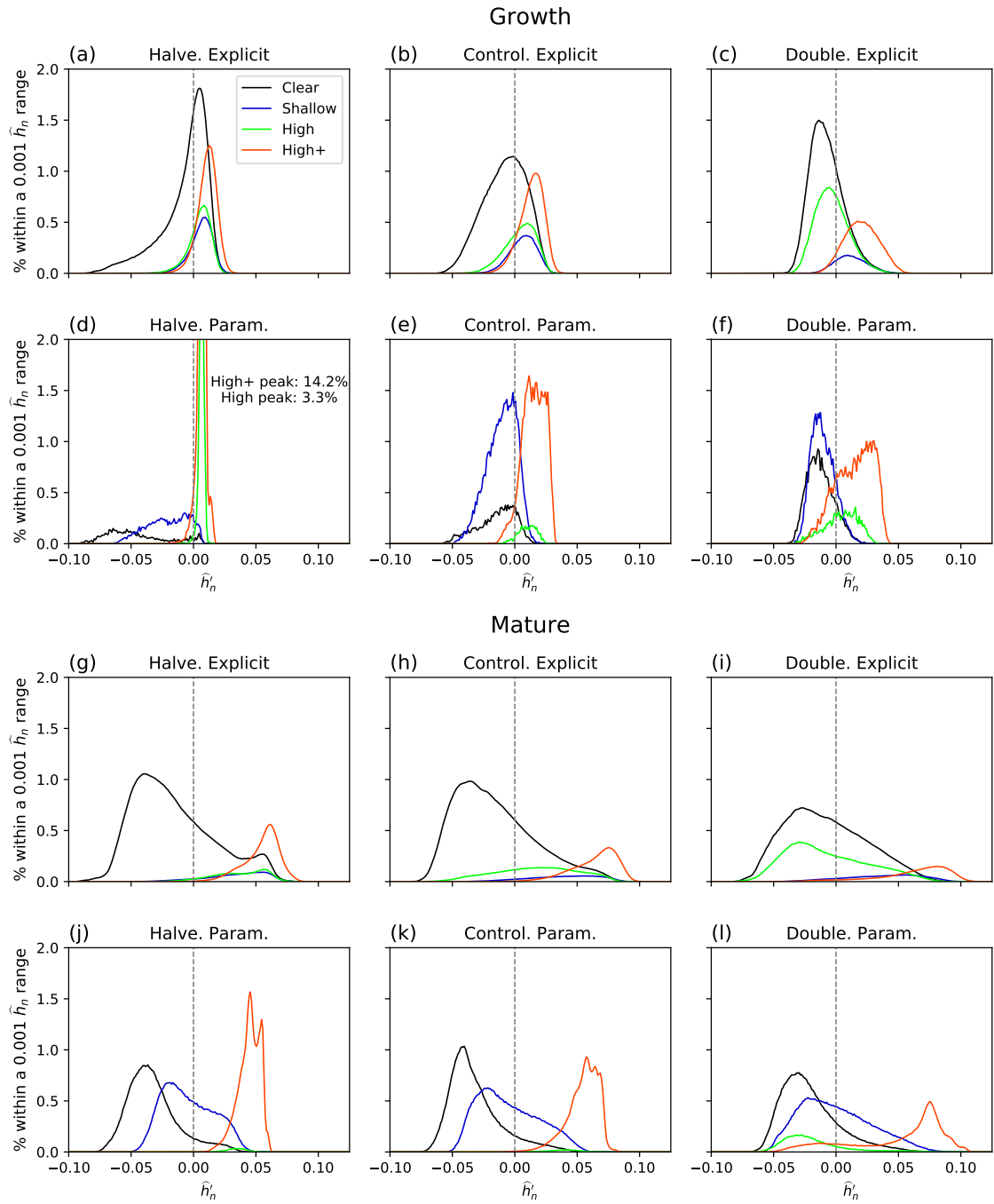


Figure 5.11: Domain fraction of each cloud type within a 0.001 bin of  $\hat{h}_n$  during the Growth (upper half) and Mature phase (lower half) of each simulation.

Low cloud types are typically confined to more negative  $\widehat{h}'_n$  regions in the parameterised simulations. Because of this, there is a stronger correlation between  $\widehat{h}'_n$  and  $LW'$ , hence an enhanced longwave feedback.

The total contributions of each cloud type to the longwave feedback for each simulation during the Growth and Mature phases of aggregation are quantified in Figure 5.12a. During the Growth phase, the total longwave term increases with  $C_{\text{tot}}$  (though for the explicit simulations, the increase from Control to Double is very small). It is also much larger in the parameterised convection simulations than the explicit simulations. In the Mature phase, the total longwave term increases from the Halve to the Control simulations, but decreases from the Control to the Double simulations. These features can be explained by analysing the contribution of each cloud type to the longwave term.

For the explicit simulations during the Growth phase, contributions from the Clear and High+ regions dominate the longwave term, with their contributions increasing as  $C_{\text{tot}}$  increases (Figure 5.12a). Clear regions have a positive  $LW' \times \widehat{h}'_n$  covariance (Figure 5.12b) and they are more abundant than any other cloud type (Figure 5.12c), so they have a significant contribution to the longwave term. Their covariance increases with  $C_{\text{tot}}$  as their  $LW'$  becomes anomalously more negative compared to the increasingly positive  $LW'$  of the High and High+ clouds (Figure 5.12d). The High+ regions have a significant contribution to the longwave term because they occupy around a fifth to a quarter of the domain and have the highest  $LW' \times \widehat{h}'_n$  covariance out of all cloud types. As  $C_{\text{tot}}$  increases, their  $LW'$  and  $LW' \times \widehat{h}'_n$  covariance increases, hence their contribution increases.

For the parameterised simulations during the Growth phase, the contribution of each cloud type to the longwave term is greater than in the explicit simulations. The High+ cloud has the largest contribution within the Control and Double simulations, with contributions from Clear and Low cloud having a significant contribution particularly at lower  $C_{\text{tot}}$ . The contributions from the High+ cloud are greater in the parameterised simulations which is mainly due to the increase in  $LW$  (Figure 5.12f). This increase in  $LW$  is in part

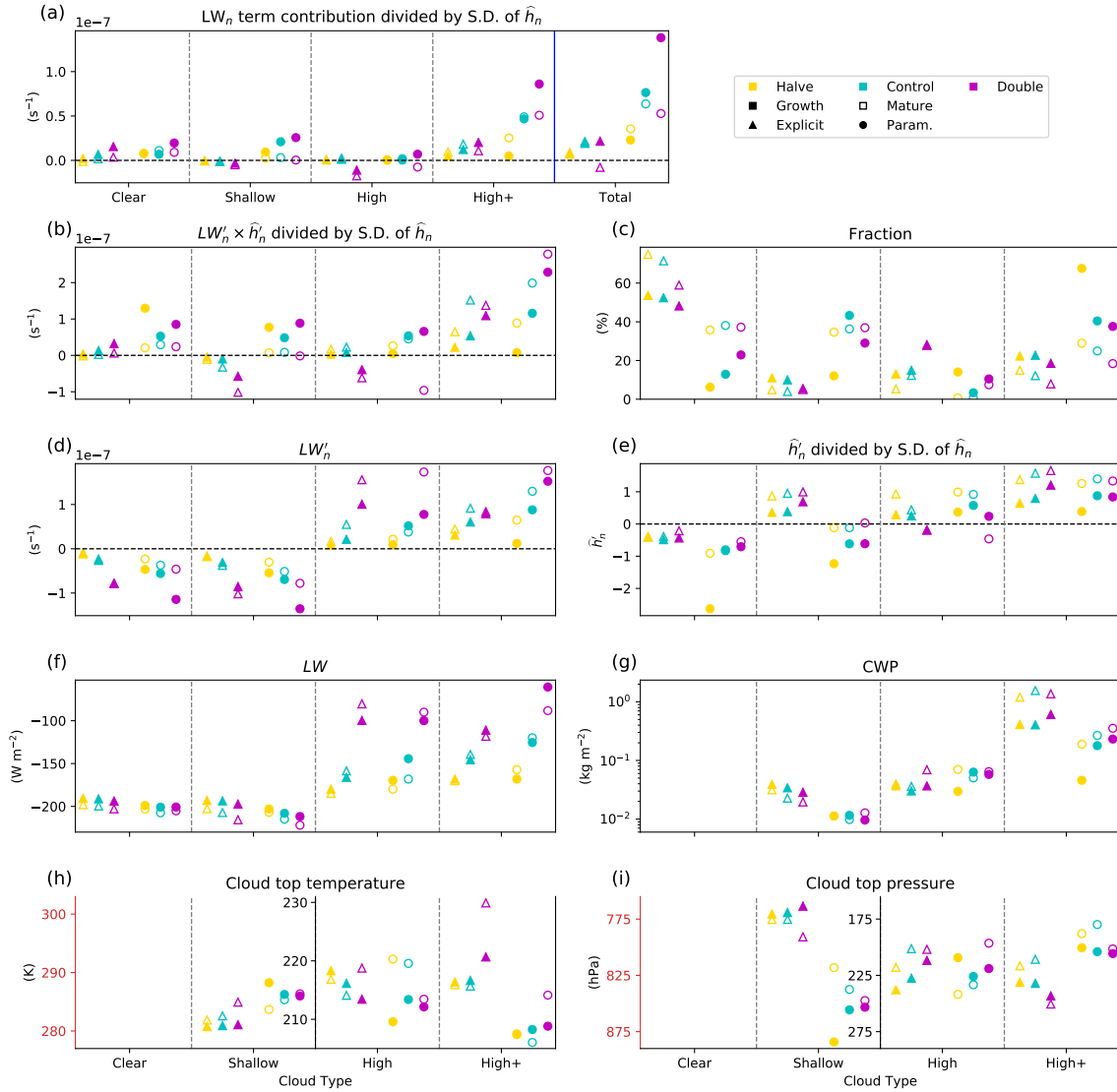


Figure 5.12: Mean (a) contribution to the longwave term in Equation (2.2) divided by the standard deviation of  $\hat{h}_n$ , (b) normalised longwave  $\times$  FMSE covariance divided by the standard deviation of  $\hat{h}_n$ , (c) cloud fraction, (d) normalised longwave heating anomaly, (e) normalised FMSE anomaly divided by the standard deviation of  $\hat{h}_n$ , (f) longwave heating rate, (g) condensed water path, (h) cloud top temperature, and (i) cloud top pressure for the Growth (filled points) and Mature phase (open points) of the explicit (triangles) and parameterised simulations (circles). Data points for each category are in order of  $C_{tot}$  increasing to the right. Note that the High and High+ clouds are plotted on a separate  $y$ -axis in panels (h) and (i).

due to the lower cloud top temperature of these clouds in the parameterised simulations (Figure 5.12h) thanks to their higher cloud tops (Figure 5.12i) as well as their colder over-all temperatures at a given pressure (Figure 5.2), despite their CWP being typically lower (Figure 5.12g). These High+ clouds are also more abundant in the parameterised simulations, which is the main reason for the greater High+ contribution in the parameterised simulation for the Halve experiment. Unlike in the explicit simulations, Shallow clouds have a significant contribution to the longwave term in the parameterised simulations. They have a much greater fraction, particularly in the Control and Double simulations, and they have a positive  $LW' \times \widehat{h}'_n$  covariance thanks to their typically-negative  $\widehat{h}'_n$  (unlike in the explicit simulations).

The longwave term remains similar from the Growth to Mature phase for the Halve and Control simulations, which is consistent with the finding in Chapter 4 for the 300 K SST. However, the longwave term significantly decreases with aggregation for the Double simulations. This is a result of increasingly negative contributions from every cloud type to the total longwave term and is consistent in both the parameterised and explicit simulations.

The decrease in the contribution of High+ clouds with aggregation is linked with the decrease in High+ cloud fraction since their  $LW' \times \widehat{h}'_n$  covariance increases slightly. High (but not High+) clouds have a more negative contribution because of the increasingly negative  $LW' \times \widehat{h}'_n$  covariance. The magnitude of the covariance increases as their  $LW'$  increases, which is a combination of their  $LW$  increasing (due to increased CWP and slightly lower cloud top pressure and thus temperature) and the reduction in high-topped cloud amount making them more anomalously positive. Their  $\widehat{h}'_n$  is also increasingly negative with aggregation, making their covariance negative. The Shallow cloud's average  $LW' \times \widehat{h}'_n$  covariance becomes increasingly negative with aggregation. Their  $LW'$  is negative, yet they tend to occur in increasingly positive  $\widehat{h}'_n$ . This lowers their contribution to the longwave term. Finally, the decreased contribution of the Clear regions comes from

their reduced average  $LW' \times \widehat{h}'_n$  covariance. This is in part due to less negative  $LW'$  in the parameterised simulation. With the reduction in high-topped cloud fraction with aggregation, the Clear  $LW'$  becomes less anomalously negative. The mean  $\widehat{h}'_n$  also becomes increasingly positive in both the explicit and parameterised simulations as there is a higher fraction of Clear regions in anomalously high  $\widehat{h}'_n$  (Figure 5.11).

## 5.6 Conclusions

In our previous chapters, we find that longwave-FMSE interactions are crucial drivers and maintainers of aggregation within RCEMIP models, often being the strongest diabatic-FMSE feedback throughout the simulations. We find a wide range in the magnitude of these diabatic feedbacks amongst the models, as well as a wide range in the degree and rate of aggregation. Whilst there is a link between the magnitude of the diabatic-FMSE feedbacks and aggregation rate in GCMs, there is no such correlation in the CRMs.

In this chapter, we investigate how the longwave-FMSE feedback affects the rate of aggregation in explicit and parameterised convection simulations by systematically scaling the strength of cloud-longwave radiation interactions in the model. This is achieved by altering the parameter that determines the fraction of cloudy subcolumns within a given grid box seen by the longwave radiation scheme ( $C_{\text{tot}}$ ). We run two sets of simulations: a set of three explicit convection simulations with a 3 km horizontal grid spacing and a set of three parameterised convection simulations with a 20 km grid spacing. All simulations are non-rotating, approximately 6,000 km  $\times$  400km in size with doubly periodic boundary conditions, constant solar forcing, and with a fixed SST of 300 K. Both sets of simulations have a Control simulation in which  $C_{\text{tot}}$  is not adjusted. We then have a Halve and a Double  $C_{\text{tot}}$  simulation designed to reduce and increase the magnitude of cloud-longwave interactions respectively.

We use the same variance of normalised vertically-integrated FMSE ( $\text{var}(\widehat{h}_n)$ ) frame-

work as described in Section 2.3 to measure aggregation and quantify the contribution of different FMSE feedbacks to the rate of change of aggregation. A cloud classification scheme is used to define a cloud type at every grid point, defining four different cloud types based on the vertical profile of condensed water: Clear (negligible condensed water in the profile), Shallow (cloud in the lower troposphere only), High (cloud in the upper troposphere only), and High+ (cloud in both the upper and lower troposphere). Differences in the longwave-FMSE feedback between our simulations can then be studied by comparing these cloud types' contribution to the total longwave feedback. We define a “Growth” and “Mature” phase of aggregation using fixed ranges of  $\text{var}(\hat{h}_n)$  for which convection is rapidly aggregating and in approximate equilibrium respectively.

We only analyse the explicit simulations after horizontally smoothing them, so that every grid point is the average of the  $7 \times 7$  grid points surrounding it (accounting for the doubly-periodic boundary conditions). This is because the parameterised simulations have an approximately 7 times greater grid spacing. In smoothing the explicit simulations, we can use the  $\text{var}(\hat{h}_n)$  budget framework to compare the two sets of simulations fairly, without the resolution dependence of the framework directly affecting the results.

In adjusting the cloud-longwave interactions, the interactions between FMSE and both shortwave and surface fluxes remain similar. Therefore, the differences in the total diabatic-FMSE feedbacks in our simulations are due to the alteration of  $C_{\text{tot}}$  and representation of convection. As  $C_{\text{tot}}$  is increased, we find the magnitude of the longwave heating anomalies of the cloudy regions increases.

Increased  $C_{\text{tot}}$  is associated with a faster aggregation rate and is mainly the result of an enhanced longwave-FMSE feedback in higher  $C_{\text{tot}}$  simulations during the early stages of aggregation for both the explicit and parameterised convection simulations (the advection feedback also plays a key role in the explicit simulations). This was an expected result for the parameterised simulations, as there was a significant correlation between the longwave feedback and aggregation rate in the parameterised simulations in RCEMIP despite the

advection term becoming more negative. The advection feedback in our explicit simulations does not completely balance the diabatic feedback as was seen on average in the RCEMIP simulations, meaning the rate of aggregation is able to increase as the diabatic feedbacks increase in our simulations, in agreement with Fan et al. (2021) and Bretherton et al. (2005). However, the advection feedback is more independent of  $C_{\text{tot}}$  in the explicit simulations compared to the parameterised simulations. This suggests that the indirect effects of modifying cloud-radiation interactions on circulations play a larger role in explicit convection simulations. It is likely that these indirect effects could outweigh the direct effects in other explicit convection simulations, given that there is no correlation between the longwave feedback and aggregation rate in the RCEMIP CRMs.

The longwave-FMSE feedback is greater in the parameterised simulations which aggregate faster than the explicit simulations. This is in agreement with the findings in Chapter 4, with faster aggregation in the parameterised convection models due to a greater longwave feedback.

The enhanced longwave feedback during the Growth phase at higher  $C_{\text{tot}}$  is due to the enhanced anomalous longwave heating rate in anomalously moist regions thanks to increased heating from high-topped clouds. This causes moist regions to amplify faster, but also helps the dry regions amplify faster by making their typically-negative longwave anomalies more negative by reducing the domain-mean radiative cooling.

The longwave feedback is greater in the parameterised simulations because of the stronger correlation between FMSE anomalies and longwave anomalies. There is a greater fraction of high-topped cloud in anomalously moist environments within the parameterised simulations. In addition, these clouds have a greater anomalous longwave heating because of their higher cloud top height and associated lower cloud top temperature. They produce more Shallow cloud (which have negative longwave heating anomalies) than in the explicit simulations, with the majority of this cloud occurring in anomalously dry regions atop the boundary layer. This further enhances the longwave-FMSE feedback by further

cooling dry regions. The longwave-FMSE correlation is weakened by Shallow cloud in the explicit simulations because the majority of shallow cloud occurs in anomalously moist regions and could be associated with developing cumulus convection. With a greater cloud fraction in the parameterised simulations, the Clear regions, with their associated negative longwave heating anomalies, are confined to more anomalously dry regions. In addition, their anomalous longwave cooling is more anomalous thanks to the greater fraction and the increased heating of high-topped cloud.

An unexpected result is that the domain-mean longwave feedback is sharply reduced after the Growth phase of the Double  $C_{\text{tot}}$  experiments. We find this is due to an increase in High cloud fraction over anomalously dry regions, reducing the longwave-FMSE correlation. It is unclear what the mechanism behind this is, however enhanced cloud-radiation interactions lead to greater cloud base heating and enhanced cloud top cooling. So, perhaps a radiatively-driven circulation may develop that is capable of sustaining High cloud for long periods of time allowing them to spread into dry regions. The decreased domain-mean longwave feedback for the Double  $C_{\text{tot}}$  simulations decreases the total diabatic-FMSE feedback, even becoming negative during the Mature phase of the explicit simulation. However, the decrease in the diabatic-FMSE feedback is balanced by an increase in the advection feedback, so the convection does not disaggregate.

By halving  $C_{\text{tot}}$  in the parameterised convection model, the simulation behaves more similarly to the explicit Control simulation in terms of aggregation characteristics. The longwave-FMSE feedback is similar, as are the total diabatic and advection feedbacks. The rate of aggregation in the Growth phase, as well as the length scale of convection is also the most similar in the parameterised Halve simulation compared to the other parameterised simulations. The distribution of cloud remains very different between these two simulations, with the parameterised simulation having a much greater cloud fraction. However, their aggregating influence is compensated by their reduced radiative forcing. This highlights that convective organisation in parameterised convection simula-

tions can be represented more similarly to explicit convection simulations providing the cloud-radiation interactions are similar.

Modifying the cloud-radiation interactions by adjusting  $C_{\text{tot}}$  has been shown to be a flawed approach, particularly when doubling  $C_{\text{tot}}$ . In certain circumstances where thick high-topped cloud is present, the doubled  $C_{\text{tot}}$  simulations can yield exceptionally low, or even negative OLR values. As a result, these simulations struggle to reach RCE, particularly during the Growth phase. Furthermore, the doubled  $C_{\text{tot}}$  experiments produce an abundance of high cloud in anomalously dry regions which is a feature unseen in the other RCEMIP simulations (Chapter 4) which has major consequences for the total longwave-FMSE feedback.

An alternative approach to adjust the cloud-radiation interactions other than by modifying  $C_{\text{tot}}$  would be preferable, to avoid the unphysical features that we have seen. For example, we could adjust the cloud optical depth for a given condensed water content by scaling the amount of condensed water seen by the radiation scheme. Modifying the clouds' optical depth would adjust the magnitude of their longwave radiative interactions without yielding unphysical longwave heating rates. We have seen in this chapter that many cloud properties do not have a linear relationship with  $C_{\text{tot}}$  (e.g. their longwave-FMSE feedback). Therefore, an experiment should be run with more simulations in which the adjustment in cloud optical depth from one simulation to the next is small (e.g. by scaling the condensed water content in the radiation scheme by 0.4, 0.6, 0.8, 1.0, 1.2 and 1.4).

## 6.1 Conclusions

### Opening Remarks

In this chapter, we present the main conclusions of the thesis. In Section 6.2, we discuss each of the main thesis objectives that are raised in Chapter 1. We then highlight the limitations of our work and discuss future directions of study following these thesis outcomes in Section 6.3.

## 6.2 Summary of Major Outcomes

The spontaneous clustering of convection, termed convective self-aggregation, has been a focus of many recent studies. It is an important area of study because it has major implications for both weather and climate e.g. by leading to more extreme precipitation events (e.g Bao and Sherwood, 2019), influencing cyclogenesis (e.g Wing et al., 2016), and by increasing domain-mean radiative cooling (e.g. Bretherton et al., 2005). However, there

remains much uncertainty in the mechanisms that drive and maintain aggregation (Wing et al., 2017), the sea surface temperature (SST) dependence of aggregation (Wing et al., 2020), and the impacts of aggregation on climate sensitivity (Becker and Wing, 2020). The uncertainty in the response of tropical convective aggregation to a warming climate is a great source of uncertainty in our estimates of the global climate sensitivity (Sherwood et al., 2020).

Interactions between radiation and convection have been shown to be crucial drivers and maintainers of self-aggregation, with interactive radiation being essential for the triggering of self-aggregation (e.g Bretherton et al., 2005; Muller and Held, 2012). Wing and Emanuel (2014) develop a framework to study aggregation that assumes that aggregation is strongly correlated to the spatial variance of vertically-integrated frozen moist static energy (FMSE). A budget equation for the rate of change of FMSE variance shows how interactions between FMSE anomalies and anomalies in radiative heating, surface fluxes and advection of FMSE contribute to changing FMSE variance. This approach allows us to quantify the contributions of these feedbacks to aggregation. A caveat of this approach is the strong SST dependence of FMSE, making it difficult to compare aggregation using the FMSE budget framework with different SSTs. In this thesis, we present modifications to this framework and extend it to allow the study of different cloud type contributions to aggregation. Our main findings are as follows.

### **A framework to study the contributions of cloud-radiation interactions to self-aggregation across a range of SSTs**

In Chapter 2, we describe a new framework to study aggregation that is insensitive to SST. It is based on the vertically-integrated FMSE variance ( $\text{var}(\hat{h})$ ) budget framework described by Wing and Emanuel (2014); however, we normalise vertically-integrated FMSE between hypothetical upper and lower limits as a function of SST. This yields values of normalised  $\hat{h}$  ( $\hat{h}_n$ ) between 0 and 1 and removes the temperature dependence of  $\text{var}(\hat{h})$ .

By rederiving the  $\text{var}(\widehat{h})$  budget equation for  $\widehat{h}_n$ , we then have a budget equation for aggregation that is insensitive to SST. We can then assess how different feedbacks with  $\widehat{h}_n$  contribute to aggregation.

We define different cloud types and study how radiative interactions with each cloud type contribute to aggregation. A cloud type's contribution to the radiation terms in the  $\text{var}(\widehat{h}_n)$  budget equation is equal to its mean covariance between its radiative heating anomaly and its  $\widehat{h}_n$  anomaly, multiplied by its domain fraction. Cloud types are defined in different ways in our three working chapters due to differences in the available data. In Chapters 3 and 5, cloud types are defined by their vertical profile of condensed water, in a similar way to Hill et al. (2018). In Chapter 4, we used top of atmosphere radiative fluxes to define clouds, following the method in Becker and Wing (2020). Regardless of the cloud classification scheme used, conclusions about radiative interactions with clear regions, clouds defined as high-topped, and clouds defined as shallow are generally equivalent.

This  $\text{var}(\widehat{h}_n)$  budget framework is a valuable tool to study aggregation and the feedbacks that control it. It can be used to directly compare aggregation in simulations across a range of SSTs. The use of a cloud classification scheme and the study of the contributions of their radiative interactions to aggregation is a useful way to compare the radiation-convection feedback between models. We have demonstrated how this approach can be used to study radiation-cloud interactions, but a similar approach may be used to study surface flux feedbacks too.

### **The key radiation-convection interactions that development and maintain aggregation**

In Chapter 3, we use our  $\text{var}(\widehat{h}_n)$  budget framework to study the key cloud-radiation interactions that are important for aggregation within simulations of the UK Met Office Unified Model. We assess the sensitivity of these interactions to SST and degree of aggregation. In Chapter 4, we then compare aggregation within the RCEMIP CRMs and GCMs and

test the robustness of our Chapter 3 conclusions.

We find that longwave interactions with high-topped cloud and clear regions are key drivers of self-aggregation in the majority of CRMs and GCMs, and that longwave interactions with high-topped cloud, and shortwave interactions with water vapour, are the main maintainers of aggregation. There is much intermodel variability in the magnitude of these longwave feedbacks, but the shortwave feedbacks are more consistent across all models.

The contributions of these longwave and shortwave radiation interactions to aggregation are sensitive to SST. In the majority of models, high-topped cloud fraction, as well as their normalised longwave heating anomalies, decrease with increasing SST. These factors reduce the amount of anomalous longwave heating in moist regions, and also reduce the anomalous longwave cooling of cloud-free areas in the dry regions, leading to a reduction in the total longwave-aggregation feedback as SST increases. The contribution of shortwave interactions with water vapour to aggregation also decreases with SST. The difference between shortwave absorption by water vapour in the moist and dry regions remains similar with SST, therefore, the shortwave contribution to aggregation decreases with SST, being proportional to the difference between the upper and lower limits of  $\hat{h}$ .

The shortwave contribution to aggregation remains similar with model type and model grid spacing because it is mainly sensitive to interactions with water vapour rather than cloud (which is more sensitive to grid spacing and parameterisation). As a result, it has little inter-model variability for a given SST and degree of aggregation. The longwave contribution to aggregation is more sensitive to model type and grid spacing. In Chapter 3, it was shown that the longwave heating anomalies of high-topped cloud increase as grid spacing is increased within CRMs, likely increasing the longwave contributions to aggregation. In Chapters 4 and 5, we found that the longwave contributions to aggregation further increase at coarser resolutions with parameterised convection, as a result of increased high-topped cloud fraction.

We have shown that high-topped clouds are crucial in determining the total direct longwave feedback by affecting both the cloudy regions and the clear regions' longwave feedback. Other studies have also highlighted that longwave interactions with shallow clouds drive circulations that are key drivers of aggregation. Therefore, both high and low clouds must be well represented in models to accurately represent the contributions of radiative interactions to self-aggregation.

### **How the inter-model variability of cloud-radiation interactions affects self-aggregation**

In Chapter 4, the cloud-radiation interactions are compared between the CRMs and GCMs in RCEMIP. Both the CRMs and GCMs display wide ranges in the rate and degree of aggregation, as well as a wide variety of radiation-convection interactions. We find no correlation between aggregation rate and radiation-convection interactions in the CRMs, with the rate of aggregation being most sensitive to the role of circulations. The aggregation rate in GCMs, on the other hand, is highly dependent on the magnitude of radiation-convection interactions, with a greater longwave feedback leading to faster aggregation rates. The sensitivity of cloud-longwave interactions to SST in GCMs may help to explain why GCMs tend to be more aggregated at higher SSTs. During intermediate to mature stages of aggregation, high-topped clouds tend to occur in anomalously higher  $\hat{h}$  environments at warmer SSTs, resulting in an enhanced longwave feedback during these times. This allows the convection to continue aggregating for a longer duration, leading to more aggregated convection at higher SSTs.

On average, the rate of aggregation is faster in GCMs than CRMs. This is mainly attributed to a greater longwave feedback in GCMs because of a greater high-topped cloud fraction than CRMs.

The high variability of aggregation and its key longwave-FMSE feedbacks amongst models highlights that results from any one model may not be representative of real-world

convection.

### **How modifications to cloud-longwave interactions affect self-aggregation**

In Chapter 5, we modify cloud-longwave interactions in explicit and parameterised convection simulations by altering the parameter that determines the fraction of cloudy sub-columns within a given grid box seen by the longwave radiation scheme ( $C_{\text{tot}}$ ). At early stages of aggregation, the longwave feedback increases with  $C_{\text{tot}}$  which results in faster aggregation via the  $\text{var}(\hat{h}_n)$  metric. This is expected in the parameterised simulations given the results of Chapter 4, in which GCMs with a greater longwave-convection feedback tend to aggregate faster. We find the explicit simulations also aggregate faster with increasing  $C_{\text{tot}}$ , which is in agreement with Fan et al. (2021). However, the advection feedback is more independent of  $C_{\text{tot}}$  in the explicit simulations than in the parameterised simulations. This finding, and the results from Chapter 4, suggest that the indirect effect of cloud-radiation interactions affecting the advection feedback may prove to be the key factor influencing aggregation in other explicit convection simulations.

The organisation of convection in the Halve  $C_{\text{tot}}$  parameterised simulation more closely resembles the explicit convection Control simulation than the other parameterised simulations. The  $\text{var}(\hat{h}_n)$  budget terms are similar, as is the length scale and rate of aggregation. The Halve parameterised simulation still has a much greater Deep cloud fraction than the Control explicit simulation, however this is balanced by an artificially reduced longwave forcing, reducing their aggregating influence. This suggests that parameterised convection models may be able to simulate convective aggregation more accurately, providing clouds and their radiative interactions are more accurately represented.

We note, however, that while the methodology of this experiment scales the magnitude of cloud-radiation interactions, it also leads to some unphysical characteristics in the model. The consequences of these features are not fully known and may have an effect on these conclusions.

### 6.3 Future Work

We have discussed that the methodology to scale the magnitude of cloud radiation interactions in Chapter 5 leads to some unphysical characteristics which may have an effect on the conclusions of the experiment. An alternative method to study the sensitivity of self-aggregation to cloud-radiation interactions that does not lead to such unphysical features would be preferable. Results from that experiment could then be compared to our results to verify the validity of our conclusions. We suggest that by systematically scaling the cloud condensed water content seen by the radiation scheme, cloud optical depth would be adjusted, and thus the magnitude of cloud-radiation interactions would be modified. Using multiple simulations with small adjustments to condensed water content would be beneficial to study the non-linearity of the effects of modified cloud-radiation interactions on convection that were seen in Chapter 5.

The  $\text{var}(\hat{h}_n)$  budget framework builds upon the  $\text{var}(\hat{h})$  budget framework designed by Wing and Emanuel (2014), but our modification allows the framework to be used to fairly compare the contributions of FMSE feedbacks to aggregation across simulations with different SSTs. It can be used as a valuable tool to help study aggregating processes across different models and SST. One of the drawbacks of the  $\text{var}(\hat{h}_n)$  budget framework is that it is based on vertically-integrated parameters; therefore, important feedbacks that occur within specific layers of the atmosphere (e.g. boundary layer feedbacks (Yang, 2018a,b) and radiatively driven circulations (Muller and Held, 2012; Muller and Bony, 2015)) are not able to be explicitly studied in this framework.

Our results from Chapters 4 & 5 suggest that circulations play a crucial role in the development of aggregation, often outweighing the effects of diabatic-FMSE feedbacks in explicit convection simulations. The overall effect of circulations is usually to oppose aggregation, but having a less negative effect at warmer SSTs (proportional to the magnitude of the diabatic feedbacks in the RCEMIP CRMs). Ascent in moist regions, upper

level divergence, then descent in dry regions transports FMSE from moist to dry regions. Yet the low-level radiatively-driven circulations from shallow clouds drives an upgradient transport of FMSE that promotes aggregation (Muller and Held, 2012; Muller and Bony, 2015). The sensitivity of these circulations to SST and cloud-radiative interactions may be investigated using a normalised FMSE framework. Rather than normalising vertically-integrated FMSE, we may still normalise non vertically-integrated FMSE using the same upper and lower limits used in our framework. By using a stream function analysis of 3D normalised FMSE on the overturning circulation (in a similar way to Bretherton et al. (2005)), the transport of normalised FMSE via these circulations, and hence their aggregating influence, may be quantified and compared across different SSTs. A comparison of the influence of these circulations to aggregation within explicit and parameterised convection simulations would be of particular interest. It may help to explain why the relationship between the diabatic-FMSE feedbacks and aggregation rate are different between CRMs and GCMs.

All model simulations in this thesis are idealised, configured over an ocean with a fixed SST, without rotation, without a prescribed mean wind, without a diurnal cycle and without land. The real atmosphere is far more complex than this idealised scenario, so the processes behind real world convective aggregation may differ from those that drive self-aggregation in idealised simulations. However, the use of our analysis framework remains valid to study convection in less idealised studies too. A drawback of this framework in its current form, is that it relies on the surface temperature to be fixed. The use of this framework in studies with a varying surface temperature may require the normalisation limits of  $\hat{h}$  ( $\hat{h}_{\min}$  and  $\hat{h}_{\max}$ ) to vary in space and time.

The framework may then be used to study aggregation using observations and reanalysis data, and then compared to more realistic simulations of convection to examine biases within these climate models. Many of the models in RCEMIP have also been run in more realistic climate configurations. The vast majority of global-scale models are GCMs, but

some of the RCEMIP CRMs are also configured to be part of the DYNamics of the Atmospheric general circulation Modeled On Non-hydrostatic Domains (DYAMOND) project (Stevens et al., 2019), which is a global storm-resolving model intercomparison project. We have seen in this thesis that models exhibit a wide range in longwave heating rates, fraction and FMSE distribution for a given cloud type, resulting in a large range in the magnitude of longwave-FMSE feedbacks. These feedbacks are also sensitive to resolution, critical condensation humidity and convective parameterisation, significantly impacting aggregation. A comparison of cloud fraction, distribution, and radiative properties between GCMs, DYAMOND storm-resolving models, and observations would be of particular interest to study systematic differences in cloud-radiation interactions and aggregation between these models.

As discussed in Chapter 1, cloud-radiation interactions are additionally sensitive to other factors, including cloud particle size and condensed water content, which can both be reliably observed using aircraft and/or satellite retrievals (e.g. Rosenfeld and Lensky, 1998). Future studies could use observations of these properties to quantify discrepancies between observed and simulated convective cloud and their radiative interactions. In doing so, we may be able to more accurately model tropical convection, and reduce our uncertainty in the tropical cloud response to a warming climate.

## APPENDIX A

### NORMALISED FMSE VARIANCE BUDGET EQUATION

#### DERIVATION

Starting with the equation of normalised FMSE:

$$\hat{h}_n = \frac{\hat{h} - \hat{h}_{\min}}{\hat{h}_{\max} - \hat{h}_{\min}} \quad (\text{A.1})$$

$\hat{h}_n$ , can be broken down into its domain-mean state plus the anomaly from the mean:

$$\hat{h}_n = \{\hat{h}_n\} + \hat{h}'_n \quad (\text{A.2})$$

where curly brackets denote the domain-mean state. Splitting  $\hat{h}_n$  and  $\hat{h}$  in A.1 into their domain mean and anomaly, we get:

$$\{\hat{h}_n\} + \hat{h}'_n = \frac{\{\hat{h}\} - \hat{h}_{\min}}{\hat{h}_{\max} - \hat{h}_{\min}} + \frac{\hat{h}'}{\hat{h}_{\max} - \hat{h}_{\min}} \quad (\text{A.3})$$

The first term on both sides of the equation is the domain-mean of  $\hat{h}_n$  and the second term is the anomaly. By subtracting the domain-mean from this equation, we end up with an expression for the anomaly of  $\hat{h}_n$ :

$$\hat{h}'_n = \frac{\hat{h}'}{\hat{h}_{\max} - \hat{h}_{\min}} \quad (\text{A.4})$$

Differentiating this with respect to time:

$$\frac{\partial \hat{h}'_n}{\partial t} = \frac{1}{\hat{h}_{\max} - \hat{h}_{\min}} \frac{\partial \hat{h}'}{\partial t} \quad (\text{A.5})$$

Multiplying with  $\hat{h}'_n$ , using the identity  $x \times \partial x / \partial t = 1/2 \times \partial x^2 / \partial t$  on the left hand side, and substituting Equation (A.4) for  $\hat{h}'_n$  on the right hand side:

$$\frac{1}{2} \frac{\partial \hat{h}'_n{}^2}{\partial t} = \frac{\hat{h}'}{(\hat{h}_{\max} - \hat{h}_{\min})^2} \frac{\partial \hat{h}'}{\partial t} \quad (\text{A.6})$$

Taking the anomaly of the expression for the tendency of  $\hat{h}$  shown in Equation 3 of Wing and Emanuel (2014):

$$\frac{\partial \hat{h}'}{\partial t} = SEF' + LW' + SW' - \nabla_h \cdot \mathbf{u} \hat{h} \quad (\text{A.7})$$

and substituting this into Equation (A.6) gives us an expression for the  $\hat{h}'_n$  tendency budget in terms of  $\hat{h}'$ :

$$\frac{1}{2} \frac{\partial \hat{h}'_n{}^2}{\partial t} = \frac{\hat{h}' LW' + \hat{h}' SW' + \hat{h}' SEF' - \hat{h}' \nabla_h \cdot \mathbf{u} \hat{h}}{(\hat{h}_{\max} - \hat{h}_{\min})^2} \quad (\text{A.8})$$

Or in terms of  $\hat{h}'_n$ , the equation becomes:

$$\frac{1}{2} \frac{\partial \hat{h}'_n{}^2}{\partial t} = \hat{h}'_n LW'_n + \hat{h}'_n SW'_n + \hat{h}'_n SEF'_n - \hat{h}'_n \nabla_h \cdot \mathbf{u} \hat{h}_n \quad (\text{A.9})$$

Here, each normalised variable is equal to the original variable in Equation (A.7) divided by the difference between  $\hat{h}_{\max}$  and  $\hat{h}_{\min}$ .

## BIBLIOGRAPHY

- Allan, R. P., Shine, K. P., Slingo, A. and Pamment, J. A. (1999) The dependence of clear-sky outgoing long-wave radiation on surface temperature and relative humidity. *Quarterly Journal of the Royal Meteorological Society*, **125**, 2103–2126.
- Arnold, N. P. and Putman, W. M. (2018) Nonrotating Convective Self-Aggregation in a Limited Area AGCM. *Journal of Advances in Modeling Earth Systems*, **10**, 1029–1046.
- Arnold, N. P. and Randall, D. A. (2015) Global-scale convective aggregation: Implications for the Madden-Julian Oscillation. *Journal of Advances in Modeling Earth Systems*, **7**, 1499–1518.
- Back, L. E. and Bretherton, C. S. (2009) On the Relationship between SST Gradients, Boundary Layer Winds, and Convergence over the Tropical Oceans. *Journal of Climate*, **22**, 4182 – 4196.
- Bao, J. and Sherwood, S. C. (2019) The Role of Convective Self-Aggregation in Extreme Instantaneous Versus Daily Precipitation. *Journal of Advances in Modeling Earth Systems*, **11**, 19–33.

- Barker, H. W., Stephens, G. L. and Fu, Q. (1999) The sensitivity of domain-averaged solar fluxes to assumptions about cloud geometry. *Quarterly Journal of the Royal Meteorological Society*, **125**, 2127–2152.
- Becker, T., Stevens, B. and Hohenegger, C. (2017) Imprint of the convective parameterization and sea-surface temperature on large-scale convective self-aggregation. *Journal of Advances in Modeling Earth Systems*, **9**, 1488–1505.
- Becker, T. and Wing, Allison, A. (2020) Understanding the Extreme Spread in Climate Sensitivity within the Radiative-Convective Equilibrium Model Intercomparison Project. *Journal of Advances in Modeling Earth Systems*, **12**, e2020MS002165.
- Beucler, T. and Cronin, T. (2019) A budget for the size of convective self-aggregation. *Quarterly Journal of the Royal Meteorological Society*, **145**, 947–966.
- Beucler, T. and Cronin, T. W. (2016) Moisture-radiative cooling instability. *Journal of Advances in Modeling Earth Systems*, **8**, 1620–1640.
- Bony, S., Stevens, B., Coppin, D., Becker, T., Reed, K. A., Voigt, A. and Medeiros, B. (2016) Thermodynamic Control of Anvil Cloud Amount. *Proceedings of the National Academy of Sciences of the United States of America*, **113**, 8927–8932.
- Bretherton, C. S., Blossey, P. N. and Khairoutdinov, M. (2005) An Energy-Balance Analysis of Deep Convective Self-Aggregation above Uniform SST. *Journal of the Atmospheric Sciences*, **62**, 4273–4292.
- Bretherton, C. S., Peters, M. E. and Back, L. E. (2004) Relationships between Water Vapor Path and Precipitation over the Tropical Oceans. *Journal of Climate*, **17**, 1517 – 1528.
- Bu, Y. P., Fovell, R. G. and Corbosiero, K. L. (2014) Influence of Cloud–Radiative Forcing on Tropical Cyclone Structure. *Journal of the Atmospheric Sciences*, **71**, 1644 – 1662.

- Bush, M., Allen, T., Bain, C., Boutle, I., Edwards, J., Finnenkoetter, A., Franklin, C., Hanley, K., Lean, H., Lock, A., Manners, J., Mittermaier, M., Morcrette, C., North, R., Petch, J., Short, C., Vosper, S., Walters, D., Webster, S., Weeks, M., Wilkinson, J., Wood, N. and Zerroukat, M. (2020) The first Met Office Unified Model-JULES Regional Atmosphere and Land configuration, RAL1. *Geoscientific Model Development*, **13**, 1999–2029.
- Cahalan, R. F., Ridgway, W., Wiscombe, W. J., Bell, T. L. and Snider, J. B. (1994) The Albedo of Fractal Stratocumulus Clouds. *Journal of Atmospheric Sciences*, **51**, 2434–2460.
- Carstens, J. D. and Wing, A. A. (2022) A Spectrum of Convective Self-Aggregation Based on Background Rotation. *Journal of Advances in Modeling Earth Systems*, **14**, e2021MS002860.
- Charney, J. G. and Phillips, N. A. (1953) Numerical Integration of the Quasi-Geostrophic Equations for Barotropic and Simple Baroclinic Flows. *Journal of the Atmospheric Sciences*, **10**, 71–99.
- Chen, Q., Fan, J., Hagos, S., Gustafson Jr., W. I. and Berg, L. K. (2015) Roles of wind shear at different vertical levels: Cloud system organization and properties. *Journal of Geophysical Research: Atmospheres*, **120**, 6551–6574.
- Coppin, D. and Bony, S. (2015) Physical mechanisms controlling the initiation of convective self-aggregation in a General Circulation Model. *Journal of Advances in Modeling Earth Systems*, **7**, 2060–2078.
- (2017) Internal variability in a coupled general circulation model in radiative-convective equilibrium. *Geophysical Research Letters*, **44**, 5142–5149.
- (2018) On the Interplay Between Convective Aggregation, Surface Temperature Gra-

- dients, and Climate Sensitivity. *Journal of Advances in Modeling Earth Systems*, **10**, 3123–3138.
- Craig, G. C. and Mack, J. M. (2013) A coarsening model for self-organization of tropical convection. *Journal of Geophysical Research: Atmospheres*, **118**, 8761–8769.
- Da Silva, N. A., Muller, C., Shamekh, S. and Fildier, B. (2021) Significant Amplification of Instantaneous Extreme Precipitation With Convective Self-Aggregation. *Journal of Advances in Modeling Earth Systems*, **13**, e2021MS002607.
- Edwards, J. M. and Slingo, A. (1996) Studies with a flexible new radiation code. I: Choosing a configuration for a large-scale model. *Quarterly Journal of the Royal Meteorological Society*, **122**, 689–719.
- Emanuel, K., Wing, A. A. and Vincent, E. M. (2014) Radiative-Convective Instability. *Journal of Advances in Modeling Earth Systems*, **6**, 75–90.
- Emanuel, K. et al. (2003) Tropical cyclones. *Annual review of earth and planetary sciences*, **31**, 75–104.
- Fan, Y., Chung, Y. T. and Shi, X. (2021) The Essential Role of Cloud-Radiation Interaction in Nonrotating Convective Self-Aggregation. *Geophysical Research Letters*, **48**, e2021GL095102.
- Fiedler, S., Crueger, T., D’Agostino, R., Peters, K., Becker, T., Leutwyler, D., Paccini, L., Burdanowitz, J., Buehler, S. A., Cortes, A. U., Dauhut, T., Dommenges, D., Fraedrich, K., Jungandreas, L., Maher, N., Naumann, A. K., Rugenstein, M., Sakradzija, M., Schmidt, H., Sielmann, F., Stephan, C., Timmreck, C., Zhu, X. and Stevens, B. (2020) Simulated Tropical Precipitation Assessed across Three Major Phases of the Coupled Model Intercomparison Project (CMIP). *Monthly Weather Review*, **148**, 3653 – 3680.

- Fu, Q. and Liou, K. N. (1993) Parameterization of the Radiative Properties of Cirrus Clouds. *Journal of Atmospheric Sciences*, **50**, 2008 – 2025.
- Held, I. M., Helmer, R. S. and Ramaswamy, V. (1993) Radiative-Convective Equilibrium with Explicit Two-Dimensional Moist Convection. *Journal of the Atmospheric Sciences*, **50**, 3909–3927.
- Hill, P. G., Allan, R. P., Chiu, J. C., Bodas-Salcedo, A. and Knippertz, P. (2018) Quantifying the Contribution of Different Cloud Types to the Radiation Budget in Southern West Africa. *Journal of Climate*, **31**, 5273–5291.
- Hohenegger, C. and Stevens, B. (2016) Coupled radiative convective equilibrium simulations with explicit and parameterized convection. *Journal of Advances in Modeling Earth Systems*, **8**, 1468–1482.
- Holloway, C. E., Wing, A. A., Bony, S., Muller, C., Masunaga, H., L’Ecuyer, T. S., Turner, D. D. and Zuidema, P. (2017) Observing Convective Aggregation. *Surveys in Geophysics*, **38**, 1199–1236.
- Holloway, C. E. and Woolnough, S. J. (2016) The Sensitivity of Convective Aggregation to Diabatic Processes in Idealized Radiative-Convective Equilibrium simulations. *Journal of Advances in Modeling Earth Systems*, **8**, 166–195.
- Hong, Y., Liu, G. and Li, J.-L. F. (2016) Assessing the Radiative Effects of Global Ice Clouds Based on CloudSat and CALIPSO Measurements. *Journal of Climate*, **29**, 7651 – 7674.
- Houze, R. A. (1977) Structure and Dynamics of a Tropical Squall–Line System. *Monthly Weather Review*, **105**, 1540–1567.
- (2004) Mesoscale Convective Systems. *Reviews of Geophysics*, **42**, RG4003.

- Jeevanjee, N. and Romps, D. M. (2013) Convective self-aggregation, cold pools, and domain size. *Geophysical Research Letters*, **40**, 994–998.
- Kiladis, G. N., Wheeler, M. C., Haertel, P. T., Straub, K. H. and Roundy, P. E. (2009) Convectively Coupled Equatorial Waves. *Reviews of Geophysics*, **47**, RG2003.
- Koll, D. D. B. and Cronin, T. W. (2018) Earth’s outgoing longwave radiation linear due to H<sub>2</sub>O greenhouse effect. *Proceedings of the National Academy of Sciences*, **115**, 10293–10298.
- Liou, K.-N. (1986) Influence of Cirrus Clouds on Weather and Climate Processes: A Global Perspective. *Monthly Weather Review*, **114**, 1167 – 1199.
- Liu, C. and Zipser, E. (2013) Regional variation of morphology of organized convection in the tropics and subtropics. *Journal of Geophysical Research: Atmospheres*, **118**, 453–466.
- Lock, A. P., Brown, A. R., Bush, M. R., Martin, G. M. and Smith, R. N. B. (2000) A New Boundary Layer Mixing Scheme. Part I: Scheme Description and Single-Column Model Tests. *Monthly Weather Review*, **128**, 3187–3199.
- Madden, R. A. and Julian, P. R. (1971) Detection of a 40–50 Day Oscillation in the Zonal Wind in the Tropical Pacific. *Journal of the Atmospheric Sciences*, **28**, 702–708.
- Manabe, S. and Wetherald, R. T. (1967) Thermal Equilibrium of the Atmosphere with a Given Distribution of Relative Humidity. *Journal of Atmospheric Sciences*, **24**, 241 – 259.
- Mapes, B. E. and Houze, R. A. (1993) Cloud Clusters and Superclusters over the Oceanic Warm Pool. *Monthly Weather Review*, **121**, 1398–1415.
- Matsuno, T. (1966) Quasi-Geostrophic Motions in the Equatorial Area. *Journal of the Meteorological Society of Japan. Ser. II*, **44**, 25–43.

- Morcrette, C. (2013) Sub-grid cloud parametrization issues in the Met Office Unified Model: A tale of several grey zones.
- Muller, C. and Bony, S. (2015) What favors convective aggregation and why? *Geophysical Research Letters*, **42**, 5626–5634.
- Muller, C. and Held, I. M. (2012) Detailed Investigation of the Self-Aggregation of Convection in Cloud-Resolving Simulations. *Journal of the Atmospheric Sciences*, **69**, 2551–2565.
- Muller, C. J. and Romps, D. M. (2018) Acceleration of tropical cyclogenesis by self-aggregation feedbacks. *Proceedings of the National Academy of Sciences*, **115**, 2930–2935.
- Müller, S. K. and Hohenegger, C. (2020) Self-Aggregation of Convection in Spatially Varying Sea Surface Temperatures. *Journal of Advances in Modeling Earth Systems*, **12**, e2019MS001698.
- Nakazawa, T. (1988) Tropical Super Clusters within Intraseasonal Variations over the Western Pacific. *Journal of the Meteorological Society of Japan*, **66**, 823–839.
- Naumann, A. K., Stevens, B., Hohenegger, C. and Mellado, J. P. (2017) A Conceptual Model of a Shallow Circulation Induced by Prescribed Low-Level Radiative Cooling. *Journal of the Atmospheric Sciences*, **74**, 3129 – 3144.
- Nesbitt, S. W., Zipser, E. J. and Cecil, D. J. (2000) A Census of Precipitation Features in the Tropics Using TRMM: Radar, Ice Scattering, and Lightning Observations. *Journal of Climate*, **13**, 4087 – 4106.
- Nolan, D., Rappin, E. and Emanuel, K. (2007) Tropical cyclogenesis sensitivity to environmental parameters in radiative-convective equilibrium. *Quarterly Journal of the Royal Meteorological Society*, **133**, 2085–2107.

- Pincus, R., Barker, H. W. and Morcrette, J.-J. (2003) A fast, flexible, approximate technique for computing radiative transfer in inhomogeneous cloud fields. *Journal of Geophysical Research: Atmospheres*, **108**, 4376.
- Pope, K. N., Holloway, C. E., Jones, T. R. and Stein, T. H. M. (2021) Cloud-Radiation Interactions and Their Contributions to Convective Self-Aggregation. *Journal of Advances in Modeling Earth Systems*, **13**, e2021MS002535.
- (2023) Radiation, Clouds, and Self-Aggregation in RCEMIP Simulations. *Journal of Advances in Modeling Earth Systems*, **15**, e2022MS003317.
- Raymond, D. J. and Fuchs, Z. (2009) Moisture Modes and the Madden–Julian Oscillation. *Journal of Climate*, **22**, 3031 – 3046.
- Roca, R., Aublanc, J., Chambon, P., Fiolleau, T. and Viltard, N. (2014) Robust Observational Quantification of the Contribution of Mesoscale Convective Systems to Rainfall in the Tropics. *Journal of Climate*, **27**, 4952 – 4958.
- Roca, R. and Fiolleau, T. (2020) Extreme precipitation in the tropics is closely associated with long-lived convective systems. *Commun Earth Environ*, **1**.
- Romps, D. M. (2015) MSE Minus CAPE is the True Conserved Variable for an Adiabatically Lifted Parcel. *Journal of the Atmospheric Sciences*, **72**, 3639 – 3646.
- Rosenfeld, D. and Lensky, I. M. (1998) Satellite-Based Insights into Precipitation Formation Processes in Continental and Maritime Convective Clouds. *Bulletin of the American Meteorological Society*, **79**, 2457 – 2476.
- Rotunno, R., Klemp, J. B. and Weisman, M. L. (1988) A Theory for Strong, Long-Lived Squall Lines. *Journal of Atmospheric Sciences*, **45**, 463 – 485.
- Ruckstuhl, C., Philipona, R., Morland, J. and Ohmura, A. (2007) Observed relationship

- between surface specific humidity, integrated water vapor, and longwave downward radiation at different altitudes. *Journal of Geophysical Research: Atmospheres*, **112**.
- Ruppert, J. H., Wing, A. A., Tang, X. and Duran, E. L. (2020) The critical role of cloud-infrared radiation feedback in tropical cyclone development. *Proceedings of the National Academy of Sciences*, **117**, 27884–27892.
- Räisänen, P. and Barker, H. W. (2004) Evaluation and optimization of sampling errors for the Monte Carlo Independent Column Approximation. *Quarterly Journal of the Royal Meteorological Society*, **130**, 2069–2085.
- Räisänen, P., Barker, H. W., Khairoutdinov, M. F., Li, J. and Randall, D. A. (2004) Stochastic generation of subgrid-scale cloudy columns for large-scale models. *Quarterly Journal of the Royal Meteorological Society*, **130**, 2047–2067.
- Shamekh, S., Muller, C., Duvel, J.-P. and D’Andrea, F. (2020) Self-Aggregation of Convective Clouds With Interactive Sea Surface Temperature. *Journal of Advances in Modeling Earth Systems*, **12**, e2020MS002164.
- Sherwood, S. C., Webb, M. J., Annan, J. D., Armour, K. C., Forster, P. M., Hargreaves, J. C., Hegerl, G., Klein, S. A., Marvel, K. D., Rohling, E. J., Watanabe, M., Andrews, T., Braconnot, P., Bretherton, C. S., Foster, G. L., Hausfather, Z., Von Der Heydt, A. S., Knutti, R., Mauritsen, T., Norris, J. R., Proistosescu, C., Rugenstein, M., Schmidt, G. A., Tokarska, K. B. and Zelinka, M. D. (2020) An assessment of Earth’s climate sensitivity using multiple lines of evidence. *Reviews of Geophysics*, **58**, e2019RG000678.
- Smagorinsky, J. (1963) General Circulation Experiments with the Primitive Equations I. The Basic Experiment. *Monthly Weather Review*, **91**, 99–164.
- Smith, R. N. B. (1990) A scheme for predicting layer clouds and their water content in a general circulation model. *Quarterly Journal of the Royal Meteorological Society*, **116**, 435–460.

- Stevens, B., Satoh, M., Auger, S. L., Biercamp, J., Bretherton, C. S., Chen, X., Düben, P., Judt, F., Khairoutdinov, M., Klocke, D., Kodama, C., L., K., Lin, S. J., Neumann, P., Putman, W. M., Röber, N., Shibuya, R., Vanniere, B., Vidale, P. L., Wedi, N. and Zhou, L. (2019) DYAMOND: The DYNAMics of the Atmospheric general circulation Modeled On Non-hydrostatic Domains. *Progress in Earth and Planetary Science*, **6**.
- Tobin, I., Bony, S., Holloway, C. E., Grandpeix, J.-Y., Sèze, G., Coppin, D., Woolnough, S. J. and Roca, R. (2013) Does convective aggregation need to be represented in cumulus parameterizations? *Journal of Advances in Modeling Earth Systems*, **5**, 692–703.
- Tompkins, A. M. (2001) Organization of Tropical Convection in Low Vertical Wind Shears: The Role of Water Vapor. *Journal of the Atmospheric Sciences*, **58**, 529 – 545.
- Tompkins, A. M. and Craig, G. C. (1998) Radiative–convective equilibrium in a three-dimensional cloud-ensemble model. *Quarterly Journal of the Royal Meteorological Society*, **124**, 2073–2097.
- Tompkins, A. M. and Semie, A. G. (2017) Organization of tropical convection in low vertical wind shears: Role of updraft entrainment. *Journal of Advances in Modeling Earth Systems*, **9**, 1046–1068.
- Vaquero-Martínez, J., Antón, M., Ortiz de Galisteo, J. P., Román, R. and Cachorro, V. E. (2018) Water vapor radiative effects on short-wave radiation in Spain. *Atmospheric Research*, **205**, 18–25.
- Vergara-Temprado, J., Miltenberger, A. K., Furtado, K., Grosvenor, D. P., Shipway, B. J., Hill, A. A., Wilkinson, J. M., Field, P. R., Murray, B. J. and Carslaw, K. S. (2018) Strong control of Southern Ocean cloud reflectivity by ice-nucleating particles. *Proceedings of the National Academy of Sciences*, **115**, 2687–2692.
- Walters, D., Baran, A. J., Boutle, I., Brooks, M., Earnshaw, P., Edwards, J., Furtado, K., Hill, P., Lock, A., Manners, J., Morcrette, C., Mulcahy, J., Sanchez, C., Smith,

- C., Stratton, R., Tennant, W., Tomassini, L., Van Weverberg, K., Vosper, S., Willett, M., Browse, J., Bushell, A., Carslaw, K., Dalvi, M., Essery, R., Gedney, N., Hardiman, S., Johnson, B., Johnson, C., Jones, A., Jones, C., Mann, G., Milton, S., Rumbold, H., Sellar, A., Ujiie, M., Whitall, M., Williams, K. and Zerroukat, M. (2019) The Met Office Unified Model Global Atmosphere 7.0/7.1 and JULES Global Land 7.0 configurations. *Geoscientific Model Development*, **12**, 1909–1963.
- Walters, D. N., Best, M. J., Bushell, A. C., Copsey, D., Edwards, J. M., Falloon, P. D., Harris, C. M., Lock, A. P., Manners, J. C., Morcrette, C. J., Roberts, M. J., Stratton, R. A., Webster, S., Wilkinson, J. M., Willett, M. R., Boutle, I. A., Earnshaw, P. D., Hill, P. G., MacLachlan, C., Martin, G. M., Moufouma-Okia, W., Palmer, M. D., Petch, J. C., Rooney, G. G., Scaife, A. A. and Williams, K. D. (2011) The Met Office Unified Model Global Atmosphere 3.0/3.1 and JULES Global Land 3.0/3.1 configurations. *Geoscientific Model Development*, **4**, 919–941.
- Wilson, D. R. and Ballard, S. P. (1999) A microphysically based precipitation scheme for the UK Meteorological Office Unified Model. *Quarterly Journal of the Royal Meteorological Society*, **125**, 1607–1636.
- Wilson, D. R., Bushell, A. C., Kerr-Munslow, A. M., Price, J. D. and Morcrette, C. J. (2008) PC2: A prognostic cloud fraction and condensation scheme. I: Scheme description. *Quarterly Journal of the Royal Meteorological Society*, **134**, 2093–2107.
- Wing, A. A. (2019) Self-Aggregation of Deep Convection and its Implications for Climate. *Current Climate Change Reports*, **5**, 1–11.
- Wing, A. A., Camargo, S. J. and Sobel, A. H. (2016) Role of radiative-convective feedbacks in spontaneous tropical cyclogenesis in idealized numerical simulations. *Journal of the Atmospheric Sciences*, **73**, 2633–2642.

- Wing, A. A. and Cronin, T. W. (2016) Self-aggregation of convection in long channel geometry. *Quarterly Journal of the Royal Meteorological Society*, **142**, 1–15.
- Wing, A. A., Emanuel, K., Holloway, C. E. and Muller, C. (2017) Convective Self-Aggregation in Numerical Simulations: A Review. *Surveys in Geophysics*, **38**, 1173–1197.
- Wing, A. A. and Emanuel, K. A. (2014) Physical Mechanisms Controlling Self-Aggregation of Convection in Idealized Numerical Modeling Simulations. *Journal of Advances in Modeling Earth Systems*, **6**, 59–74.
- Wing, A. A., Reed, K. A., Satoh, M., Stevens, B., Bony, S. and Ohno, T. (2018) Radiative-Convective Equilibrium Model Intercomparison Project. *Geoscientific Model Development*, **11**, 793–813.
- Wing, A. A., Stauffer, C. L., Becker, T., Reed, K. A., Ahn, M.-s., Arnold, N., Bony, S., Branson, M., Chaboureau, J.-p., Roode, S. D., Gayatri, K., Hohenegger, C., Hu, I.-k., Jansson, F., Jones, T. R., Khairoutdinov, M., Kim, D., Matsugishi, S., Martin, Z., Medeiros, B., Miura, H., Moon, Y., Sebastian, K. M., Ohno, T., Popp, M., Prabhakaran, T., Randall, D., Rios-berrios, R., Rochetin, N., Roehrig, R., David, M., Ruppert, J. H., Satoh, M. and Silvers, L. (2020) Clouds and Convective Self-Aggregation in a Multi-Model Ensemble of Radiative-Convective Equilibrium Simulations. *Journal of Advances in Modeling Earth Systems*, **12**, e2020MS0021380.
- Wood, N., Staniforth, A., White, A., Allen, T., Diamantakis, M., Gross, M., Melvin, T., Smith, C., Vosper, S., Zerroukat, M. and Thuburn, J. (2014) An inherently mass-conserving semi-implicit semi-Lagrangian discretization of the deep-atmosphere global non-hydrostatic equations. *Quarterly Journal of the Royal Meteorological Society*, **140**, 1505–1520.

- Yang, D. (2018a) Boundary Layer Diabatic Processes, the Virtual Effect, and Convective Self-Aggregation. *Journal of Advances in Modeling Earth Systems*, **10**, 2163–2176.
- (2018b) Boundary Layer Height and Buoyancy Determine the Horizontal Scale of Convective Self-Aggregation. *Journal of the Atmospheric Sciences*, **75**, 469 – 478.